COUPLED DYNAMICS OF THIN MICROELECTRO MECHANICAL SYSTEMS

by Ranajay Ghosh

COUPLED DYNAMICS OF THIN MICRO ELECTRO MECHANICAL SYSTEMS

A Dissertation

Presented to the Faculty of the Graduate School

of Cornell University

in Partial Fulfillment of the Requirements for the Degree of

Doctor of Philosophy

by

Ranajay Ghosh

August 2010

COUPLED DYNAMICS OF THIN MICRO ELECTRO MECHANICAL SYSTEMS

Ranajay Ghosh, Ph.D.

Cornell University 2010

Microelectromechanical systems (MEMS) combine high levels sensitivity and multifunctionality with small size and low power consumption. The major prime mover for MEMS industry in the past has been automobiles whereas consumer electronics (E.g. iPhones and Nintendo Wii) is the most important sector for growth now. With new focus on small scale energy harvesting from ambient vibration and air flow, MEMS have definitely entered a new generation. A significant factor propelling design and manufacturing is the need for reliable and robust computational tools. The basic skeleton of MEMS still remain suspended or anchored beams and plates actuated by electrical, electrostatic, thermal, magnetic or photonic mechanisms. This dissertation describes the simulation of coupled dynamics of thin MEMS actuated electrostatically and vibrating in a fluid medium. Although, only micro-beams are addressed here, the computational structure developed here can be directly used to address other forms of actuation or medium. A fully Lagrangian approach is developed to couple the electrostatic, fluidic and mechanical problem which is then solved using Newton's method. This approach eliminates the problems arising from remeshing and computing of derivatives of integrals over changing domain shapes. The mechanical problem is solved using finite element method (FEM) whereas the fluidic and electrostatic problems are tackled using the boundary element method (BEM). Severe numerical issues arise when dealing with very thin microstruc-

tures (very high aspect ratio) for the BEM problem due to nearly singular integrals. A special BEM which addresses these problems has been developed for both the electrostatic and the fluidic problem. A singularity of mathematical nature arises at the free edge for the electrostatic BEM problem when dealing with cantilevers. This problem is solved by incorporating a singular element formulation for the electrostatic BEM. The resulting solution is compared with the case of simple extrapolation for some typical performance parameters. Finally, several possible extensions of current work like adapting the algorithm for nanoelectromechanical systems (NEMS), computational acceleration using the fast multipole method (FMM) and quantifying uncertainty has been explained in the concluding chapter.

BIOGRAPHICAL SKETCH

Ranajay Ghosh was born on November 7, 1982 in Patna, India where he attended Saint Michael's High School from 1988-1998. He then enrolled in Patna Science College for two years of high schooling. Ranajay then got admission into the Indian Institute of Technology, Kharagpur in the department of mechanical engineering for a bachelor of technology (B.Tech) degree. In his last year of undergraduate studies, he was awarded a fellowship to pursue a PhD in Theoretical and Applied Mechanics at Cornell University, Ithaca, NY. Ranajay spent the fall semester of 2007 interning at the General Electric Company's Global Research Center located in Niskayuna, NY working in the Lifing Technologies Lab. Following his graduation from Cornell Ranajay has joined as postdoctoral research associate at the Rensselaer Polytechnic Institute, Troy, NY and wants to continue pursuing research and teaching in the area of computational solid mechanics in the future.

This document is dedicated to my parents.

ACKNOWLEDGEMENTS

A journey of thousand steps always begins with the first. Getting an opportunity to work with Professor Subrata Mukherjee as my adviser was the first on my journey to obtain this PhD. Language is often an approximation and it is pretty poor one to describe the great mentorship of Professor Mukherjee. In addition to occupying the formal positions of adviser and teacher he has seamlessly contributed to my professional and personal growth far beyond the usual confines of graduate school. Working with Professor Mukherjee has been both an honor and a privilege. I may only hope that I can stand up with pride in the immense galaxy of Prof Mukherjee's illustrious students.

I would like to take this opportunity to thank the members of my committee, Professor Richard Rand and Professor Charles Van Loan for the extremely valuable insights and suggestions for my dissertation. My thanks are due to Prof Stephen Vavasis who served in my committee before moving to University of Waterloo for many valuable suggestions at the beginning of my research. In particular, his class on 'Numerical Solutions to Differential Equations' greatly aided my understanding of numerical methods that formed the bedrock of the current research. I wish to thank the extremely helpful members of Theoretical and Applied Mechanics department under whom I have served as teaching assistants. In particular fruitful discussions on a variety of topics related to my research and applied mechanics in general with Professor Herbert Hui, Professor Timothy Healey and Professor Alan Zehnder needs special mention.

No words can describe the great company of friends I enjoyed in Ithaca all these years. In particular I am greatly indebted to Michael Czabaj and William Whittacre for the deeply personal and intellectual company provided during my graduate school. In addition, I am indebted to my room mate Krishnaprasad

Vikram for providing such an enriching and inspiring presence in my house together with Yogeshwer Sharma and Dharmavaram Sanjay. In addition, special thanks are also due to my former office mate Michele Carpenter and other classmates Siva Prasad Pulla, Lulin Shen and Jingzhou Liu for a fun filled graduate life at Cornell. Thanks are also due to Amit Halder, Manish Agarwal, Karthick Chandraseker and Haolin Zhu for many hours of valuable discussions both inside and outside of classrooms. Finally thanks to the couples Ramaranjan and Lopamudra Bhattacharya and Rahul and Kavita Anand for providing me with the comforts of a home away from home.

I wish to thank my undergraduate mentors Professor Kumar Ray (at the Indian Institute of Technology, Kharagpur) and Professor Asitava Ghoshal (during my internship at the Indian Institute of Science) without whose encouragement and vision, even the first step of this journey would have been impossible.

This section on acknowledgment would be incomplete without mentioning my grandmother (deceased), mother, father and brother whose unconditional and staunch support for higher studies provided both motivation and courage to finish my doctoral studies.

Finally I wish to acknowledge the financial support to this dissertation provided by the National Science Foundation grant $\#CMS - 0508466$ and the department of Theoretical and Applied Mechanics and Mathematics for providing me with generous teaching assistantships and the Harriet-Davis graduate fellowship.

TABLE OF CONTENTS

LIST OF FIGURES

CHAPTER 1

INTRODUCTION

The middle of the last century saw the birth of the modern semiconductor based electronic device [1]. An ever unsatiable drive to pack more processing power in less space heralded the birth of the modern microelectronic age when within a decade, the integrated circuit was developed [2]. A vast microelectronic industry was about to be born driven by increasing research and high demand for computing power in the post world war era of unprecedented economic prosperity. An estimate of the growth of this sector was prophesied by Gordon Moore who formulated the now famous *Moore's Law* [3] which gives a rough time rate of increasing density and decreasing prices of microelectronic devices packed in a chip. Attempts to miniaturize are still going on with undiminished vigor as INTEL Corp. announced its $45nm$ processor in the year 2008. While the microelectronic revolution has transcended many generations by now, the miniaturization of mechanical devices and mechanisms is relatively new. Although the immense possibilities that such a change of scale may bring were already talked about as early as 1959 by none other than Feynman [4] himself, the growth remained challenged due to lack of both design and manufacturing expertise. Fortunately, a paradigm shift in design, fabrication and simulation of microelectromechanical systems (MEMS) finally began to take place by the beginning of the last decade and growth has been brisk ever since. Steadily more and more micro devices have been invading our automobiles, cell phones, printers, medical devices, airplanes, batteries, digital displays and even lab instruments.

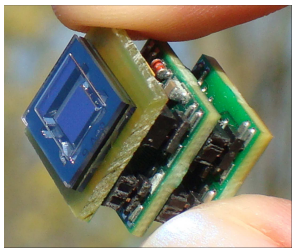

Figure 1.1: MEMS Energy Harvester Developed by IMEC

1.1 Historical Origins of MEMS

As noted in the previous section, the foundation of the current MEMS industry can be traced back to the beginnings of the microprocessor industry. However, the first true MEMS device, a resonant gate transistor was fabricated by researchers at Westinghouse in 1964 by H.C. Nathanson and his team. Researchers at the Stanford University developed the first MEMS accelerometer[1] in 1979. This device has proved to be hugely successful with millions sold till date finding their use from CPR-machines to iPhone-3GS. Within the next five years, the polysilicon surface micromachining prcess was developed at the University of California, Berkeley (1984) making it possible to manufacture MEMS and integrated circuits together for the first time.

In the meantime, researchers were already pushing the limits of molecular nanotechnology. Eric Drexler's 1981 article [5] titled *Protein design as a pathway to molecular manufacturing* published in the Proceedings of the National Academy of Sciences became one of the first articles which could be genuinely called venturing into the zone of molecular nanotechnology. Soon the scanning tunneling microscope (STM) based on the idea of quantum tunneling was developed by

[1] An accelerometer is a device that measures proper acceleration, the acceleration experienced relative to freefall.

Binning and Rohrer at IBM Zurich in 1982 which could resolve images in the nanometer scale[2]. With this resolution, individual atoms within materials are routinely imaged and manipulated. The STM can be used not only in ultra high vacuum but also in air, water, and various other liquid or gas ambients, and at temperatures ranging from near zero kelvins to a few hundred degrees Celsius. This was soon followed by the invention of the atomic force microscope (AFM) by Binnig, Quate and Gerber. The AFM is one of the foremost tools for imaging, measuring, and manipulating matter at the nanoscale. The information is gathered by "feeling" the surface with a mechanical probe. Piezoelectric elements that facilitate tiny but accurate and precise movements on (electronic) command enable the very precise scanning. These technological breakthroughs in the 80s and early 90s pushed the frontiers of microscale towards nanoscale. Soon thereafter in 1991 carbon nanotubes were discovered by Iijima [6] and Smalley [7] discovered the technique for uniform nanotube production. These discoveries made it possible to develop not just micro level but also nano level nanoelectromechanical systems (NEMS). This thesis deals with modeling the dynamics of only MEMS with NEMS being left for future research.

1.2 Overview of Modeling Complexities in the Micro Regime

Modeling of a MEMS is a vital first step for design or testing. Modeling incorporates a wide range of phenomena and their mutual interactions. By their very nature MEMS involve interaction of at least two different physical forces - electrical and mechanical. However, modern MEMS are not just limited to interacting electric and mechanical forces. Instead a plethora of force domains

[2]Both the inventors were awarded the Nobel Prize in 1986 for this invention

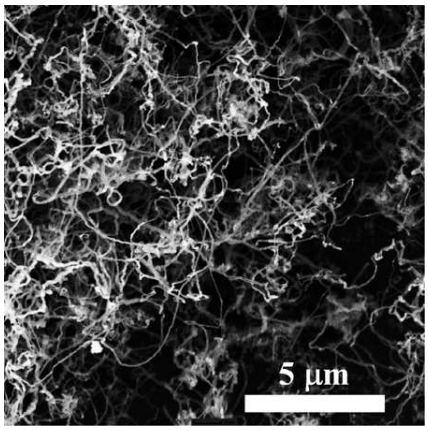

Figure 1.2: Carbon Nanotubes

may interact with each other in a single device requiring simultaneous modeling of electrostatic, mechanical, thermal, fluidic, magnetic or even chemical fields. This type of *coupled multiphysics* interaction results in a spectrum of rich behavior [8] in MEMS and at the same time makes the task of modeling extremely challenging. Real world engineering systems exist and perform in a universe of mutually intersecting force fields. The locus of design however considers only those which are able to exert appreciable effect on the system. Most forces scale differently with dimension [9]. For instance, whereas the spring force may be linear with respect to length scale, the electrostatic force is inverse square. However, the mathematics of scaling can bring about some curious advantages for microsystems making them suitable for a large number of engineering problems. One can take a simple example of a parallel plate capacitor of plate area A, gap d and dielectric constant ϵ_r. It is known that the maximum force between the plates is given by:

$$\begin{aligned} F_e &= \epsilon_0 \epsilon_r \frac{A(E_b d)^2}{d^2} \\ &= \epsilon_0 \epsilon_r A E_b^2 \end{aligned} \tag{1.1}$$

where E_b is the breakdown field and ϵ_0 the permittivity of the free space. One can assume that the switching speed is given by the agility of plate movements. A simple analysis can be done to show a remarkable improvement in switching speed achieved through geometric scaling. To start, one can use ideas from simple uniform rectilinear mechanics. Denoting time as t, displacement as x , acceleration as a, plate thickness as h, mass as m and mass density as ρ, the following equation can be obtained:

$$t = \sqrt{\frac{2x}{a}} = \sqrt{\frac{2mx}{F_e}} = \sqrt{\frac{2\rho A h x}{F_e}}. \tag{1.2}$$

Now, one can use the scaling laws $A \approx O(L^2)$, $h, x \approx O(L)$ and $F_e \approx O(A) \approx O(L^2)$ from Eq. (1.1) where L is the length scale. Plugging into Eq. (1.2), one gets, $t \approx O(L)$! Hence, switching time is proportional to length scale. Smaller the length scale, lower would be the switching time and higher would be the switching speed! Similar analysis on energy and traction can yield results endorsing the unique advantages of micro and submicro mechanisms and machines. Scaling laws have been used to explore new application possibilities of electroactive polymers in MEMS [10]. In addition, geometric scaling down can help us achieve a scaling up on the number of such devices in a given area which can open up other exciting phenomena [11].

1.3 Thesis Organization

The rest of the dissertation begins with a fully Lagrangian approach for modeling electrostatic MEMS without the damping effect of a surrounding fluid medium. The plate is simplified as a beam with uniform fields assumed across the depth. The electrostatic actuation force is obtained from relevant BEM equations and the thin beam is modeled as moderately large deformation FEM. The dynamic pullin phenomenon and the effect of various AC excitation frequencies have been studied and reported. The interesting competing roles of electrical softening and mechanical hardening has also been reported. It is important to note that the derivatives of the residuals necessary for the Newton method need to be very carefully obtained by analytical differentiation of the relevant integral and FEM equations. Chapter 3 deals with the effect of fluidic damping on the structure from the encapsulating fluidic medium. The fluid is assumed to follow Stokes flow equations due to small length scales involved. This assumption is verified by *a-posteriori* computation of the Reynolds number. A fully Lagrangian version of the fluidic equation was developed and integrated with the already developed electromechanical problem described in Chapter 2 through the continuity of velocity and equilibrium of traction. Numerical results for the beam vibrations both free (under DC bias) and forced by AC excitation are presented here for selected problems. A genuine numerical difficulty is encountered (requiring very small time steps and tighter tolerances for the Newton iteration) when the surrounding fluid is incompressible Stokes and the initial gap between the two beams is very small.

Chapter 4 addresses the edge singularity arising at the free end of the cantilever. An asymptotic formula is derived for the singularity from where the or-

der of singularity is derived. A singular element is then developed by enriching the shape function to better approximate the singular nature of the solution. The resultant singular formulation is then regularized assuming a straight geometry of the small element. A work equivalent charge distribution is then proposed to compute traction on the element. The solution of this singular problem is then presented and compared with simple extrapolation. Chapter 5 describes the conclusions and areas of future research. Extension to NEMS, acceleration using fast multipole methods(FMM) and uncertainty quantification issues are described.

BIBLIOGRAPHY

[1] Riordan M. and Hoddenson L. *Crystal Fire. The invention of the transistor and the birth of the information age*. W.W.Norton and Company, New York, 1998.

[2] Kilby J. S. Integrated semiconductor circuit device. US Patent 3,138,747, 1964.

[3] Moore G. E. Cramming more components onto integrated circuits. *Electronics Magazine*, 38(8), 1965.

[4] Feynamn R. P. There's plenty of room at the bottom. *Annual Meeting of the American Physical Society*, 1959.

[5] Drexler K. E. Protein design as a pathway to molecular manufacturing. *Proc. Natl. Acad. Sci.*, 78(9):5275–5278, September 1981.

[6] Iijima S. Helical microtubules of graphitic carbon. *Nature*, 354:56–58, 1991.

[7] Pavel Nikolaev Hongjie Dai Pierre Petit Jerome Robert Chunhui Xu Young Hee Lee Seong Gon Kim Andrew G. Rinzler Daniel T. Colbert Gustavo E. Scuseria David Tomnek John E. Fischer Richard E. Smalley Andreas Thess, Roland Lee. Crystalline ropes of metallic carbon nanotubes. *Science*, 273(5274):483–487, July 1996.

[8] De S. K. and Aluru S. K. Complex nonlinear oscillations in electrostatically actuated microstructures. *Journal of Microelectromechanical Systems*, 15(2):355–369, April 2006.

[9] Trimmer W. S. N. Microrobots and micromechanical systems. *Sensors and Actuators A*, 19:267–287, 1989.

[10] Liu C. and Bar-Cohen Y. Scaling laws of microactuators and potential applications of electroactive polymers in mems. *Proceedings of SPIE's 6th Annual International Symposium on Smart Structures and Materials*, pages 3669–33, 1999.

[11] Richard R. and Syms A. Scaling laws for mems mirro-rotation optical cross connect switches. *Journal of Lightwave Technology*, 20(7):1084–1094, 2002.

CHAPTER 2

FULLY LAGRANGIAN MODELING OF DYNAMICS OF MEMS WITH THIN BEAMS: UNDAMPED VIBRATIONS

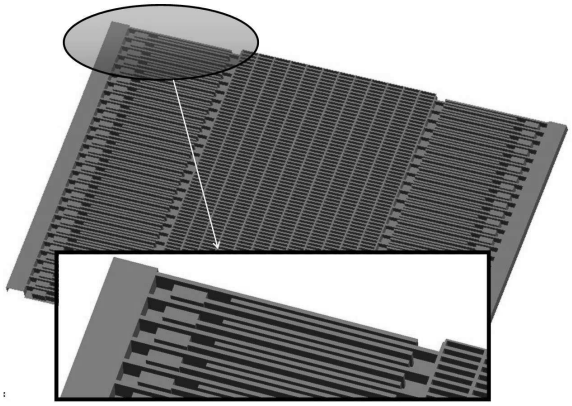

Figure 2.1: Parallel plate resonator: geometry and detail of the parallel plate fingers from [1]

The field of Micro-Electro-Mechanical Systems (MEMS) is a very broad one that includes fixed or moving microstructures; encompassing micro-electro-mechanical, microfluidic, micro-electro- fluidic-mechanical, micro-opto-electro-mechanical and micro-thermo-mechanical devices and systems. MEMS usually consists of released microstructures that are suspended and anchored, or captured by a hub-cap structure and set into motion by mechanical, electrical, thermal, acoustical or photonic energy source(s)

Typical MEMS structures consist of arrays of thin plates with cross-sections in the order of microns (μm) and lengths in the order of ten to hundreds of microns (See, for example, Fig. 2.1). Sometimes, MEMS structural elements are beams. An example is a small rectangular silicon beam with length in the order

[0]R. Ghosh and S. Mukherjee, Fully Lagrangian Modeling of Damped Vibrations of MEMS with Thin Beams - Part I: Undamped Vibrations , ASME Journal of Applied Mechanics, Volume 76, September 2009

of mm and thickness of the order of microns, that deforms when subjected to electric fields. Owing to its small size, significant forces and/or deformations can be obtained with the application of low voltages ($\approx$ 10 volts). Examples of devices that utilize vibrations of such beams are comb drives (see Fig. 2.1), synthetic micro-jets [2] - (for chemical mixing, cooling of electronic components, micro-propulsion, turbulence control and other macro flow properties), micros-peakers [3] etc.

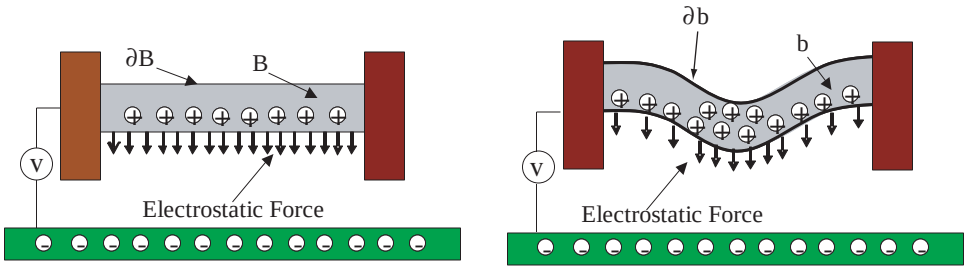

Figure 2.2: Deformable clamped beam over a fixed ground plate

Numerical simulation of electrically actuated MEMS devices have been carried out for nearly two decades using the Boundary Element Method (BEM - see, e.g. [4],[5], [6],[7] and [8]) to model the exterior electric field and the Finite Element Method (FEM - see, e.g. [9], [10],[11]) to model deformation of the structure. The commercial software package MEMCAD [12], for example, uses the commercial FEM software package ABAQUS for mechanical analysis, together with a BEM code FastCap [13] for the electric field analysis. Other examples of such work are [14], [15],[16]; as well as [12],[17] for dynamic analysis of MEMS.

The focus of this chapter is the study of dynamic response of MEMS devices made up of very thin conducting beams. This requires BEM analysis of the electric field exterior to these thin conducting beams. A convenient way to

model such a problem is to assume beams with vanishing thickness and solve for the sum of the charges on the upper and lower surfaces of each beam [18]. The standard Boundary Integral Equation (BIE) with a weakly singular kernel is used here and this approach works well for determining, for example, the capacitance of a parallel plate capacitor. For MEMS calculations, however, one must obtain the charge densities separately on the upper and lower surfaces of a beam since the traction at a surface point on a beam depends on the square of the charge density at that point. The gradient BIE is employed in [19] to obtain these charge densities separately. The formulation given in [19] is a BEM scheme that is particularly well-suited for MEMS analysis of very thin plates - for $h/L \approx 0.001$ - in terms of the length L (of a side of a square plate) and its thickness h . A similar approach has also been developed for MEMS and Nano Electro Mechanical Systems (NEMS) with very thin beams [20]. Similar work has also been reported by Chen et al. [21] in the context of determining fringing fields and levitating forces for 2-D beam shaped conductors in MEMS combdrives.

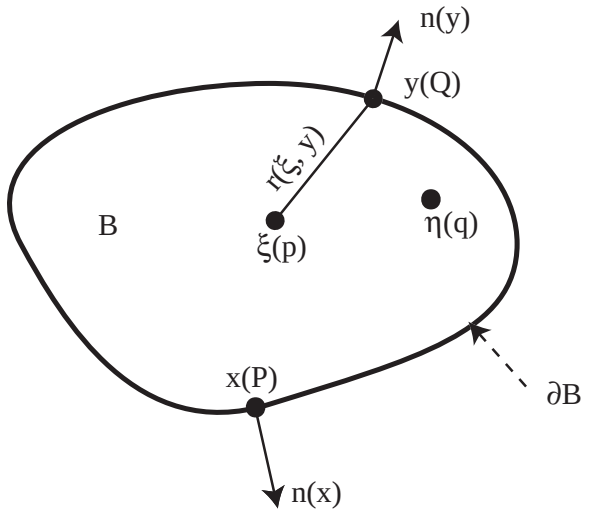

Figure 2.3: Notation used in boundary integral equations

The coupled BEM/FEM methods employed in many of the references cited above perform a mechanical analysis on the undeformed configuration of a structure (Lagrangian approach) and an electrical analysis on the deformed configuration (Eulerian approach). A relaxation method is then used for self-consistency between the two domains. Therefore, the geometry of the structure must be updated before an electrical analysis is performed during each relaxation iteration. This procedure increases computational effort and introduces additional numerical errors since the deformed geometry must be computed at every stage. Li and Aluru [22] first proposed a Lagrangian approach for the electrical analysis as well, thus obviating the need to carry out calculations based on the deformed shapes of a structure. Two and three-dimensional (2-D and 3-D) quasi-static Lagrangian exterior BEM analysis was addressed in [23] and [24]; while a fully coupled 2-D quasi-static MEMS analysis has been carried out in [22]. A fully-coupled 2-D dynamic Lagrangian MEMS analysis has been carried out by De and Aluru [25]. Additional advantages of the fully Lagrangian approach, for dynamic analysis of MEMS, are described in [25], in which a Newton method has been developed and compared with the relaxation scheme. It must be noted that [23],[22],[24],[25] and [26] employ a standard (not thin feature) BEM. Finally, quasi static deformation of thin plates, using the thin plate BEM is addressed in [27].

This chapter is an attempt to analyze and simulate vibrations of a practical MEM system involving a coupling of the electrical and mechanical problem. Additional coupling with fluid fields exterior to the system is considered in [28]. The external electric field is modeled using the Lagrangian version of the thin beam BEM approach [20] together with a hyper-singular post processing gradient BIE to find the individual charges. The mechanical problem is tackled using

a moderately large deflection FEM analysis. Finally, a Newton scheme developed analogous to [25] is used to solve the entire coupled nonlinear problem.

The chapter starts with regularization of the conventional and hypersingular BIEs for potential theory in an infinite region outside the thin conducting beams. The equations are then reformulated in a total Lagrangian framework. A finite element scheme is then presented for the mechanical deformation of the structure. The chapter then proceeds to explain the Newton scheme for coupling the electrical and mechanical domains. Numerical results are then presented and discussed. The chapter concludes with a section on discussions of the results and scope for future research.

2.1 Electrical Problem in the Exterior Domain

Fig. 2.2 shows (as an example of a MEMS device) a deformable, clamped beam over a fixed ground plane. The undeformed configuration is B with boundary ∂B. The beam deforms when a potential V is

applied between the two conductors, and the deformed configuration is called b with boundary ∂b. The charge redistributes on the surface of the deformed beam, thereby changing the electrical force on it and this causes the beam to deform further. The system then undergoes vibrations and the complete analysis of the system is done using the Newton scheme.

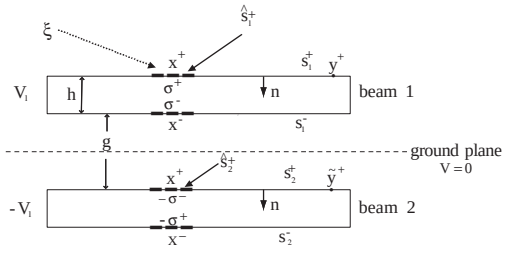

Figure 2.4: Two parallel conducting beams

2.1.1 Electric Field BIE in a Simply-Connected Body

The boundary element formulation of the electric problem can be derived from the Laplace equation which governs the potential in the region outside a conductor.

Conventional BIE - Indirect Formulation:

Referring to Fig 2.3, for a source point $\xi \in B$ (with bounding surface ∂B), one has the indirect BIE:

$$\phi(\xi) = \int_{\partial B} -\frac{\ln(r(\xi, \mathbf{y}))}{2\pi\epsilon} \nu(\mathbf{y}) ds(\mathbf{y}) \tag{2.1}$$

where $\mathbf{y}$ is a field point, ϕ is the potential, $r(\xi, \mathbf{y}) = \mathbf{y} - \xi$, $r = |\mathbf{r}|$, ϵ is the dielectric constant of the medium, ds is the area of an infinitesimal surface element on ∂B and ν is the (unknown) surface density function on ∂B.

Gradient BIE - Indirect Formulation:

Taking the derivative of the potential ϕ at the source point leads to an auxiliary hypersingular equation:

$$\nabla_\xi \phi(\xi) = \int_{\partial B} -\frac{\nu(\mathbf{y})}{2\pi\epsilon} \nabla_\xi \ln(r(\xi, \mathbf{y})) ds(\mathbf{y}) = \int_{\partial B} \frac{\nu(\mathbf{y}) \mathbf{r}(\xi, \mathbf{y})}{2\pi r^2(\xi, \mathbf{y})\epsilon} ds(\mathbf{y}) \tag{2.2}$$

Note that, in general, the function $\nu(\mathbf{y})$ is not the charge density. It becomes equal to the charge density when B is the infinite region exterior to the conductors. This is discussed in the next section.

2.1.2 BIEs in Infinite Region Containing Two Thin Conducting Beams

Now consider the situation shown in Fig. 2.4. Of interest is the solution of the following Dirichlet problem for Laplaces equation:

$$\nabla^2 \phi(\mathbf{x}) = 0, \quad \mathbf{x} \in B, \quad \phi(\mathbf{x}) \text{ prescribed for } \mathbf{x} \in \partial \mathbf{B} \tag{2.3}$$

where B is now the region *exterior* to the two beams. The unit normal $\mathbf{n}$ to B is defined to point away from B (i.e. into the beam).

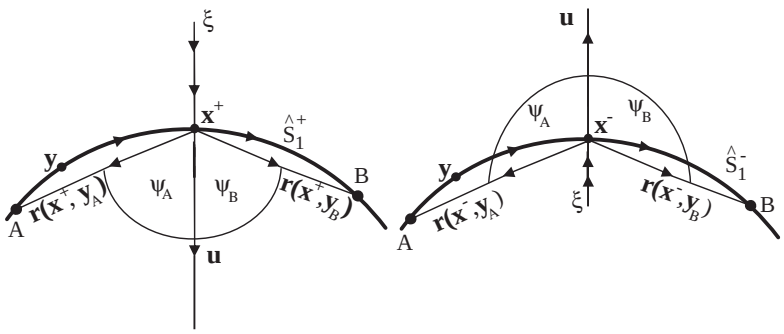

Figure 2.5: Evaluations of angles

Regular BIE - Source Point Approaching a Beam Surface s_1^+

It has been shown by Bao & Mukherjee [20] that for this case:

$$\phi(\mathbf{x}^+) = -\int_{s_1^+ - \hat{s}_1^+} \frac{\ln r(\mathbf{x}^+, \mathbf{y})\beta(\mathbf{y})}{2\pi\epsilon} ds(\mathbf{y}) - \int_{\hat{s}_1^+} \frac{\ln r(\mathbf{x}^+, \mathbf{y})\beta(\mathbf{y})}{2\pi\epsilon} ds(\mathbf{y}) - \int_{s_2^+} \frac{\ln r(\mathbf{x}^+, \mathbf{y})\beta(\mathbf{y})}{2\pi\epsilon} ds(\mathbf{y}). \quad (2.4)$$

Here $\beta(\mathbf{y}) = \sigma(\mathbf{y}^+) + \sigma(\mathbf{y}^-)$, where σ is now the charge density at a point on the beam surface. The second integral in Eq. (2.4) is logarithmically singular and the rest are regular except when the beam thickness and the gap become very small.

A similar equation can be written for $\mathbf{x}^+ \in s_2^+$. For the case shown in Fig. 2.4, however, it is not necessary since $\beta(\mathbf{y})$ is equal and opposite on the two beams. Therefore, for this case, Eq. (2.4) is sufficient to solve for β on both the beams.

Hypersingular BIE - Source Point Approaching a Beam Surface s_1^+

It is first noted that for $\mathbf{x}^+ \in s_k^+ \cup s_k^-,\ k = 1, 2$:

$$\sigma(\mathbf{x}) = \epsilon \frac{\partial \phi}{\partial n}(\mathbf{x}) = \epsilon \mathbf{n}(\mathbf{x}) \cdot [\nabla_\xi \phi(\xi)]_{\xi = x}. \quad (2.5)$$

Consider the limit $\xi \to \mathbf{x}^+ \in \hat{s}_1^+ \in s_1^+$. It is important to realize that this limit is meaningless for a point $\mathbf{x}$ on the edge of a beam, since the charge density is singular on its edges. One obtains the following HBIE:

$$\begin{aligned}\sigma(\mathbf{x}^+) = &\int_{s_1^+ - \hat{s}_1^+} \frac{\beta(\mathbf{y})\mathbf{r}(\mathbf{x}^+,\mathbf{y})\cdot\mathbf{n}(\mathbf{x}^+)}{2\pi r^2(\mathbf{x}^+,\mathbf{y})} ds(\mathbf{y}) \\ &+ \int_{\hat{s}_1^+} \frac{\mathbf{r}(\mathbf{x}^+,\mathbf{y})[\beta(\mathbf{y})\cdot\mathbf{n}(\mathbf{x}^+) - \beta(\mathbf{x})\cdot\mathbf{n}(\mathbf{y})]}{2\pi r^2(\mathbf{x}^+,\mathbf{y})} ds(\mathbf{y}) \\ &+ \frac{\beta(\mathbf{x})}{2\pi}\Psi(\hat{s}_1^+,\mathbf{x}^+) + \int_{s_2^+} \frac{\beta(\mathbf{y})\mathbf{r}(\mathbf{x}^+,\mathbf{y})\cdot\mathbf{n}(\mathbf{x}^+)}{2\pi r^2(\mathbf{x}^+,\mathbf{y})} ds(\mathbf{y}). \end{aligned} \tag{2.6}$$

In the above, the angle subtended by the line element s_1^+ at the point $\mathbf{x}^+$ (see [19],[20]) and Fig. 2.5 is:

$$\Psi(\hat{s}_1^+,\mathbf{x}^+) = \fint_{\hat{s}_1^+} \frac{\mathbf{r}(\mathbf{x}^+,\mathbf{y})\cdot\mathbf{n}(\mathbf{y})}{r^2(\mathbf{x}^+,\mathbf{y})} ds(\mathbf{y}) = \psi_A + \psi_B. \tag{2.7}$$

Here, the symbol $\fint$ denotes the finite part of the integral in the sense of Mukherjee [29]. Also (see Fig. 2.5), a unit vector $\mathbf{u}$, through the point $\mathbf{x}^+$, is chosen such that it intersects $\hat{s}_1^+$. Now, ψ is the angle between the positive $\mathbf{u}$ vector and $\mathbf{r}(\mathbf{x}^+,\mathbf{y})$ with $\mathbf{y} \in \hat{s}_1^+$. This angle can be obtained from the equation,

$$\cos(\psi(\mathbf{y})) = \frac{\mathbf{r}(\mathbf{x}^+,\mathbf{y})\cdot\mathbf{u}}{r(\mathbf{x}^+,\mathbf{y})} \tag{2.8}$$

Writing Eq. (2.6) at $\mathbf{x}^-$ together with some algebraic manipulation gives:

$$\begin{aligned}\frac{1}{2}[\sigma(\mathbf{x}^+) - \sigma(\mathbf{x}^-)] = &\int_{s_1^+ - \hat{s}_1^+} \frac{\beta(\mathbf{y})\mathbf{r}(\mathbf{x}^+,\mathbf{y})\cdot\mathbf{n}(\mathbf{x}^+)}{2\pi r^2(\mathbf{x}^+,\mathbf{y})} ds(\mathbf{y}) \\ &+ \int_{\hat{s}_1^+} \frac{\mathbf{r}(\mathbf{x}^+,\mathbf{y})[\beta(\mathbf{y})\cdot\mathbf{n}(\mathbf{x}^+) - \beta(\mathbf{x})\cdot\mathbf{n}(\mathbf{y})]}{2\pi r^2(\mathbf{x}^+,\mathbf{y})} ds(\mathbf{y}) \\ &- \frac{\beta(\mathbf{x})}{2\pi}[\pi - \Psi(\hat{s}_1^+,\mathbf{x}^+)] + \int_{s_2^+} \frac{\beta(\mathbf{y})\mathbf{r}(\mathbf{x}^+,\mathbf{y})\cdot\mathbf{n}(\mathbf{x}^+)}{2\pi r^2(\mathbf{x}^+,\mathbf{y})} ds(\mathbf{y}). \end{aligned} \tag{2.9}$$

Eq. (2.4) gives the sum of the charge densities and the HBIE Eq. (2.9) can

be used as a post-processing step to compute the values of individual charge densities on each of the beams.

2.1.3 Electrostatic Boundary Integral Equation in the Lagrangian Framework

Converting Eq. (2.4) and Eq. (2.9) in the Lagrangian framework can be started by using Nanson's law [30]:

$$\mathbf{n}ds = J\mathbf{N} \cdot \mathbf{F}^{-1}dS. \tag{2.10}$$

Here $\mathbf{n}$ and $\mathbf{N}$ are unit normal vectors to ∂b and ∂B, at the generic points $\mathbf{x}$ and $\mathbf{X}$, respectively, $\mathbf{F} = \frac{\partial \mathbf{x}}{\partial \mathbf{X}}$ is the deformation gradient, $J = det(\mathbf{F})$ and dS is an area element on ∂B. Also, $\mathbf{X}$ and $\mathbf{x}$ denote coordinates in the undeformed and deformed configurations, respectively. From Eq. (2.10), it follows that:

$$ds = J|\mathbf{N} \cdot \mathbf{F}^{-1}|dS. \tag{2.11}$$

Next, define Σ, the charge density per unit undeformed surface area. Since $\Sigma dS = \sigma ds$, one has:

$$\Sigma = J\sigma|\mathbf{N} \cdot \mathbf{F}^{-1}|. \tag{2.12}$$

Also define:

$$B = \Sigma^{+} + \Sigma^{-} \tag{2.13}$$

Lagrangian Version of the Regular BIE

Using the relations developed in the previous section, one arrives at the Lagrangian version of the Eq. (2.4),

$$\phi(\mathbf{X}^+) = -\int_{S_1^+ - \hat{S}_1^+} \frac{\ln R(\mathbf{X}^+, \mathbf{Y}) B(\mathbf{Y})}{2\pi\epsilon} dS(\mathbf{Y}) - \int_{\hat{S}_1^+} \frac{\ln R(\mathbf{X}^+, \mathbf{Y}) B(\mathbf{Y})}{2\pi\epsilon} dS(\mathbf{Y}) - \int_{S_2^+} \frac{\ln R(\mathbf{X}^+, \mathbf{Y}) B(\mathbf{Y})}{2\pi\epsilon} dS(\mathbf{Y}) \quad (2.14)$$

where:

$$\mathbf{r}(\mathbf{x}(\mathbf{X}), \mathbf{y}(\mathbf{Y})) \equiv \mathbf{R}(\mathbf{X}, \mathbf{Y}) = \mathbf{y}(\mathbf{Y}) - \mathbf{x}(\mathbf{X}) = \mathbf{Y} + \mathbf{u}(\mathbf{Y}) - \mathbf{X} - \mathbf{u}(\mathbf{X}) = \mathbf{R_0}(\mathbf{X}, \mathbf{Y}) + \mathbf{u}(\mathbf{Y}) - \mathbf{u}(\mathbf{X}) \quad (2.15)$$

$$\mathbf{R_0}(\mathbf{X}, \mathbf{Y}) = \mathbf{Y} - \mathbf{X} \quad (2.16)$$

$$r(\mathbf{x}(\mathbf{X}), \mathbf{y}(\mathbf{Y})) \equiv R(\mathbf{X}, \mathbf{Y}) = |\mathbf{R}(\mathbf{X}, \mathbf{Y})| \quad (2.17)$$

with $\mathbf{u}$ denoting the displacement at a point in B.

Also:

$$\mathbf{h}(\mathbf{y}) = -\frac{\sigma^2(\mathbf{y})}{2\epsilon}\mathbf{n} \quad (2.18)$$

$$\int_{\partial B} \mathbf{H} dS = \int_{\partial b} \mathbf{h} ds. \quad (2.19)$$

where $\mathbf{h}$ and $\mathbf{H}$ are the tractions per unit deformed and undeformed surface areas, respectively. Using Eq. (2.10), Eq. (2.11), Eq. (2.18) and Eq. (2.19), one gets:

$$\mathbf{H} = -\frac{J\sigma^2 \mathbf{N}\cdot\mathbf{F^{-1}}}{2\epsilon} = -\frac{\Sigma^2}{2J\epsilon}\frac{\mathbf{N}\cdot\mathbf{F^{-1}}}{|\mathbf{N}\cdot\mathbf{F^{-1}}|} \tag{2.20}$$

Lagrangian Version of the Gradient BIE

The Lagrangian version of the Eq. (2.9) is derived as follows,

$$First\,Term = \int_{S_1^+ - \hat{S}_1^+} \frac{B(\mathbf{Y})\mathbf{R}(\mathbf{X}^+,\mathbf{Y})\cdot\left(\frac{\mathbf{N}\cdot\mathbf{F^{-1}}}{|\mathbf{N}\cdot\mathbf{F^{-1}}|}\right)(\mathbf{X}^+)}{2\pi R^2(\mathbf{X}^+,\mathbf{Y})} dS(\mathbf{Y}) \tag{2.21}$$

$$\begin{aligned} Second\,Term = &\int_{\hat{S}_1^+} \frac{\mathbf{R}(\mathbf{X}^+,\mathbf{Y})B(\mathbf{Y})}{2\pi R^2(\mathbf{X}^+,\mathbf{Y})}\cdot\Big(\frac{\mathbf{N}\cdot\mathbf{F^{-1}}}{|\mathbf{N}\cdot\mathbf{F^{-1}}|}\Big)(\mathbf{X}^+)dS(\mathbf{Y}) \\ -\int_{\hat{S}_1^+} &\frac{\mathbf{R}(\mathbf{X}^+,\mathbf{Y})}{2\pi R^2(\mathbf{X}^+,\mathbf{Y})}\cdot\frac{B(\mathbf{X})}{J(\mathbf{X}^+)|\mathbf{N}\cdot\mathbf{F^{-1}}(\mathbf{X}^+)|}\cdot J(\mathbf{X}^+)(\mathbf{Y})(\mathbf{N}\cdot\mathbf{F^{-1}})(\mathbf{Y})dS(\mathbf{Y}) \end{aligned} \tag{2.22}$$

$$Third\,Term = -\frac{B(\mathbf{X})}{2\pi J(\mathbf{X}^+)|\mathbf{N}\cdot\mathbf{F^{-1}}|(\mathbf{X}^+)}[\pi - \Psi(\hat{S}_1^+,\mathbf{X}^+)] \tag{2.23}$$

The fourth term can be treated in the same way as the first. Now, multiply the entire equation by $J(\mathbf{X}^+)|\mathbf{N}\cdot\mathbf{F^{-1}}|(\mathbf{X}^+)$, use the mid-plane values[1] for $\mathbf{F}(\mathbf{X}^+) = \mathbf{F}(\mathbf{X}^-)$ and use the fact that $\mathbf{N}(\mathbf{X}^+) = -\mathbf{N}(\mathbf{X}^-)$ to simplify the equation further. The resulting equation has the form:

[1] Also called the membrane assumption

$$\frac{1}{2}[\Sigma(\mathbf{X}^+) - \Sigma(\mathbf{X}^-)] = \int_{S_1^+ - \hat{S}_1^+} \frac{B(\mathbf{Y})\mathbf{R}(\mathbf{X}^+, \mathbf{Y}) \cdot J(\mathbf{X}^+)(\mathbf{N} \cdot \mathbf{F^{-1}}(\mathbf{X}^+))}{2\pi R^2(\mathbf{X}^+, \mathbf{Y})} dS(\mathbf{Y})$$
$$+ \int_{\hat{S}_1^+} \frac{B(\mathbf{Y})\mathbf{R}(\mathbf{X}^+, \mathbf{Y}) \cdot J(\mathbf{X}^+)(\mathbf{N} \cdot \mathbf{F^{-1}}(\mathbf{X}^+))}{2\pi R^2(\mathbf{X}^+, \mathbf{Y})} dS(\mathbf{Y})$$
$$- \int_{\hat{S}_1^+} \frac{B(\mathbf{X})\mathbf{R}(\mathbf{X}^+, \mathbf{Y}) \cdot J(\mathbf{Y})(\mathbf{N} \cdot \mathbf{F^{-1}}(\mathbf{Y}))}{2\pi R^2(\mathbf{X}^+, \mathbf{Y})} dS(\mathbf{Y})$$
$$- \frac{B(\mathbf{X})}{2\pi}[\pi - \Psi(\hat{S}_1^+, \mathbf{X}^+)]$$
$$+ \int_{S_2^+} \frac{B(\mathbf{Y})\mathbf{R}(\mathbf{X}^+, \mathbf{Y}) \cdot J(\mathbf{X}^+)(\mathbf{N} \cdot \mathbf{F^{-1}}(\mathbf{X}^+))}{2\pi R^2(\mathbf{X}^+, \mathbf{Y})} dS(\mathbf{Y}) \quad (2.24)$$

It must be noted that the second and third terms must be evaluated together for numerical purposes. The angle can be easily computed from taking dot products of the position vectors of the required points on the surface of the body.

2.2 Mechanical Problem for the Elastic Beam

Nonlinear deformation of a beam with no initial axial force is discussed in this section. The beam is linearly elastic, has immovable ends and is of uniform cross section. The cross section is symmetric such that there is no twisting of the beam under applied bending moments. Also, $u(x)$ is the axial deformation and $w(x)$ the transverse displacement of the mid-line of the beam.

2.2.1 The Model

The kinematic equations can be derived starting from the nonlinear strain-displacement equation [31]leading to the following kinematic equations:

$$\epsilon_{xx} = u_{,x} + 1/2 \cdot (w_{,x})^2 \tag{2.25}$$

$$\kappa_x = -w_{,xx}. \tag{2.26}$$

Here, ϵ_{xx} is the midline axial strain and κ_x is the curvature. Also $_{,x}$ denotes the derivative with respect to the axial coordinate x. The strain energy $\mathcal{E}^{(s)}$ and the kinetic energy $\mathcal{E}^{(k)}$ of an uniform beam of length L are:

$$\mathcal{E}^{(s)} = \frac{ES}{2}\int_0^L [(u_{,x})^2 + u_{,x}(w_{,x})^2 + (1/4)(w_{,x})^4]dx + \frac{EI}{2}\int_0^L (w_{,xx})^2 dx \tag{2.27}$$

$$\mathcal{E}^{(k)} = \frac{\rho S}{2}\int_0^L [(\dot{u})^2 + (\dot{w})^2]dx. \tag{2.28}$$

Here, E, ρ, L, S, I are the Youngs modulus, density (mass per unit volume), length, area of cross section, and area moment of inertia of the cross section of the beam, respectively, and a superposed dot denotes differentiation with respect to time t. Similarly the work expression can be written as,

$$\mathcal{W} = \int_0^L (H_x du + H_y dw + M dw_{,x})dx. \tag{2.29}$$

Here H_x, H_y and M are the axial force, transverse force and bending moment, respectively.

2.2.2 Finite Element Model for Beams with Immovable Ends

The procedure followed here, for FEM discretization of vibrating beams, is similar to standard methods (see, e.g., Zienkiewicz and Taylor [10]). However, in

this particular problem the standard beam element needs a slight modification. This modification is necessitated because the usual linear interpolation for the axial deformation results in discontinuities during residual computation in the Newton's scheme. Hence, a quadratic interpolation is taken for the axial deformation. A standard Hermitian interpolation is used for bending . Hence, the beam element used in this present problem has a total of seven degrees of freedom; three axial at three axial nodes and two transverse and two rotational degrees of freedom at the end nodes. These degrees of freedom can be written as:

$$\begin{aligned} \mathbf{u} &= [u_1\ u_2\ u_3] \\ \mathbf{w} &= [w_1\ w_2] \\ \theta &= [w_{,x1}\ w_{,x2}] \end{aligned}$$

Now, the values of the primary deformations $\mathbf{u},\ \mathbf{w}$ inside the elements can be interpolated from the above nodal values using:

$$\begin{bmatrix} u(x,t) \\ w(x,t) \end{bmatrix} = \begin{bmatrix} N^{(I)}(x) & 0 \\ 0 & N^{(0)}(x) \end{bmatrix} \cdot \begin{bmatrix} q^{(I)}(t) \\ q^{(O)}(t) \end{bmatrix} \tag{2.30}$$

wherein

$$[N^{(I)}(x)] = [N_1\ N_2\ N_3], \qquad [N^{(O)}] = [P_1\ P_2\ P_3\ P_4] \tag{2.31}$$

$$[q^{(I)}(t)] = [u_1\ u_2\ u_3]^T, \qquad [q^{(O)}(t)] = [w_1\ \theta_1\ w_2\ \theta_2] \tag{2.32}$$

Here N_k and P_k are quadratic Lagrange and cubic (Hermite polynomials) interpolation functions, respectively and $q^{(I)}$ and $q^{(O)}$ contain the appropriate nodal degrees-of-freedom. Now, define:

$$D = w_{,x}, \quad [G] = [N^{(O)}_{,x}], \quad [B^{(I)}] = [N^{(I)}_{,x}] \quad [B^{(O)}] = -[N^{(O)}_{,xx}]. \tag{2.33}$$

Substitution of the interpolations from Eq. (2.30) into the work energy expressions from Eq. (2.27), Eq. (2.28) and Eq. (2.29) and use of Hamilton's principle leads to the following element level equations [32]:

$$\begin{bmatrix} M^{(I)} & 0 \\ 0 & M^{(0)} \end{bmatrix} \cdot \begin{bmatrix} \ddot{q}^{(I)}(t) \\ \ddot{q}^{(O)}(t) \end{bmatrix} + \begin{bmatrix} K^{(I)} & 0 \\ 0 & K^{(0)} \end{bmatrix} \cdot \begin{bmatrix} q^{(I)}(t) \\ q^{(O)}(t) \end{bmatrix} + \begin{bmatrix} 0 & K^{IO} \\ 2K^{(IO)T} & K^{(NI)} \end{bmatrix} \cdot \begin{bmatrix} q^{(I)}(t) \\ q^{(O)}(t) \end{bmatrix} = \begin{bmatrix} P^{(I)}(t) \\ P^{(O)}(t) \end{bmatrix}. \tag{2.34}$$

In the above:

$$[M^{(I)}] = \frac{\rho S}{2} \int_0^L [N^{(I)}]^T [N^{(I)}] dx$$
$$[M^{(I)}] = \frac{\rho S}{2} \int_0^L [N^{(O)}]^T [N^{(O)}] dx \tag{2.35}$$
$$[K^{(I)}] = ES \int_0^L [B^{(I)}]^T [B^{(I)}] dx$$
$$[K^{(O)}] = EI \int_0^L [B^{(O)}]^T [B^{(O)}] dx \tag{2.36}$$

$$[K^{(IO)}] = \frac{ES}{2} \int_0^L [B^{(I)}]^T [DG] dx$$
$$[K^{(NI)}] = \frac{ES}{2} \int_0^L [DG]^T [DG] dx \tag{2.37}$$

$$[P] = \int_0^L \begin{pmatrix} N^{(I)} & 0 \\ 0 & N^{(O)} \end{pmatrix}^T \begin{pmatrix} \overline{H}_x \\ \overline{H}_y \\ \overline{M} \end{pmatrix} dx \tag{2.38}$$

where L is the length of the finite element and $[\overline{H}]$ is the resultant traction on the mid-line of the beam. If one denotes $\xi = (I/S)^{1/2}$ as the radius of gyration of the beam cross-section, one can observe a few interesting points about the relations just derived. The in-plane (axial) and out-of-plane (bending) matrices $[K^{(I)}]$and $[K^{(O)}]$ are $\propto$ to S and $S\xi^2$, respectively, the matrix $[K^{(IO)}] \propto AS$ where A is the beam deflection, represents coupling between the axial and bending displacements, and the matrix $[K^{(NI)}] \propto A^2S$ arises purely from the nonlinear axial strains. It is well known that for the linear theory $K^{(O)} \ll K^{(I)}$ as $\xi \to 0$. It is very interesting, however, to note that if A/ξ remains $\mathcal{O}(1)$ (moderately large deformation), the bending matrix $K^{(O)}$, which arises from the linear theory, and the matrix $K^{(NI)}$ from the nonlinear theory, remain of the same order as $\xi \to 0$ [32].

2.3 Newton's Scheme for Solving the Coupled Problem

Newton's method is an iterative root-finding algorithm that uses the first few terms of the Taylor series of a function $f : \mathrm{R} \to \mathrm{R}$ in the vicinity of a suspected root. The algorithm can be written for a one dimensional case as,

$$x_{n+1} = x_n - \frac{f(x_n)}{f'(x_n)}, \qquad n \geq 0.$$

For the multivariate case, $\boldsymbol{f} : \mathrm{R}^p \to \mathrm{R}^p$,

$$\boldsymbol{x} \in \mathrm{R}^p : \boldsymbol{f}(\boldsymbol{x}) = \boldsymbol{0} \in \mathrm{R}^p$$

$$\boldsymbol{x}_{n+1} = \boldsymbol{x}_n - \boldsymbol{J}\boldsymbol{f}(\boldsymbol{x}_n)^{-1}\boldsymbol{f}(\boldsymbol{x}_n), \qquad n \geq 0 \tag{2.39}$$

where $\boldsymbol{J}\boldsymbol{f}(\boldsymbol{x})$ denotes the Jacobian of the function $\boldsymbol{f}(\boldsymbol{x})$. It is straightforward to re-cast Eq. (2.39) in the context of the current problem by replacing the vector function $\boldsymbol{f}(\boldsymbol{x})$ by the relevant vector function for the present problem.

2.3.1 Residuals and Their Gradients

Newton's scheme is used to solve the entire system of equations of the coupled electro-mechanical problem together. The relevant vector functions used in the present case are called residuals. Eq. (2.14) gives the electrical residual and Eq. (2.34) gives the mechanical residual. In addition, the auxiliary Eq. (2.24) is used in conjunction with Eq. (2.20) as an inter-domain coupling equation. It must be noted that the primary variables are B and $\mathbf{U} = [\mathbf{u}\ \mathbf{w}\ \theta]$ respectively, the electrical and mechanical variables.

The Electrical Residual and its Derivatives

The electrical residual can be formed from Eq . (2.14), as

$$\begin{aligned} R_E(\mathbf{U}, B) = \phi(\mathbf{X}^+) + \int_{S_1^+ - \hat{S}_1^+} \frac{\ln R(\mathbf{X}^+, \mathbf{Y}) B(\mathbf{Y})}{2\pi\epsilon} dS(\mathbf{Y}) \\ + \int_{\hat{S}_1^+} \frac{\ln R(\mathbf{X}^+, \mathbf{Y}) B(\mathbf{Y})}{2\pi\epsilon} dS(\mathbf{Y}) \\ + \int_{S_2^+} \frac{\ln R(\mathbf{X}^+, \mathbf{Y}) B(\mathbf{Y})}{2\pi\epsilon} dS(\mathbf{Y}). \end{aligned} \tag{2.40}$$

To compute the gradient of the electrical residual, one can rewrite Eq. (2.40) in a standard BEM form using a suitable interpolation functions:

$$\begin{pmatrix} \mathbf{R}_E(\mathbf{U}(\mathbf{X_1^+}), B(\mathbf{X_1})) \\ \vdots \\ \mathbf{R}_E(\mathbf{U}(\mathbf{X_N^+}), B(\mathbf{X_N})) \end{pmatrix} = \begin{pmatrix} \phi(\mathbf{X_1}^+) \\ \vdots \\ \phi(\mathbf{X_N}^+) \end{pmatrix} + \begin{pmatrix} \Upsilon_{11} & \dots & \Upsilon_{1N} \\ \vdots & \ddots & \vdots \\ \Upsilon_{N1} & \dots & \Upsilon_{NN} \end{pmatrix} \begin{pmatrix} B(\mathbf{X_1}) \\ \vdots \\ B(\mathbf{X_N}) \end{pmatrix} \quad (2.41)$$

where subscripts $1 \dots N$ denote the value of the variable at the corresponding node positions and $[\Upsilon]$ is the matrix of BEM integration constants which depends on both the geometry and interpolation functions used in the problem. One can differentiate Eq. (2.41) with respect to $B(\mathbf{X})$ and arrive at the following expression:

$$\frac{\partial R_E}{\partial \mathbf{B}}(\mathbf{U}, B) = [\Upsilon]. \quad (2.42)$$

The other residual can be computed by differentiating Eq. (2.40) with respect to the mechanical variable $\mathbf{U}$. Now using:

$$\frac{\partial R}{\partial \mathbf{U}(\mathbf{X})} = -\frac{\mathbf{R}}{R}, \qquad \frac{\partial R}{\partial \mathbf{U}(\mathbf{Y})} = \frac{\mathbf{R}}{R} \quad (2.43)$$

one gets:

$$\begin{aligned} \frac{\partial R_E}{\partial \mathbf{U}(\mathbf{X}^+)}(\mathbf{U}, B) &= -\int_{S_1^+ - \hat{S}_1^+} \frac{\mathbf{R}(\mathbf{X}^+, \mathbf{Y}) B(\mathbf{Y})}{2\pi\epsilon R^2} dS(\mathbf{Y}) \\ &\quad - \oint_{\hat{S}_1^+} \frac{\mathbf{R}(\mathbf{X}^+, \mathbf{Y}) B(\mathbf{Y})}{2\pi\epsilon R^2} dS(\mathbf{Y}) \\ &\quad - \int_{S_2^+} \frac{\mathbf{R}(\mathbf{X}^+, \mathbf{Y}) B(\mathbf{Y})}{2\pi\epsilon R^2} dS(\mathbf{Y}) \\ &\quad + \oint_{\hat{S}_1^+} \frac{\mathbf{R}(\mathbf{X}^+, \mathbf{Y}) B(\mathbf{X})}{2\pi\epsilon R^2} dS(\mathbf{Y}). \end{aligned} \quad (2.44)$$

The first three terms on the right hand side of Eq. (2.44) are obtained by applying Eq. $(2.43)_1$ to Eq. (2.40), while the last one is obtained by applying Eq. $(2.43)_2$

and using $\partial R_E/\partial \mathbf{U}|_{\mathbf{Y}=\mathbf{X}^+}$. The second and the fourth term on the right hand side of Eq. (2.44) can be combined into a single term:

$$-\int_{\hat{S}_1} \frac{\mathbf{R}(\mathbf{X}^+,\mathbf{Y})(B(\mathbf{Y})-B(\mathbf{X}))}{2\pi\epsilon R^2} dS(\mathbf{Y}) \tag{2.45}$$

which is only weakly singular.

The Mechanical Residuals and Their Gradients

The mechanical residual can be written as,

$$R_M(\mathbf{U},B) = \begin{bmatrix} M^{(I)} & 0 \\ 0 & M^{(0)} \end{bmatrix} \cdot \begin{bmatrix} \ddot{q}^{(I)}(t) \\ \ddot{q}^{(O)}(t) \end{bmatrix} + \begin{bmatrix} K^{(I)} & 0 \\ 0 & K^{(0)} \end{bmatrix} \cdot \begin{bmatrix} q^{(I)}(t) \\ q^{(O)}(t) \end{bmatrix} + \begin{bmatrix} 0 & K^{IO} \\ 2K^{(IO)T} & K^{(NI)} \end{bmatrix} \cdot \begin{bmatrix} q^{(I)}(t) \\ q^{(O)}(t) \end{bmatrix} - [P]. \tag{2.46}$$

The last term of the above equation is the load term and contains information of the electrical influence. Using Eq. (2.20) as well as the relations:

$$\overline{\mathbf{H}} = \mathbf{H}^+ + \mathbf{H}^-, \quad \mathbf{N} = \mathbf{N}^+ = -\mathbf{N}^-, \quad \mathbf{F} = \mathbf{F}^+ = \mathbf{F}^- \tag{2.47}$$

one gets:

$$\overline{\mathbf{H}} = -\frac{AB}{2J\epsilon} \frac{\mathbf{N}\cdot\mathbf{F}^{-\mathbf{1}}}{|\mathbf{N}\cdot\mathbf{F}^{-\mathbf{1}}|^2} \tag{2.48}$$

where $A = \Sigma^+ - \Sigma^-$.

From Eq. (2.46):

$$\frac{\partial R_M}{\partial B}(\mathbf{U}, B) = -\frac{\partial [P]}{\partial B}. \tag{2.49}$$

The gradient $\partial R_M/\partial \mathbf{U}$ has two parts. The first part comes from the first two terms of the right side of Eq. (2.46) (It must be noted from Eq. (2.32) that $[q^{(I)}]$ and $[q^{(O)}]$ involve the displacement components as well as twists. Also, the stiffness matrices $[K^{(IO)}]$ and $[K^{(NI)}]$ involve slopes.) The second part of the gradient requires evaluation of the derivative of the load vector which in turn involves computation of $\partial \mathbf{F}/\partial \mathbf{U}$ and $\partial J/\partial \mathbf{U}$, together with the application of the chain rule. For these computations, it is useful, in general, to use the formulae:

$$\frac{\partial F_{ij}}{\partial U_k} = \frac{\partial F_{ij}}{\partial X_m} F^{-1}_{mk}, \quad \frac{\partial J}{\partial U_k} = J \frac{\partial F_{ij}}{\partial U_k} F^{-1}_{ji}, \quad \frac{\partial \mathbf{F^{-1}}}{\partial \mathbf{U}} = -\mathbf{F}^{-1} \cdot \frac{\partial \mathbf{F}}{\partial \mathbf{U}} \cdot \mathbf{F}^{-1}. \tag{2.50}$$

It is noted that, in the present case, the deformation gradient can be written down as:

$$\mathbf{F} = \begin{bmatrix} 1 + u_{,x} & 0 \\ w_{,x} & 1 \end{bmatrix} \tag{2.51}$$

Now, with $w_{,x} = \theta$, one has:

$$\mathbf{F} = \begin{bmatrix} 1 + u_{,x} & 0 \\ \theta & 1 \end{bmatrix} \tag{2.52}$$

Also, $J = det(\mathbf{F}) = 1 + u_{,x}$.

Finally, the auxiliary equation Eq. (2.24) is viewed as,

$$\frac{1}{2}A = f(\mathbf{U}, B) \tag{2.53}$$

and is used within each Newton iteration.

2.4 Dynamic Analysis of MEMS

The computational procedures for dynamic analysis of MEMS are considered next. The governing equation for the dynamic response of MEMS is:

$$\mathbf{M}\ddot{\mathbf{U}}(t) + \mathbf{K}\mathbf{U}(t) = \mathbf{F}(\mathbf{U}(t), \Sigma(t)). \tag{2.54}$$

Here, $\mathbf{U}(t)$ is the displacement vector, $\Sigma(t)$ is the charge density and dots indicate time derivatives. $\mathbf{M}$ and $\mathbf{K}$ are respectively the consistent mass matrix and stiffness matrix. $\mathbf{F}(\mathbf{U}(t), \Sigma(t))$ represents the electrostatic force which depends on the charge distribution $\Sigma(t)$. Eq. (2.54) can be solved using several direct integration methods when the forces are linear in displacement [9]. However, many of these methods are not directly applicable to MEMS. Two methods applicable to MEMS analysis are the Central Difference Method and the Newmark Method. Eq. (2.54) is solved for $\mathbf{U}(t)$ with the initial conditions,

$$\begin{aligned} \mathbf{U}(0) &= \mathbf{0} \\ \dot{\mathbf{U}}(0) &= \mathbf{0} \end{aligned} \tag{2.55}$$

Now one can define $\dot{\mathbf{U}} = \mathbf{v}$, $\ddot{\mathbf{U}} = \mathbf{a}$ and discretize the time period $[0 \quad T]$ into $[t_1, t_2, \ldots, t_n, t_{n+1}, \ldots, t_N]$ with $t_1 = 0,\ t_N = T$. Consider a typical time interval $[t_n \qquad t_{n+1}]$. Assuming that the solution is known at time t_n, i.e. $[\mathbf{U_n}, \mathbf{v_n}, \mathbf{a_n}]$

are known, the unknown quantities at t_{n+1} are $[\mathbf{U_{n+1}}, \mathbf{v_{n+1}}, \mathbf{a_{n+1}}]$. In the present work, the Newmark method has been employed to update the variables.

2.4.1 The Newmark Method

The Newmark method [33] is a widely used time integration scheme for dynamic analysis in finite element modeling. There are various ways of implementing the Newmark scheme.The version which is used in the present work is called the $a-$form [11]. Define *predictors*:

$$\begin{aligned} \tilde{\mathbf{U}}_{\mathbf{n+1}} &= \mathbf{U_n} + \Delta t \mathbf{v_n} + \frac{\Delta t^2}{2}(1-2\beta)\mathbf{a_n} \\ \tilde{\mathbf{v}}_{\mathbf{n+1}} &= \mathbf{v_n} + (1-\gamma)\Delta t \mathbf{a_n}. \end{aligned} \tag{2.56}$$

The next step is to use the *predictors* to obtain the actual quantities,

$$\begin{aligned} \mathbf{U_{n+1}} &= \tilde{\mathbf{U}}_{\mathbf{n+1}} + \beta \Delta t^2 \mathbf{a_n} \\ \mathbf{v_{n+1}} &= \tilde{\mathbf{v}}_{\mathbf{n+1}} + \gamma \Delta t \mathbf{a_{n+1}}. \end{aligned} \tag{2.57}$$

Here β and γ are algorithmic parameters that are fine tuned for integration accuracy and numerical stability. For a discussion on the effect of these parameters on the performance on the algorithm, see [11].

To start the process, $\mathbf{a_0}$ can be calculated from:

$$\mathbf{M a_0} = -\mathbf{K U}(0) + \mathbf{F}(\mathbf{U}(0), \Sigma(0)). \tag{2.58}$$

To march forward in time for acceleration, one needs to solve the time discrete version of the dynamic Eq. (2.54):

$$\mathbf{M a}_{n+1} + \mathbf{K U}_{n+1} = \mathbf{F}(\mathbf{U}_{n+1}, \Sigma_{n+1}). \tag{2.59}$$

This equation set is nonlinear and would be solved using the Newton scheme.

2.4.2 Implicit Time Integration

Finally, time integration for the problem is implemented using the Newmark scheme utilizing Newton's scheme. The method follows closely from Belytschko et. al. [34]. Using the version of BEM derived in the current work, one can recast Eq. (2.54) as:

$$\mathbf{M}\ddot{\mathbf{U}}(t) + \mathbf{K}\mathbf{U}(t) = \mathbf{f}^{elec}(\mathbf{U}(t), B(t)). \tag{2.60}$$

Here $\mathbf{f}^{elec}(\mathbf{U}(t), B(t))$ denotes the entire force loading term obtained through BEM analysis of the electrostatic problem.

Now define:

$$\mathbf{R}(\mathbf{U}, B) = \begin{pmatrix} R_E \\ \\ R_M \end{pmatrix} \tag{2.61}$$

Here, $\mathbf{R}$ is the grand residual for the problem. The Newton iterative scheme is essentially:

$$\begin{pmatrix} \frac{\partial R_E}{\partial B} & \frac{\partial R_E}{\partial \mathbf{U}} \\ \\ \frac{\partial R_M}{\partial B} & \frac{\partial R_M}{\partial \mathbf{U}} \end{pmatrix}^{(k)} \cdot \begin{pmatrix} \Delta B \\ \\ \Delta \mathbf{U} \end{pmatrix}^{(k)} = - \begin{pmatrix} R_E \\ \\ R_M \end{pmatrix}^{(k)} \tag{2.62}$$

$$\mathbf{U}^{(k+1)} = \mathbf{U}^{(k)} + \Delta\mathbf{U}^{(k)}, \quad B^{(k+1)} = B^{(k)} + \Delta B^{(k)}. \tag{2.63}$$

Superscripts are used to denote the iteration step and subscripts for the Newmark integrator. Starting with $k = 0$, Eq. (2.62) is iterated until convergence. At convergence, $\mathbf{R}^{(k)} \equiv R(\mathbf{U^{(k)}}, B^{(k)}) \rightarrow \mathbf{0}$. This iteration helps one find the value of $\mathbf{a_n}$ needed at each step of time integration through an update of $\mathbf{U_n^{(k)}}$. The algorithm for the coupled scheme is described below.

1. Solve BEM on ∂B for applied voltage and compute the traction $\mathbf{H_0}$ from Eq. (2.20).
2. Set initial values of displacement $\mathbf{U_0}$ and velocity $\mathbf{v_0}$ to $\mathbf{0}$ and compute initial acceleration using $\mathbf{a_0} = \mathbf{M^{-1}H_0}$
3. Set $\mathbf{a}_{n+1}^{(0)} = \mathbf{a}_n, \mathbf{v}_{n+1}^{(0)} = \mathbf{v}_n$ and $\mathbf{U}_{n+1}^{(0)} = \mathbf{U}_n$.
4. Estimate $\tilde{\mathbf{U}}_{n+1}$ and $\tilde{\mathbf{v}}_{n+1}$ from $\mathbf{U}_n$ and $\mathbf{v}_n$using Eq. (2.56).
5. $B_{n+1}^{(0)} = B_n$
6. Set $k = 1$
7. Newton iteration for time step $n + 1$:
   (a) Use Eqs. (2.40) and (2.46) to compute the value of requisite residuals.$B = B_{n+1}^{(k)}, \mathbf{U} = \mathbf{U}_{n+1}^{(k)}$.
   (b) Use Eqs. (2.42) and (2.44) to get residual gradient for the electrical part, where $B = B_{n+1}^{(k)}, \mathbf{U} = \mathbf{U}_{n+1}^{(k)}$.
   (c) Similarly proceed to compute the other four gradients from the relevant equations
   (d) Update acceleration as $\mathbf{a}_{n+1}^{(k)} = 1/\beta\Delta t^2(\mathbf{U}_{n+1}^{(k)} - \tilde{\mathbf{U}}_{n+1})$ and $\mathbf{v}_{n+1}^{(k)} = \tilde{\mathbf{v}}_{n+1} + \gamma\Delta t\mathbf{a}_{n+1}^{(k)}$
   (e) $R_M^{(k)} = R_M^{(k)} + \mathbf{M}\mathbf{a}_{n+1}^{(k)}$ and $\partial R_M/\partial \mathbf{U}|^{(k)} = \partial R_M/\partial \mathbf{U}|^{(k)} + 1/(\beta\Delta t^2)\mathbf{M}$

(f) Plug the above residuals into Eq. (2.62) and solve for the increments.

(g) Use Eq. (2.63), to update the primary variables.

(h) Compute the tolerance, TOL $= \frac{||\mathbf{U}_{n+1}^{(k)} - \mathbf{U}_{n+1}^{(k-1)}||}{||\mathbf{U}_{n+1}^{(k-1)}||} \times 100\%$

(i) Update $k = k + 1$

(j) If tolerance is high, repeat from step (7).

8. $\mathbf{a}_{n+1} = \mathbf{a}_{n+1}^{(k)}, \mathbf{v}_{n+1} = \mathbf{v}_{n+1}^{(k)}, \mathbf{U}_{n+1} = \mathbf{U}_{n+1}^{(k)}$

9. $B_{n+1} = B_{n+1}^{(k)}$

10. $n = n + 1$ and repeat from step (3) till required time limit is reached.

2.5 Numerical Verification

2.5.1 Code Verification

The computer code for the thin beam Lagrangian BEM has been carefully verified at several stages.

BEM for Region Exterior to a Thin Flat Beam

The BEM code has been carefully verified by comparing the charge densities obtained with the values reported by Liu and Shen [35]. The charge density obtained at the mid point of the thin beam has been found to agree within 1% of that reported by [35] in the thin beam limit.

FEM for Thin Beam

The FEM formulation for deformable von Karman plates, presented earlier in [26] has been carefully verified and the code has also been independently verified for classical problems like bending deformation of beams and plates under uniform pressure.

FEM-BEM Coupling

FEM-BEM coupling has been carried out using Newton's method on the Lagrangian version and the results are discussed in the next section.

2.5.2 Thin Beam Dynamics

Material Properties

Material properties used for Silicon conductors are [36], [37]:

$$E = 169GPa, \qquad \nu = 0.22, \qquad \rho = 2231Kg/m^3, \qquad \epsilon = 8.85 \times 10^{-12}F/m. \tag{2.64}$$

Here, E, ν and ρ refer to the Young's modulus, Poisson's ratio and density of Silicon respectively whereas ϵ is the permittivity of free space. It is assumed that the anisotropy is negligible and the beam is made up of poly-silicon for this system.

The Problem

Dynamics of a MEMS beam (the silicon is doped so that it is a conductor), subjected to both DC and AC bias (electric field) is simulated using the BEM-FEM coupled approach described earlier in the chapter. Each beam is in clamped-clamped configuration and two beams are used in order to have a zero voltage ground plane (plane of symmetry) midway between them. The MEMS beam is $1000\mu m$ long, $40\mu m$ wide and $0.5\mu m$ in height. The initial gap (gap_0) is $5\mu m$. The transverse mid point deflection is denoted by w_{mid} and the amplitude of vibration of the mid point of the beam, corresponding to AC excitation frequency ω, is denoted by $Amp(\omega)$.

Results

Fig. 2.6 shows normalized deflection as a function of voltage for a quasi-static version with DC bias. The beam suffers instability when the gap reduces by approximately 57% of the initial value. This result agrees very well with results obtained using reduced order modeling [38].

Fig. 2.7 is a plot of normalized deflection as a function of voltage squared. Since electric force is proportional to the square of the voltage, the slope of this curve can be used to deduce the stiffness of the system. The presence of competing electrical and mechanical nonlinearities and their influence on the stiffness has been explained in [27]. The curve obtained here closely agrees with the results of the quasi-static 3D plate version of the problem [27].

The dynamic behavior of the beam under DC bias can be seen in Fig. 2.8. The time period in the plot refers to $T_p = 2\pi/\Omega_{Nat}$ where $\Omega_{Nat} = (4.73)^2(EI/\rho SL^4)^{1/2}$

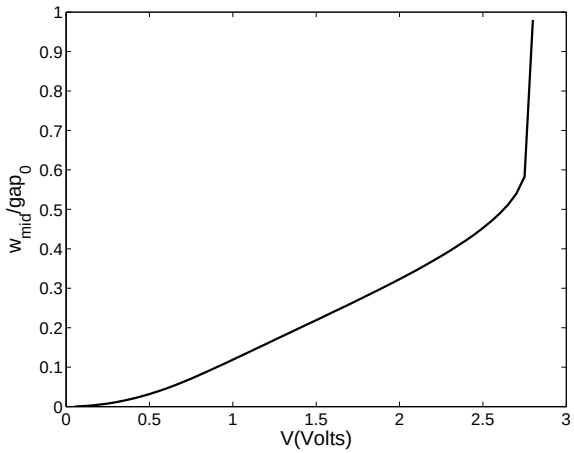

Figure 2.6: Response behavior of MEMS beam. Pull in Behavior

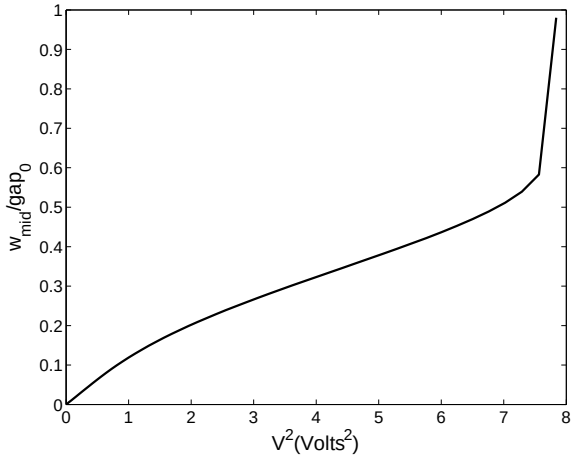

Figure 2.7: Response behavior of MEMS beam. Competing Nonlinearities

from the classical linear beam theory [39]. For the current beam geometry, $T_p \approx 226.75\mu s$. The frequency of vibration agrees within 1% with this value for a relatively low excitation voltage which limits the nonlinear effect. The MEMS beam can also be excited using AC excitation and its response is also studied. When excited close to the beam's natural frequency, the beat phenomenon can be clearly observed from Fig. 2.9. A more informative picture can be obtained by plotting the amplitude for various frequencies of AC excitation. Fig. 2.10

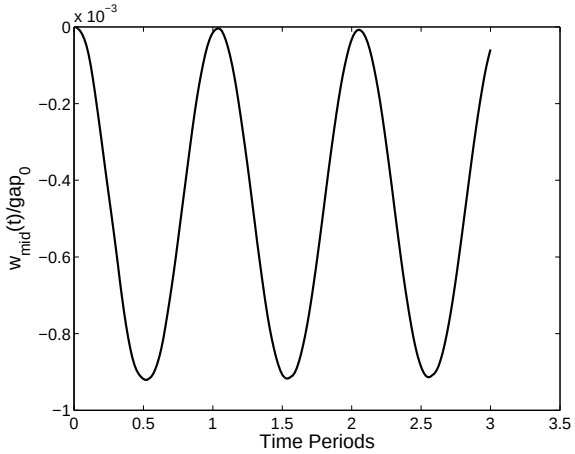

Figure 2.8: Vibration under a DC bias

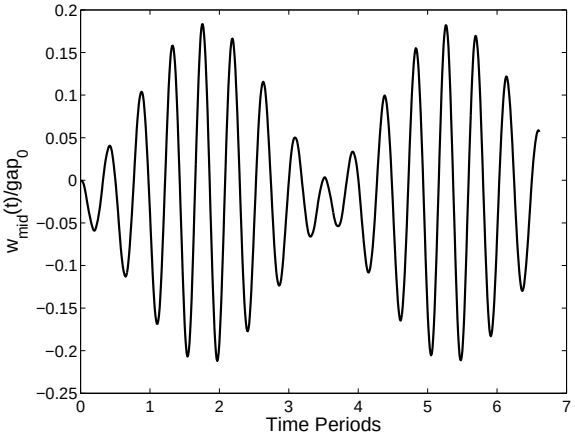

Figure 2.9: Beat phenomenon for near natural frequency excitation

shows the frequency response of the MEMS structure under a sinusoidal AC loading of constant amplitude and different frequencies. The curve has the characteristic flip-over profile with the peak. Since the electric force is proportional to the square of the applied voltage, the resonance peak occurs near half the natural frequency as shown in Fig. 2.10.

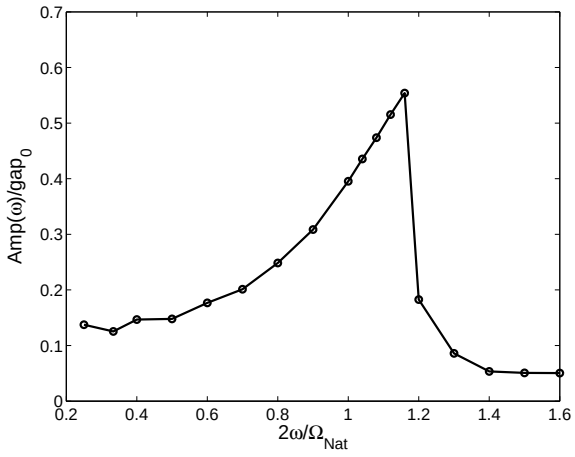

Figure 2.10: Amplitude-frequency response of a MEM beam

Comparisons With an Analogous Spring-Mass System

The amplitude-frequency diagram (Fig. 2.10) of the electrostatically actuated micro-beam problem dealt with here can be also be understood in terms of a simplified spring-mass system with a Duffing type cubic nonlinear spring attached to a rigid plate suspended over a ground plane illustrated in (Fig. 2.11). The electrostatic actuating force for such a system is known to be [40]:

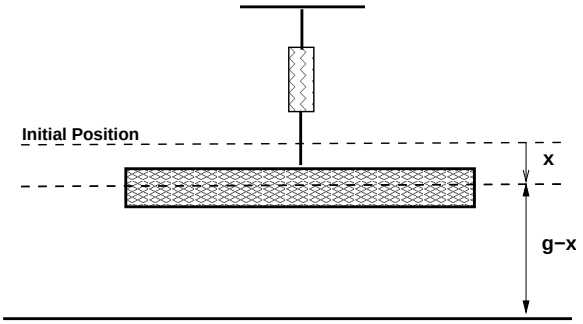

Figure 2.11: Idealization of MEMS Microbeam with Cubic Nonlinear Spring

$$F_e = \epsilon A \frac{V^2}{8(g-x)^2} \tag{2.65}$$

where F_e is the actuating electrostatic force, ϵ is the permittivity of the medium, A is the area of the plate, g the initial gap and x the current displacement of the plate from equilibrium position. Using this actuating force one can obtain the governing equation for the system:

$$m\ddot{x} = -k_1 x - k_2 x^3 + \epsilon A \frac{V^2}{8(g-x)^2} \tag{2.66}$$

where m is the plate mass, k_1, k_2 are the nonlinear stiffness of the spring and $V = V_0 \cos(\Omega_{App} t)$ is the AC excitation voltage. The preceding equation can be cast in the following dimensionless form:

$$\ddot{x}_* + \Omega_{Nat}^2 x_* + \beta {x_*}^3 - \gamma \frac{V_0^2 \cos(\Omega_{App} t)}{(1-x_*)^2} = 0 \tag{2.67}$$

where $x_* = x/g$, $\Omega_{Nat} = \sqrt{k_1/m}$, $\beta = k_2 g^2/m$ and $\gamma = \epsilon A/8mg^3$. For a fixed excitation amplitude V_0, one gets a normalized amplitude-frequency (δ_m/g vs $\Omega_{App}/\Omega_{Nat}$) curve where δ_m is the mid point displacement by sweeping through frequencies. On increasing V_0, the nonlinear effects become more pronounced. Hence, on varying the value of V_0, one obtains a family of such amplitude-frequency curves. One such plot of amplitude-frequency for a test system is shown in Fig. 2.12 where the initial conditions are beam at rest at its static equilibrium position. It is clear that the curve obtained in Fig. 2.10 resembles the curves with greater nonlinearities in Fig. 2.12. It must however be noted that the nonlinearities in this current system are not purely of classical Duffing type but has other nonlinear terms coming from the electrostatic forcing term. A detailed analysis of such MEMS vibrations is provided in [41] and [42].

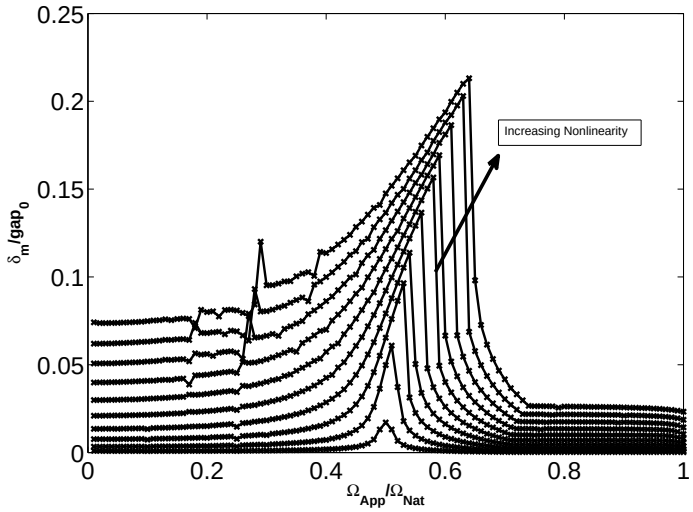

Figure 2.12: Frequency amplitude characteristic of an analogous spring-mass system

2.6 Conclusions

Free and forced vibrations of thin MEMS beams caused by applied DC and AC excitation have been studied in this work. The BEM (a special version suitable for thin features) is used to model the exterior electrostatic charge distribution and forces while the FEM is used to model moderately large deflections of thin beams. A fully Lagrangian description is employed for both the electrical and mechanical equations. Coupling of the BEM and FEM is carried out by the Newton scheme with time integration carried out by the Newmark method. Derivatives of the residuals necessary for the Newton method are carefully obtained by analytical differentiation of the relevant integral and FEM equations. Nonlinearities arise in this problem from the moderately large deflections of the beams, from the fact that the deformed shape of a beam affects the electrical forces on it, and the quadratic relationship between the charge density and the

corresponding traction. Damping caused by the presence of fluid exterior to the beams is included in a companion paper [28] in which a Stokes flow model is employed for the fluid flow.

The code developed to simulate the coupled electro-mechanical problem is carefully verified by comparison with other solutions reported in the literature. Numerical results for the beam vibrations both free (under DC bias) and forced by AC excitation are presented here for selected problems. The approach presented in this paper can be extended to study vibrations of MEMS with plates or NEMS with nanowires and nanotubes in a straightforward manner. A static deformation analysis of plates is presented in [27], while charge distribution on conducting carbon nanotubes and semi conducting silicon nanowires have been studied in recent work [43],[44].

Acknowledgments

This research has been supported by National Science Foundation Grant $\#CMS-0508466$ to Cornell University.

BIBLIOGRAPHY

[1] Frangi A. and di Gioa A. Multipole bem for evaluating damping forces on mems. *Comput. Mech.*, 37(1):24–31, December 2005.

[2] Roman M. and Aubry N. Design and fabrication of electrostatically actuated synthetic microjets. *ASME Paper No. IMECE2003-41579, New York, American Society of Mechanical Engineers*, 259:517–524, 2003.

[3] Ko S. C., Kim Y. C., Lee S. S., Choi S. S., and Kim S. R. Micromachined piezoelectric membrane acoustic device. *Sensors and Actuators A*, 103:130–134, 2003.

[4] Mukherjee S. *Boundary Element Methods in Creep and Fracture*. Applied Science Publishers, London, 1982.

[5] Banerjee P. K. *Boundary Element Methods in Engineering*. McGraw Hill, Europe, 1994.

[6] Chandra A. and Mukherjee S. *Boundary Element Methods in Manufacturing*. Oxford University Press, New York, 1997.

[7] Bonnet A. *Boundary Element Equation Methods for Solids and Fluids*. Wiley, Chichester, UK, 1999.

[8] Mukherjee S. and Mukherjee Y. X. *Boundary Methods: Elements, Contours and Nodes*. Taylor and Francis, CRC Press, Boca Raton, FL, 2005.

[9] Yang T. Y. *Finite Element Structural Analysis*. Prentice-Hall, Englewood Cliffs, New York, 1986.

[10] Zienkiewicz O. C. and Taylor R. L. *The Finite Element Method*, volume 1,2, 4th Ed. McGraw Hill, Berkshire, UK, 2005.

[11] Hughes T. J. R. *The Finite Element Method: Linear Static and Dynamic Finite Element Analysis*. Dover, Mineola, NY., 2000.

[12] Senturia S. D., Harris R. M., Johnson B. P., Kim S., Nabors K., Shulman M. A., and White J. K. A computer aided design system for microelectromechanical systems(memcad). *IEEE J. Microelectromech. Syst.*, 1:3–13, 1992.

[13] Nabors K. and White J. Fastcap: a multi-pole accelarated 3-d capcacitance extraction program. *IEEE Transcations in Computer Aided Design*, 10:1447–1459, 1991.

[14] Gilbert J. R., Legtenberg R., and Senturia S. D. 3d coupled electromechanics for mems: applications of cosolve-em. In *Proceedings, IEEE MEMS*, 1995.

[15] Shi F., Ramesh P., and Mukherjee S. Simulation methods for micro-electro-mechanical structures (mems) with applications to microtweezer. *Comp. Struct.*, 56:769–783, 1995.

[16] Aluru N. R. and White J. An efficient numerical technique for electromechanical simulation of complicated microelectromechancial structures. *Sens. Actuators A*, 58:1–11, 1997.

[17] Shi F., Ramesh P., and Mukherjee S. Dynamic analysis of micro-electro-mechanical systems. *Int. J. Num. Meth. Engng.*, 39:4119–4139, 1996.

[18] Harrington R. F. *Field computation by Moment Methods*. IEEE Press, Piscataway, NJ, 1993.

[19] Bao Z. and Mukherjee S. Electrostatic bem for mems with thin conducting plates and shells. *Eng. Anal. Bound. Elem.*, 28:1427–1435, 2004.

[20] Bao Z. and Mukherjee S. Electrostatic bem for mems with thin beams. *Comm. Numer. Meth. Engng.*, 21:297–312, 2005.

[21] Chuyan S. W., Liao Y. S., and Chen J. T. Computational study of the effect of finger width and aspect ratios for the electrostatic levitating force of mems comb drive. *IEEE J. Microelectromech. Syst.*, 14:305–312, 2005.

[22] Li G. and Aluru N. R. Efficient mixed-domain analysis of electrostatic mems. *IEEE Trans. Comput.-Aided Design*, 22:1228–1242, 2003.

[23] Li G. and Aluru N. R. A lagrangian approach for electrostatic analysis of deformable conductors. *J. Microelectromech. Syst.*, 11:245–254, 2002.

[24] Shrivastava V., Aluru N. R., and Mukherjee S. Numerical analysis of 3d electrostatics of deformable conductors using a lagrangian approach. *Eng. Anal. Bound. Elem.*, 28:583–591, 2004.

[25] De S. K. and Aluru N. R. Full-lagrangian schemes for dynamic analysis of electrostatic mems. *IEEE J. Microelectromech. Syst.*, 13, 2004.

[26] Mukherjee S., Bao Z., Roman M., and Aubry N. Nonlinear mechanics of mems plates with a total lagrangian approach. *Comp. Struct.*, 13:758–768, 2005.

[27] Telukunta S. and Mukherjee S. Fully lagrangian modeling of mems with thin plates. *IEEE J. Microelectromech. Syst.*, 15(4):795–810, 2006.

[28] Ghosh R. and Mukherjee S. Fully lagrangian modeling of dynamics of mems with thin beams – Part I: Undamped vibrations. *ASME J. Appl. Mech., submitted*, 2008.

[29] Mukherjee S. Finite parts of singular and hypersingular integrals with irregular boundary source points. *Eng. Anal. Bound. Elem.*, 24:767–776, 2004.

[30] Nanson E. J. Note on hydrodynamics. *The Messenger of Mathematics*, 7:182–183, 1877-1888.

[31] Reddy J. N. *Introduction to Nonlinear Finite Element Analysis*. Oxford University Press, USA, 2004.

[32] Bao Z., Mukherjee S., Roman M., and Aubry N. Nonlinear vibrations of beams, strings, plates and membranes without initial tension. *ASME J. App. Mech.*, 71(4):551–559, 2003.

[33] Newmark N. M. A method of computation for structural dynamics. *J. Engg. Mech. Div., ASCE*, pages 67–94, 1959.

[34] Belytschko T., Lui W. K., and Moran B. *Nonlinear Finite Element for Continua and Structures*. John Wiley & Sons, Ltd., 2000.

[35] Liu Y. J. and Shen L. A dual bie approach for large-scale modelling of 3-d electrostatic problems with the fast multipole boundary element method. *Int. J. Num. Meth. Engng.*, 71(7):837–855, 2007.

[36] Petersen K. E. Silicon as a mechanical material. In *Proceedings, IEEE*, volume 70, pages 420–455, 1982.

[37] Sharpe W. N. Jr. *Mechanical Properties of MEMS materials in The MEMS handbook*. CRC, Boca Raton, FL, 2001.

[38] Younis M. I., Abdel-Rahman E. M., and Nayfeh A. H. A reduced-order model for electrically actuated microbeam-based mems. *IEEE J. Microelectromech. Syst.*, 12(5):672–680, 2003.

[39] Hurty W. C. and Rubinstein M. F. *Dynamics of Structures*. Prentice Hall, Englewood Cliffs, New Jersey, 1964.

[40] Senturia S. D. *Microsystems Design*. Kluwer Academic Publishers, Boston, MA., 2001.

[41] K. L. Turner J. Moehlis B. E. DeMartini J. F. Rhoads, S. W. Shaw and W. Zhang. Generalized parametric resonance in electrostatically actuated microelectromechanical oscillators. *Journal of Sound and Vibration*, 296(4-5):797–829, Oct. 2006.

[42] De S. K. and Aluru S. K. Complex nonlinear oscillations in electrostatically actuated microstructures. *Journal of Microelectromechanical Systems*, 15(2):355–369, April 2006.

[43] Chen H. and Mukherjee S. Charge distribution on thin conducting nanotubes reduced 3-d model. *Int. J. Num. Meth. Engng.*, 68(5):503–524, 2006.

[44] Chen H., Mukherjee S., and Aluru N. Charge distribution on thin semiconducting silicon nanowire. *Comput. Methods Appl. Mech. Engrg., In Press*, 197:3366–3377, 2008.

CHAPTER 3

FULLY LAGRANGIAN MODELING OF DYNAMICS OF MEMS WITH THIN BEAMS: DAMPED VIBRATIONS

The field of Micro-Electro-Mechanical Systems (MEMS) is a very broad one that includes fixed or moving microstructures; encompassing micro-electro-mechanical, microfluidic, micro-electro- fluidic-mechanical, micro-opto-electro-mechanical and micro-thermal-mechanical devices and systems. MEMS usually consists of released microstructures that are suspended and anchored, or captured by a hub-cap structure and set into motion by mechanical, electrical, thermal, acoustical or photonic energy source(s)

Typical MEMS structures consist of arrays of thin plates with cross-sections in the order of microns (μm) and lengths in the order of ten to hundreds of microns . Sometimes, MEMS structural elements are beams. An example is a small rectangular silicon beam, with length in the order of mm and thickness of the order of microns, that deforms when subjected to electric fields. Owing to its small size, significant forces and/or deformations can be obtained with the application of low voltages ($\approx$ 10 volts). Examples of devices that utilize vibrations of such beams are comb drives , synthetic micro-jets ([1] - for chemical mixing, cooling of electronic components, micro-propulsion, turbulence control and other macro flow properties), microspeakers [2] etc. Numerical simulation of electrically actuated MEMS devices have been carried out for approximately a decade by using the Boundary Element Method (BEM - see, e.g. [3],[4], [5],[6] and [7]) to model the exterior electric field and the Finite Element Method (FEM

[0]R. Ghosh and S. Mukherjee, Fully Lagrangian Modeling of Damped Vibrations of MEMS with Thin Beams - Part II: Damped Vibrations , ASME Journal of Applied Mechanics, Volume 76, September 2009

- see, e.g. [8], [9],[10]) to model deformation of the structure. The commercial software package MEMCAD [11], for example, uses the commercial FEM software package ABAQUS for mechanical analysis, together with a BEM code FastCap [12] for the electric field analysis. Other examples of such work are [13], [14],[15]; as well as [11],[16] for dynamic analysis of MEMS.

The present chapter focuses on the influence of fluidic damping on the dynamic behavior of MEMS devices made up of very thin conducting beams. Analysis of the electro-mechanical problem has already been carried out in the companion paper [17]. Ye et.al. [18] have shown Stokes flow to be adequate for modeling the fluidic effects in MEMS systems. This model is used in the current chapter. A convenient way to model such a problem is to assume beams with vanishing thickness and recast the Boundary Integral Equations (BIE) in terms of sum of tractions and difference of velocities between the upper and lower surfaces respectively [19]. Further simplification can be obtained by noting that the difference of velocities between the upper and lower surfaces, for very thin beams, is negligible and the sum of tractions between upper and lower surfaces is equal to the net traction on the beam.

The BEM developed in the references cited above performs the electrical analysis on the deformed configuration (Eulerian approach). Therefore, the geometry of the structure must be updated before an electrical analysis is performed during each relaxation iteration. This procedure increases computational effort and introduces additional numerical errors since the deformed geometry must be computed at every stage. Hence, a Lagrangian approach which obviates the need to carry out calculations based on the deformed shapes of a structure [20], has been used in the current work. The fluid equations are then

coupled with the electric and mechanical equations developed in [17] to form a total Lagrangian version of the entire problem. Finally, a Newton scheme developed analogous to [21] is used to solve the entire coupled nonlinear problem.

The chapter starts with modeling of the fluid. The fluid is assumed to be Stokes. A conventional BIE representing the fluid is first presented and a thin beam approximation follows. The equations are then reformulated in a total Lagrangian framework. Weak fluid compressibility to reduce high stresses generated in very small gaps is discussed next. The chapter then proceeds to explain the Newton scheme for coupling the fluid domain with the electrical and mechanical domains. Numerical results are then presented and discussed. The chapter concludes with a section on discussions of the results and scope for future research.

3.1 Damping Problem in a Stokes Fluid

An extensive literature exists on the subject of damping forces in MEMS. The key issue, of course, is the choice of a particular mathematical model in order to calculate the damping forces correctly. Various options exist, such as a squeeze film model (e.g. [22]), an incompressible steady Stokes flow model (e.g. [23]), an incompressible oscillatory Stokes flow model (e.g. [18] and [24]), inclusion [24] or exclusion of slip at the solid/fluid interface, or molecular dynamics (MD) simulation (e.g. [25]). The last option must be employed if continuum theory breaks down, as often happens at the nanoscale or due to extreme rarefaction of the surrounding air at very low pressures. Sometimes, even if continuum theory does apply, a quasi-steady Stokes model may not due to very high resonant

frequencies (around 100 MHz [26]).

MEMS plates and beams, however, are typically tens to hundreds of micrometers long and with thickness in the order of micrometers [27]. There exists a regime where due to the micrometer-scales involved, the Reynolds numbers of the surrounding flow are generally small enough, and natural frequencies low enough (in the range of 100 s of kiloHertz) to allow the use of a steady-state Stokes flow (sometimes called creeping flow) model. Moreover, if the MEMS operate at pressures where the air can be treated as a continuum, the usual operating frequencies very often require an incompressible fluid model [23]. Further, in synthetic microjet applications, the medium surrounding the beam is typically a liquid for which an incompressible model is, of course, the appropriate one. Problems in which an incompressible steady-state Stokes model applies are of interest in this work. It is important to point out that numerical and experimental study of typical MEMS structures [18] demonstrates that a 3D, incompressible, no slip, oscillatory Stokes model can predict measured quality factors within 10%. Although only the steady Stokes model is employed in the present work, it is important to note that the forms of the integral equations used here remain unchanged for the oscillatory case, provided that the appropriate kernels for oscillatory flow are used in these integral equations ([18], [24]).

3.1.1 Governing Equations

As discussed above, the Reynolds numbers of the surrounding flow are generally small enough to allow for the use of a steady-state Stokes flow (sometimes

called creeping flow) model. The governing equations for the Stokes flow are:

$$\nabla p(\mathbf{x}) - \mu \nabla^2 \mathbf{v}(\mathbf{x}) = \mathbf{0}, \qquad \mathbf{x} \in B \tag{3.1}$$

$$\nabla \cdot \mathbf{v}(\mathbf{x}) = 0, \qquad \mathbf{x} \in B \tag{3.2}$$

$$\mathbf{v}(\mathbf{x}) = \mathbf{g}(\mathbf{x}), \qquad \mathbf{x} \in \partial B. \tag{3.3}$$

In the above, $\mathbf{v}$ is the velocity, p is the pressure and μ is the dynamic viscosity of the fluid. Also, B is the region *exterior* to the structure and ∂B is its boundary. The stress tensor σ inside the fluid, and the fluid surface traction τ on the solid surface, are defined by the equations,

$$\boldsymbol{\sigma}(\mathbf{x}) = -p(\mathbf{x})\mathtt{I} + \mu[\nabla \mathbf{v}(\mathbf{x}) + \nabla^T \mathbf{v}(\mathbf{x})], \qquad \mathbf{x} \in B \tag{3.4}$$

$$\boldsymbol{\tau}(\mathbf{x}) = \boldsymbol{\sigma}(\mathbf{x}) \cdot \mathbf{n}(\mathbf{x}), \qquad \mathbf{x} \in \partial B \tag{3.5}$$

where $\mathbf{n}$ is the unit outward normal to the fluid domain at a point on its boundary.

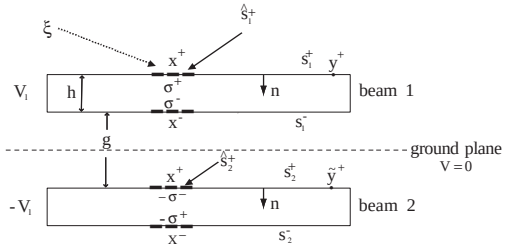

Figure 3.1: Two parallel beams in a surrounding Stokes fluid

3.1.2 Interface Conditions

In addition to the governing equations, interface conditions on the velocity $\mathbf{v}$ and traction $\boldsymbol{\tau}$ are required to simulate the coupled dynamics of MEMS devices. The interface conditions for the fluid-solid interface can be written as:

$$\begin{aligned} \mathbf{v}^f &= \mathbf{v}^s \\ \boldsymbol{\tau}^e - \boldsymbol{\tau}^f &= \boldsymbol{\tau}^s, \end{aligned} \tag{3.6}$$

where superscripts f, s denote the fluid and solid sides of the interface respectively, $\boldsymbol{\tau}^s$ is the total traction on the solid side and $\boldsymbol{\tau}^e$ and $\boldsymbol{\tau}^f$ are the electric and fluid parts of the traction.

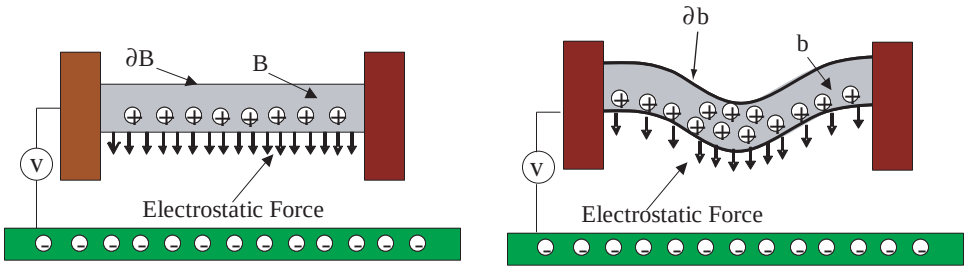

Figure 3.2: Deformable clamped beam over a fixed ground plate

3.1.3 Stokes Flow - Standard BIE Formulation

The general BIE formulation of the governing differential equations of the previous section can be written as [28]:

$$v_i(\mathbf{x}) = g_i(\mathbf{x}) = \fint_{\partial B} T_{ij}(\mathbf{x},\mathbf{y}) v_j(\mathbf{y}) ds(\mathbf{y})$$
$$+ \int_{\partial B} G_{ij}(\mathbf{x},\mathbf{y}) \tau_j(\mathbf{y}) ds(\mathbf{y}), \qquad \mathbf{x} \in \partial B \tag{3.7}$$

where the Green's function G is:

$$G_{ij}(\mathbf{x},\mathbf{y}) = \frac{1}{4\pi\mu}[-\delta_{ij} \ln r + r_{,i} r_{,j}] \tag{3.8}$$

and the traction kernel is:

$$T_{ij}(\mathbf{x},\mathbf{y}) = T_{ijk}(\mathbf{x},\mathbf{y}) n_k(\mathbf{y}) \tag{3.9}$$

with:

$$T_{ijk}(\mathbf{x},\mathbf{y}) = \frac{1}{\pi r} r_{,i} r_{,j} r_{,k} \tag{3.10}$$

In the above, $\mathbf{x}$ is a source point, $\mathbf{y}$ is a field point, r is the Euclidean distance between the source and field points, $r_{,i} = \partial r / \partial y_i = (y_i - x_i)/r$ and δ_{ij} are the components of the Kronecker delta. Also, the symbol $\fint$ denotes the finite part of the integral in the sense of Mukherjee [29],[30].

3.1.4 BIE in Stokes Flow in Infinite Region around Very Thin Beams

Analogous to the BIE for the electrostatic problem [31],[32], consider the flow in a region outside of, in this case, a single thin beam. (One beam is considered for simplicity of explanation - flow around many beams can also be easily modeled). It has been shown by Mukherjee et. al. [19] that for a thin beam, with

$\mathbf{x}^+ \in s^+$ (see Fig. 3.1),

$$v_i(\mathbf{x}^+) = g_i(\mathbf{x}^+) = \fint_{s^+} T_{ij}(\mathbf{x}^+, \mathbf{y}) w_j(\mathbf{y}) ds(\mathbf{y}) + \int_{s^+} G_{ij}(\mathbf{x}^+, \mathbf{y}) q_j(\mathbf{y}) ds(\mathbf{y}), \quad \mathbf{x}^+ \in s^+ \tag{3.11}$$

where $q_j = \tau_j^+ + \tau_j^-$, $w_j = v_j^+ - v_j^-$ and $s^+ = s_1^+ \cup s_2^+$.

For a thin beam $v_j^+ \approx v_j^-$, causing the first integral on the right hand side to disappear in Eq. (3.11). The above equations then simplifies to:

$$v_i(\mathbf{x}^+) = g_i(\mathbf{x}^+) = \int_{s^+} G_{ij}(\mathbf{x}^+, \mathbf{y}) q_j(\mathbf{y}) ds(\mathbf{y}), \qquad \mathbf{x}^+ \in s^+ \tag{3.12}$$

It has been shown by Mukherjee et.al. [19] that the null space of the kernel $\mathbf{G}$ in Eq. (3.12) is empty and this equation has a unique solution for any prescribed velocity $\mathbf{g}(\mathbf{x})$ on $\partial B = s^+ \cup s^-$. Thus Eq. (3.12) has the double advantage of avoiding ill behaved matrices resulting from thin structures and gaps, as well as singularities present in $\mathbf{G}$ in Eq. (3.7) ([28], [19]).

3.1.5 Lagrangian Version of the Stokes BIE

Using the same line of reasoning as for the electrical problem [17], one can derive the Lagrangian formulation of the Stokes flow BIE:

$$V_i(\mathbf{X}^+) = \int_{S^+} \frac{1}{4\pi\mu} \Big(- \delta_{ij} \ln R(\mathbf{X}^+, \mathbf{Y}) + \frac{R(\mathbf{X}^+, \mathbf{Y})_i R(\mathbf{X}^+, \mathbf{Y})_j}{R(\mathbf{X}^+, \mathbf{Y})^2} \Big) \overline{H}_j^{flu}(\mathbf{Y}) dS(\mathbf{Y}), \quad \mathbf{X}^+ \in S^+. \tag{3.13}$$

Here $R = R(\mathbf{X}^+, \mathbf{Y})$,$V_i(\mathbf{X}^+)$ and $\overline{H}_j^{flu}(\mathbf{Y})$ are respectively the Lagrangian description of the position, velocity and the resultant fluidic surface traction.

Please note that the resultant fluidic surface traction acting on the beam is $\mathbf{H}^{flu} = -\overline{\mathbf{H}}^{flu}$.

3.2 Compressible Stokes Flow

In view of the fact that real fluids are at least somewhat compressible (especially some gases), inclusion of compressibility in the Stokes flow model is investigated in this section (A similar model is used in [33] for a different reason). It is noted that inclusion of a small amount of compressibility in the model can help in convergence of the solutions by avoiding high stresses generated when the gap between two beams is very small ($gap \approx \mathcal{O}(0.005L)$).

It is first noted that the constitutive model for Stokes flow (Eq. (3.4)) is analogous to that for incompressible linear elasticity. This equation is now replaced by one analogous to that for compressible elasticity, i.e.:

$$\sigma(\mathbf{x}) = \lambda(\nabla \cdot \mathbf{v})\mathtt{I} + \mu[\nabla\mathbf{v}(\mathbf{x}) + \nabla^T\mathbf{v}(\mathbf{x})], \qquad \mathbf{x} \in B \tag{3.14}$$

where

$$\lambda = \frac{2\mu\nu}{1-2\nu}, \tag{3.15}$$

in terms of dynamic viscosity μ and a new material constant ν which is analogous to Poisson's ratio for linear elasticity. Also, K, analogous to bulk modulus, is:

$$K = \frac{2\mu(1+\nu)}{3(1-2\nu)} \tag{3.16}$$

and this is a measure of the compressibility of the fluid. It is well known that at the incompressibility limit $\nu \to \frac{1}{2}$ and both λ and $K \to \infty$.

Please note that Eq. (3.14) is identical to Eq. (1) in [33] where it is written in a different way by adding and subtracting the pressure term to the right hand side of Eq. (3.14).

The previous BIE formulation (Eq. (3.12)) remains the same except that instead of (Eq. (3.8)) one has:

$$G_{ij}(\mathbf{x},\mathbf{y}) = \frac{1}{8\pi(1-\nu)\mu}[-(3-4\nu)\ln(r)\delta_{ij} + r_{,i}r_{,j}] \tag{3.17}$$

One can note that Eq. (3.17) reduces to Eq. (3.8) when $\nu \to \frac{1}{2}$.

3.3 Newton's Scheme for Solving the Coupled Problem

Newton's method is an iterative root-finding algorithm that uses the first few terms of the Taylor series of a function $f : \mathrm{R} \to \mathrm{R}$ in the vicinity of a suspected root. The algorithm can be written for a one dimensional case as,

$$x_{n+1} = x_n - \frac{f(x_n)}{f'(x_n)}, \qquad n \geq 0.$$

For the multivariate case, $\boldsymbol{f} : \mathrm{R}^p \to \mathrm{R}^p$,

$$\boldsymbol{x} \in \mathrm{R}^p : \boldsymbol{f}(\boldsymbol{x}) = \mathbf{0} \in \mathrm{R}^p$$

$$\boldsymbol{x}_{n+1} = \boldsymbol{x}_n - \boldsymbol{J}\boldsymbol{f}(\boldsymbol{x}_n)^{-1}\boldsymbol{f}(\boldsymbol{x}_n), \qquad n \geq 0 \tag{3.18}$$

where $\boldsymbol{J}\boldsymbol{f}(\boldsymbol{x})$ denotes the Jacobian of the function $\boldsymbol{f}(\boldsymbol{x})$. It is straightforward to re-cast Eq. (3.18) in the context of the current problem by replacing the vector function $\boldsymbol{f}(\boldsymbol{x})$ by the relevant vector function for the present problem.

3.3.1 Coupled MEMS System

The system of interest in the present chapter is a thin MEMS beam electrically actuated and vibrating in a fluid medium. The electro-mechanics of a typical system has been analyzed in [17] and the introduction of fluidic effects in this chapter completes the full analysis of such a system. Fig. 3.2 shows (as an example of such a MEMS device) a deformable, clamped beam over a fixed ground plane. The undeformed configuration is B with boundary ∂B. The beam deforms when a potential V is applied between the two conductors, and the deformed configuration is called b with boundary ∂b. The charge redistributes on the surface of the deformed beam, thereby changing the electrical force on it and this causes the beam to deform further. As the deformation starts, the damping effects due to fluids come into play. The system then undergoes vibrations and the complete analysis of the system is carried out using the Newton scheme. The coupling of the mechanical and fluid equations involve continuity of velocity and equilibrium of traction. The fluid traction at the interface contributes as an additional external fluid force on the beam (see Eq. (3.6)).

3.3.2 Residuals and Their Gradients

The Newton scheme is used to solve equations for the entire system of the coupled electro-mechanical-fluid problem together. The relevant vector functions used in the present case are called residuals which can be formed using the relevant governing equations as shown in the companion paper [17]. For the sake of brevity the electrical, mechanical and fluidic variables are denoted as E, M, F. Hence, the residuals are denoted respectively as: R_E, R_M and R_F. The gradient

notation follows as: $\partial R_E/\partial B = R_{EE}$, $\partial R_E/\partial \mathbf{U} = R_{EM}$, $\partial R_E/\partial \mathbf{H}^{flu} = R_{EF}$, and so on.

The Electrical Residual and its Derivatives

One can recall from [17],

$$\begin{aligned} R_E(\mathbf{U}, B) = \phi(\mathbf{X}^+) + \int_{S_1^+ - \hat{S}_1^+} \frac{\ln R(\mathbf{X}^+, \mathbf{Y}) B(\mathbf{Y})}{2\pi\epsilon} dS(\mathbf{Y}) \\ + \int_{\hat{S}_1^+} \frac{\ln R(\mathbf{X}^+, \mathbf{Y}) B(\mathbf{Y})}{2\pi\epsilon} dS(\mathbf{Y}) \\ + \int_{S_2^+} \frac{\ln R(\mathbf{X}^+, \mathbf{Y}) B(\mathbf{Y})}{2\pi\epsilon} dS(\mathbf{Y}). \end{aligned} \tag{3.19}$$

where B is the sum of charges of the upper and lower surface of a thin beam, ϵ is the permittivity of the medium and ϕ the electric potential (voltage) on the surface. From the physics of the problem, it is clear that there is no direct influence of fluidic variables on the electric field and hence one can at once deduce that R_{EE} and R_{EM} remain the same as in [17], and:

$$R_{EF} = \frac{\partial R_E}{\partial \mathbf{H}^{flu}} = [0]. \tag{3.20}$$

The Mechanical Residuals and Their Gradients

The mechanical residual can be formed along the lines of [17] except that the force due to the fluid is added to the forcing term. One can recall from [17] that the mechanical residual can be written as:

$$R_M(\mathbf{U}, B, \mathbf{H}^{flu}) = \begin{bmatrix} M^{(I)} & 0 \\ 0 & M^{(0)} \end{bmatrix} \cdot \begin{bmatrix} \ddot{q}^{(I)}(t) \\ \ddot{q}^{(O)}(t) \end{bmatrix} + \begin{bmatrix} K^{(I)} & 0 \\ 0 & K^{(0)} \end{bmatrix} \cdot \begin{bmatrix} q^{(I)}(t) \\ q^{(O)}(t) \end{bmatrix} + \begin{bmatrix} 0 & K^{IO} \\ 2K^{(IO)T} & K^{(NI)} \end{bmatrix} \cdot \begin{bmatrix} q^{(I)}(t) \\ q^{(O)}(t) \end{bmatrix} - [P] \quad (3.21)$$

The last term of the above equation is the load term and contains electrical and fluidic forces:

$$[P] = [P]^{elec} + [P]^{flu} = \int_0^L \begin{pmatrix} N^{(I)} & 0 \\ 0 & N^{(O)} \end{pmatrix}^T \begin{pmatrix} \overline{H}_x^{elec} \\ \overline{H}_y^{elec} \\ \overline{M}_x^{elec} \end{pmatrix} - \int_0^L \begin{pmatrix} N^{(I)} & 0 \\ 0 & N^{(O)} \end{pmatrix}^T \begin{pmatrix} \overline{H}_x^{flu} \\ \overline{H}_y^{flu} \\ \overline{M}_x^{flu} \end{pmatrix} \quad (3.22)$$

where $elec$ and flu superscripts denote respectively the electrical and fluidic components of tractions and forces.

It can be deduced that R_{ME} remains same as in [17]. R_{MM} also remains the same assuming that $\overline{\mathbf{H}}^{flu}$ does not depend on $\mathbf{U}$. The remaining gradient R_{MF} would entail the computation of $\partial R_M / \partial \mathbf{H}^{flu} = -\partial[P]/\partial \mathbf{H}^{flu}$. The load has two parts, electrostatic and the fluidic. The fluidic part alone contributes to the gradient. One can note using a suitable finite element interpolation:

$$\mathbf{P}^{flu}(\mathbf{x}) = bL[N(\mathbf{x})]\{\mathbf{H}^{flu}\}, \quad (3.23)$$

where b, L are beam depth and length, $\mathbf{P}^{flu}$ is the fluid force, $[N(\mathbf{x})]$ is a suitable interpolation matrix and $\{\mathbf{H}^{flu}\}$ is the nodal fluid traction. Using Eq. (3.23), one can compute R_{MF}:

$$\partial R_{MF} = R_M/\partial \mathbf{H}^{flu} = -\partial[P]/\partial \mathbf{H}^{flu} = -\partial \mathbf{P}^{flu}/\partial \mathbf{H}^{flu} = -bL[N(\mathbf{x})] \qquad (3.24)$$

The Fluidic Residuals and Their Gradients

The fluidic residual can be written as:

$$R_{Fi}(\mathbf{U}, \mathbf{H^{flu}}) = V_i(\mathbf{X}^+) + \int_{S^+} \frac{1}{4\pi\mu}\Big(- \delta_{ij} \ln R(\mathbf{X}^+, \mathbf{Y}) + \frac{R(\mathbf{X}^+, \mathbf{Y})_i R(\mathbf{X}^+, \mathbf{Y})_j}{R(\mathbf{X}^+, \mathbf{Y})^2}\Big) H_j^{flu}(\mathbf{Y}) dS(\mathbf{Y}), \quad \mathbf{X}^+ \in S^+. \qquad (3.25)$$

where the index i denotes the component of the residual (axial or transverse). The above equation confirms the lack of coupling between the fluid and electric fields and hence $R_{FE} = 0$. Computing R_{FF} requires the computation of the gradient of Eq. (3.25) with respect to H_k^{flu}:

$$\frac{\partial R_{Fi}}{\partial H_j^{flu}}(\mathbf{X}^+) = \int_{S^+} \frac{1}{4\pi\mu}\Big(- \delta_{ij} \ln R(\mathbf{X}^+, \mathbf{Y}) + \frac{R(\mathbf{X}^+, \mathbf{Y})_i R(\mathbf{X}^+, \mathbf{Y})_j}{R(\mathbf{X}^+, \mathbf{Y})^2}\Big) dS(\mathbf{Y}). \qquad (3.26)$$

Finally, finding the residual with respect to the mechanical domain, R_{FM} needs computing gradient with respect to the displacement $\mathbf{U}$ variable. One can rewrite Eq. (3.25) as:

$$R_{Fi}(\mathbf{U}, \mathbf{H^{flu}}) = V_i(\mathbf{X}^+) + \int_{S^+} \frac{1}{4\pi\mu} K_{ij}(\mathbf{X}^+, \mathbf{Y}) H_j^{flu}(\mathbf{Y}) dS(\mathbf{Y}) \qquad (3.27)$$

where:

$$K_{ij}(\mathbf{X}^+, \mathbf{Y}) = -\delta_{ij} \ln R(\mathbf{X}^+, \mathbf{Y}) + \frac{R(\mathbf{X}^+, \mathbf{Y})_i R(\mathbf{X}^+, \mathbf{Y})_j}{R(\mathbf{X}^+, \mathbf{Y})^2}. \qquad (3.28)$$

Now one can write:

$$\frac{\partial K_{ij}(\mathbf{X}^+, \mathbf{Y})}{\partial U_k(\mathbf{X}^+)} = D_{ijk}(\mathbf{X}^+, \mathbf{Y}) \qquad (3.29)$$

where:

$$D_{ijk} = \frac{\delta_{ij}R_k}{R^2} - \frac{\delta_{ik}R_j}{R^2} - \frac{\delta_{jk}R_i}{R^2} + 2\frac{R_iR_jR_k}{R^4} \tag{3.30}$$

Following the derivation of Eq. (46) in [17]:

$$\begin{aligned}\frac{\partial R_{Fi}(\mathbf{U}, \mathbf{H^{flu}})}{\partial U_k(\mathbf{X}^+)} = &\int_{S_1^+ - \hat{S}_1^+} \frac{1}{4\pi\mu} D_{ijk}(\mathbf{X}^+, \mathbf{Y}) H_j^{flu}(\mathbf{Y}) dS(\mathbf{Y}) \\ &+ \int_{S_2^+} \frac{1}{4\pi\mu} D_{ijk}(\mathbf{X}^+, \mathbf{Y}) H_j^{flu}(\mathbf{Y}) dS(\mathbf{Y}) \\ + \int_{\hat{S}_1^+} \frac{1}{4\pi\mu} D_{ijk}(\mathbf{X}^+, \mathbf{Y}) &(H_j^{flu}(\mathbf{Y}) - H_j^{flu}(\mathbf{X})) dS(\mathbf{Y})\end{aligned} \tag{3.31}$$

3.4 Dynamic Analysis of MEMS

We are now in a position to consider the computational procedures for dynamic analysis of MEMS. The governing equation for the dynamic response of the MEMS system is:

$$\mathbf{M}\ddot{\mathbf{U}}(t) + \mathbf{K}\mathbf{U}(t) = \mathbf{F}^{elec}(B(t), \mathbf{U}(t)) + \mathbf{F}^{flu}(\mathbf{H}^{flu}(t)). \tag{3.32}$$

Here, $\mathbf{U}$ is the displacement vector and dots indicate time derivatives. $\mathbf{M}$ and $\mathbf{K}$ are respectively the consistent mass matrix and stiffness matrix. $\mathbf{F}^{elec}(B(t))$ represents the electrostatic force which depends on the charge distribution $B(t)$ and $\mathbf{F}^{flu}$ represents the fluidic force vector which depends on the traction distribution $\mathbf{H}^{flu} = \mathbf{H}^{flu}(\dot{\mathbf{U}})$ where $\dot{\mathbf{U}}$ is the velocity vector. Eq. (3.32) can be solved using several direct integration methods when the forces are linear in displacement [8]. However, many of these methods are not directly applicable to MEMS. Two methods applicable to MEMS analysis are the Central Difference Method and the Newmark Method. Eq. (3.32) is solved for $\mathbf{U}(t)$ with the initial

conditions,

$$\begin{aligned} \mathbf{U}(0) &= \mathbf{0} \\ \dot{\mathbf{U}}(0) &= \mathbf{0} \end{aligned} \tag{3.33}$$

Now one can define $\dot{\mathbf{U}} = \mathbf{v}$, $\ddot{\mathbf{U}} = \mathbf{a}$ and discretize the time period $[0 \quad T]$ into $[t_1, t_2, \ldots, t_n, t_{n+1}, \ldots, t_N]$ with $t_1 = 0,\ t_N = T$. Consider a typical time interval $[t_n \qquad t_{n+1}]$. Assuming that the solution is known at time t_n, i.e. $[\mathbf{U_n}, \mathbf{v_n}, \mathbf{a_n}]$ are known, the unknown quantities at t_{n+1} are $[\mathbf{U_{n+1}}, \mathbf{v_{n+1}}, \mathbf{a_{n+1}}]$. In the present work, the Newmark method has been employed to update the variables.

3.4.1 The Newmark Method

The Newmark method [34] is a widely used time integration scheme for dynamic analysis in finite element modeling. There are various ways of implementing the Newmark scheme, one which is used in the present work is called the $a-$form [10]. Define *predictors*,

$$\begin{aligned} \tilde{\mathbf{U}}_{\mathbf{n+1}} &= \mathbf{U_n} + \Delta t \mathbf{v_n} + \frac{\Delta t^2}{2}(1 - 2\beta)\mathbf{a_n} \\ \tilde{\mathbf{v}}_{\mathbf{n+1}} &= \mathbf{v_n} + (1 - \gamma)\Delta t \mathbf{a_n}. \end{aligned} \tag{3.34}$$

The next step is to use the *predictors* to obtain the actual quantities,

$$\begin{aligned} \mathbf{U_{n+1}} &= \tilde{\mathbf{U}}_{\mathbf{n+1}} + \beta \Delta t^2 \mathbf{a_n} \\ \mathbf{v_{n+1}} &= \tilde{\mathbf{v}}_{\mathbf{n+1}} + \gamma \Delta t \mathbf{a_{n+1}}. \end{aligned} \tag{3.35}$$

Here β and γ are algorithmic parameters that are fine tuned for integration accuracy and numerical stability. For a discussion on the effect of these parameters on the performance on the algorithm, see [10].

To start the process, $\mathbf{a_0}$ can be calculated from

$$\mathbf{M\ddot{a}}(0) = -\mathbf{K}\mathbf{U}(0) + \mathbf{F}^{elec}(B(0), \mathbf{U}(\mathbf{0})) + \mathbf{F}^{flu}(\mathbf{H}^{flu}(0)). \tag{3.36}$$

To march forward in time for acceleration, one needs to solve the time discrete version of the dynamic Eq. (3.32),

$$\mathbf{M}\mathbf{a}_{n+1} + \mathbf{K}\mathbf{U}_{n+1} = \mathbf{F}^{elec}(B_{n+1}, \mathbf{U}_{n+1}) + \mathbf{F}^{flu}(\mathbf{H}^{flu}_{n+1}). \tag{3.37}$$

This equation set is nonlinear and is solved using the Newton scheme.

3.4.2 Implicit Time Integration

Finally, time integration for the problem is implemented using the Newmark scheme utilizing Newton's scheme. The method follows closely from Belytchko et.al. [35].

Write Eq. (3.32) as:

$$\mathbf{M\ddot{U}}(t) + \mathbf{K}\mathbf{U}(t) = \mathbf{f}(B(t), \mathbf{H}^{flu}(t)). \tag{3.38}$$

Here $\mathbf{f}(B(t), \mathbf{H}^{flu}(t))$ denotes the entire force loading term obtained through BEM analysis. One can define:

$$\mathbf{R}(\mathbf{U}, B, \mathbf{H}^{flu}) = \begin{pmatrix} R_E \\ R_M \\ R_F \end{pmatrix} \tag{3.39}$$

Here, $\mathbf{R}$ is the grand residual for the problem. The Newton iterative scheme is essentially:

$$\begin{pmatrix} R_{EB} & R_{EM} & R_{EF} \\ R_{ME} & R_{MM} & R_{MF} \\ R_{FE} & R_{FM} & R_{FF} \end{pmatrix}^{(k)} \cdot \begin{pmatrix} \Delta B \\ \Delta \mathbf{U} \\ \Delta \mathbf{H}^{flu} \end{pmatrix}^{(k)} = - \begin{pmatrix} R_E \\ R_M \\ R_F \end{pmatrix}^{(k)} \tag{3.40}$$

$$\mathbf{U}^{(k+1)} = \mathbf{U}^{(k)} + \Delta \mathbf{U}^{(k)} \quad B^{(k+1)} = B^{(k)} + \Delta B^{(k)} \quad \mathbf{H}^{flu(k+1)} = \mathbf{H}^{flu(k)} + \Delta \mathbf{H}^{flu(k)}. \tag{3.41}$$

Superscripts denote a Newton iteration step and subscripts a Newmark integrator step. Starting with $k = 0$, Eq. (3.40) is iterated until convergence. At convergence, $\mathbf{R}^{(k)} \equiv R(\mathbf{U^{(k)}}, B^{(k)}, \mathbf{V^{(k)}}) \rightarrow \mathbf{0}$. This iteration helps one to find the value of $\mathbf{a_n}$ needed at each step of time integration through an update of $\mathbf{U_n^{(k)}}$. The algorithm for the coupled scheme is described below:

1. Solve BEM on ∂B for applied voltage and compute the traction $\mathbf{H_0}$ from [17].
2. Set initial values of displacement $\mathbf{U_0}$ and velocity $\mathbf{v_0}$ to $\mathbf{0}$ and compute initial acceleration using $\mathbf{a_0} = \mathbf{M^{-1}H_0}$
3. Set $\mathbf{a}_{n+1}^{(0)} = \mathbf{a}_n, \mathbf{v}_{n+1}^{(0)} = \mathbf{v}_n$ and $\mathbf{U}_{n+1}^{(0)} = \mathbf{U}_n$.
4. Estimate $\tilde{\mathbf{U}}_{n+1}$ and $\tilde{\mathbf{v}}_{n+1}$ from $\mathbf{U}_n$ and $\mathbf{v}_n$using Eq. (3.34).
5. $B_{n+1}^{(0)} = B_n$ and $\mathbf{H}_{n+1}^{flu(0)} = \mathbf{H}_n^{flu}$
6. Set $k = 1$
7. Newton iteration for time step $n + 1$:

(a) Use Eq. (3.19, 3.21 and 3.25) to compute the value of requisite residuals.$B = B_{n+1}^{(k)}, \mathbf{U} = \mathbf{U}_{n+1}^{(k)}, \mathbf{H}^{flu} = \mathbf{H}_{n+1}^{flu(k)}$.

(b) Use [17] and Eq. (3.20) to get residual gradient for the electrical part, where $B = B_{n+1}^{(k)}, \mathbf{U} = \mathbf{U}_{n+1}^{(k)}, \mathbf{H}^{flu} = \mathbf{H}_{n+1}^{flu(k)}$.

(c) Similarly proceed to compute the other six gradients from the relevant equations

(d) Update acceleration as $\mathbf{a}_{n+1}^{(k)} = 1/\beta\Delta t^2(\mathbf{U}_{n+1}^{(k)} - \tilde{\mathbf{U}}_{n+1})$ and $\mathbf{v}_{n+1}^{(k)} = \tilde{\mathbf{v}}_{n+1} + \gamma\Delta t\mathbf{a}_{n+1}^{(k)}$

(e) $R_M^{(k)} = R_M^{(k)} + \mathbf{M}\mathbf{a}_{n+1}^{(k)}$ and $\partial R_M/\partial \mathbf{U}|^{(k)} = \partial R_M/\partial \mathbf{U}|^{(k)} + 1/(\beta\Delta t^2)\mathbf{M}$

(f) Plug the above residuals to Eq. (3.40) and solve for the increments.

(g) Using Eq. (3.40), to compute the increments .

(h) Use Eq. (3.41) to update the primary variables.

(i) Compute the tolerance, TOL $= \frac{||\mathbf{U}_{n+1}^{(k)} - \mathbf{U}_{n+1}^{(k-1)}||}{||\mathbf{U}_{n+1}^{(k-1)}||} \times 100\%$

(j) Update $k = k + 1$

(k) If tolerance is high, repeat from step (7).

8. $\mathbf{a}_{n+1} = \mathbf{a}_{n+1}^{(k)}, \mathbf{v}_{n+1} = \mathbf{v}_{n+1}^{(k)}, \mathbf{U}_{n+1} = \mathbf{U}_{n+1}^{(k)}$

9. $B_{n+1} = B_{n+1}^{(k)}, \mathbf{H}_{n+1}^{flu} = \mathbf{H}_{n+1}^{flu(k)}$

10. $n = n + 1$ and repeat from step (3) till required time limit is reached.

3.5 Numerical Verification

3.5.1 Code Verification

The computer code with thin beam Lagrangian Stokes BEM has been carefully verified at several stages. The beam dimensions have been taken to be $1000\mu m \times 40\mu m \times 0.5\mu m$ and dynamic viscosity is assumed to be $1 \times 10^{-5} Pa \cdot s$ for the numerical results. The incompressible Stokes' equations are employed in sections 3.5.1 and 3.5.1.

Plane Couette Flow

Couette flow refers to flow between two parallel plates, one of which is moving with respect to the other. The analytical solution for this kind of flow is known. If the bottom plate is fixed and the top plate is moving with speed v_0 , is at a distance D from the latter and the fluid has dynamic viscosity μ , then the horizontal traction τ on the top surface can be written as:

$$\tau = \mu \frac{v_0}{D}. \tag{3.42}$$

It must be noted that the value of the traction at the bottom surface would be equal and opposite to the above.

For numerical verification the gap D between the plates has been taken to be $10\mu m$ and velocity of the top plate $1m/s$. The analytical value of the horizontal traction in this case would be (from Eq. (3.42)) $1Pa$. The numerical results have been shown in Fig .3.3 and agree to within 3% of the analytical result.

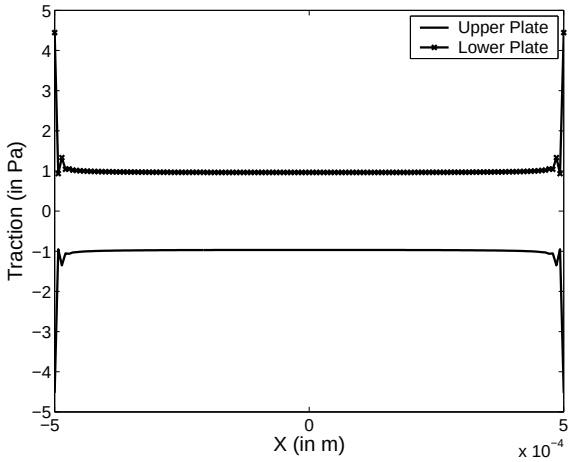

Figure 3.3: Horizontal traction on plates for plane Couette flow

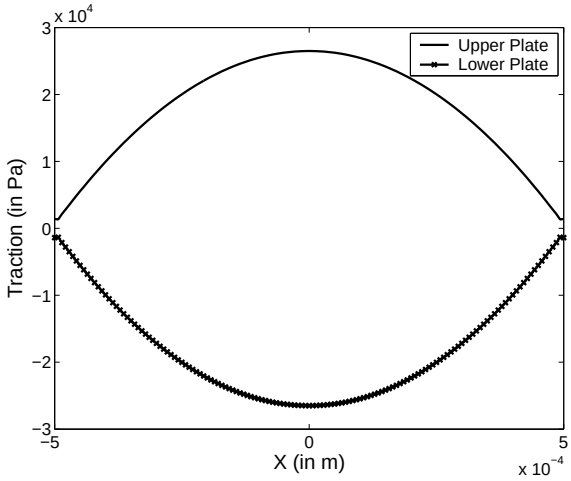

Figure 3.4: Vertical traction on plates moving vertically towards each other

Vertically Moving Plate

When the plates are moving vertically towards each other, to the best of the author's knowledge, there is no closed form solution. However, certain inferences can be drawn for this kind of flow.

For numerical verification, the initial gap D between the plates have been

taken to be $10\mu m$ and the velocity of the top plate $1\ m/s$ downwards and that of bottom plate is $1\ m/s$ upwards. Fig. 3.4 shows the vertical traction generated by such motion. It can be deduced from the physics that the vertical traction would be equal and opposite on the two plates and will have maximum value at the center and decrease towards the sides as fluid escapes. This trend can be clearly observed in the plot. Fig. 3.5 shows a plot of the horizontal traction for this motion. One can deduce that as the plates move towards each other, they displace fluid from the central part of the plates to the periphery in opposite directions. Hence the horizontal traction should be antisymmetric with respect to the centerline on either side of the top plate. The exact same effect would be visible for the bottom plate via symmetry of the problem. This effect is clearly observed in the plot of horizontal traction.

Compressibility and Convergence

When the initial gap between the plates is reduced to $\mathcal{O}(0.005L)$ unrealistically large stresses result and convergence takes disproportionately larger time. The effect of incompressibility on convergence can be clearly seen in the plot Fig. 3.6 presented here for such small gaps. The computing requirement increases very sharply as one approaches the incompressibility limit of $\nu \to \frac{1}{2}$.

It is noted however, that the value of ν for air and water are approximately 0.499999999999 and 0.49999999999999 respectively at room temperature. Hence, $\nu = \frac{1}{2}$ should be used for practical calculations involving these fluids.

3.5.2 Thin Beam Dynamics

Material Properties

Material properties used for Silicon conductors are [36], [37]:

$$E = 169GPa, \quad \nu^s = 0.22, \quad \rho = 2231Kg/m^3, \tag{3.43}$$

whereas properties of the surrounding medium are:

$$\epsilon = 8.85 \times 10^{-12}F/m, \quad \mu = 1.0 \times 10^{-5}Pa \cdot s, \quad \nu^f = 0.50 \quad \text{(except for Fig. 3.8).} \tag{3.44}$$

Here, E, ν^s and ρ refer to the Young's modulus, Poisson's ratio and density of Silicon respectively whereas ϵ, μ and ν^f are the permittivity of free space, dynamic viscosity and Poisson parameter of air respectively. It is assumed that the anisotropy is negligible and the beam is made up of poly-silicon for this system.

The Problem

Dynamics of a MEMS beam (the silicon is doped so that it is a conductor), subjected to both DC and AC bias (electric field) inside a fluid medium is simulated using a BEM-FEM coupled approach described earlier in this chapter. Each beam is clamped-clamped configuration and two beams are used in order to have a zero voltage and velocity at the ground plane (plane of symmetry) midway between them (see Fig. 3.1). The MEMS beam is $1000\mu m$ long, $40\mu m$ wide and $0.5\mu m$ in height. The initial gap (gap_0) is $5\mu m$. The transverse mid point

deflection is denoted by w_{mid}.

Results

The dynamic behavior of the beam under DC bias of $0.5V$ can be seen in Fig. 3.7. The time period in the plot refers to $T_p = 2\pi/\Omega_{Nat}$ where $\Omega_{Nat} = (4.73)^2(EI/\rho SL^4)^{1/2}$ from the classical linear beam theory [38]. For the current beam geometry, $T_p \approx 226.75\mu s$.

It should be noted that incompressible Stokes flow in the current configuration causes overdamped motion as shown in Fig. 3.7. The equilibrium position of the beam in Fig. 3.7 agrees to within 1% of the quasi-static value obtained in [17].

The effect of compressibility of the fluid medium is indicated in Fig. 3.8. It is clear that damping resistance offered by the fluid greatly increases as the Poisson parameter $\nu \rightarrow \frac{1}{2}$ (incompressible limit).

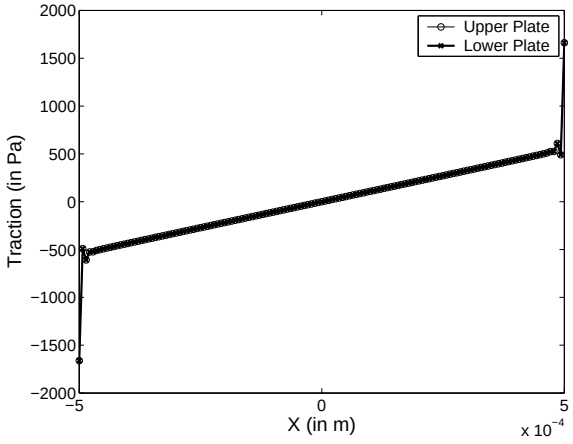

Figure 3.5: Horizontal traction on plates moving vertically towards each other

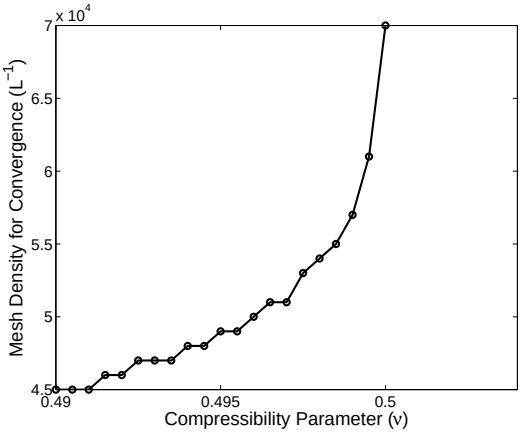

Figure 3.6: Compressibility influence on convergence

Fig. 3.9 shows the response of the beam under AC bias of $0.5\cos(0.5\Omega_{Nat}t)$. As the forcing is proportional to the square of the voltage, the response frequency is twice the applied frequency.

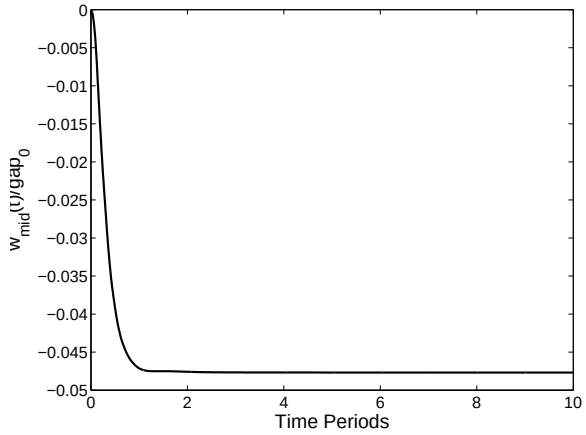

Figure 3.7: Damped response for DC bias of 0.5V

Fig. 3.10 shows the response of the beam under a combined AC and DC bias. The DC component of the bias is $0.5V$ and the AC component is $0.05\cos(0.5\Omega_{Nat}t)$. The beam vibrates about the quasi-static value corresponding approximately to the DC bias and with a frequency almost equal to $0.5\Omega_{Nat}$.

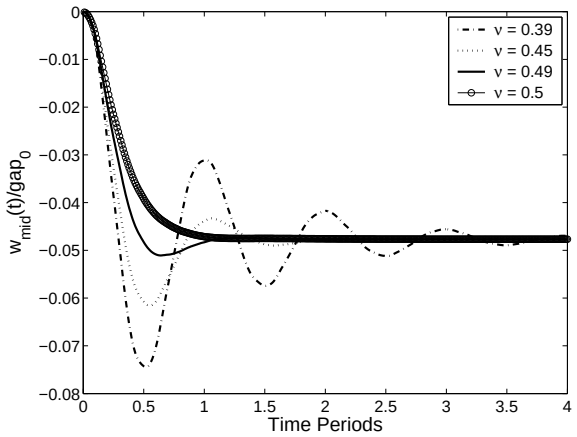

Figure 3.8: Damped vibrations for various Poisson parameters (DC bias = $0.5V$)

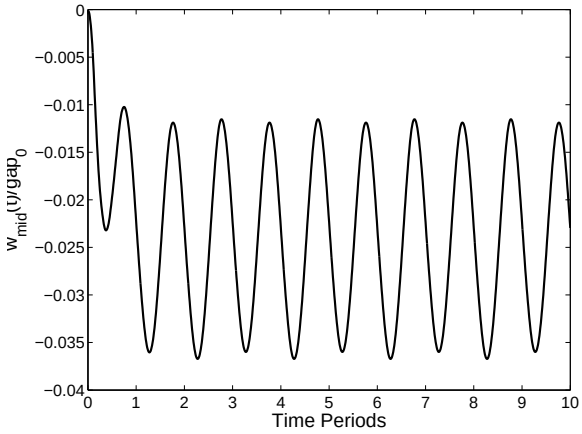

Figure 3.9: Damped vibration for AC $0.5\cos(0.5\Omega_{Nat}t)V$

This is expected since,

$$\begin{aligned} F_{elec}(t) \propto V_{app}^2 &= (0.5 + 0.05\cos(0.5\Omega_{Nat}t))^2 \\ &= 0.25 + 0.05\cos(0.5\Omega_{Nat}t) + 0.0025\cos^2(0.5\Omega_{Nat}t) \\ &= 0.2513 + 0.05\cos(0.5\Omega_{Nat}t) + 0.0013\cos(\Omega_{Nat}t) \end{aligned} \quad (3.45)$$

From Eq. (3.45), the dominant AC term has frequency $0.5\Omega_{Nat}$ and the oscillations occur about the quasi-static response of $0.2513V \approx 0.25V$ (see Fig. 3.7 and

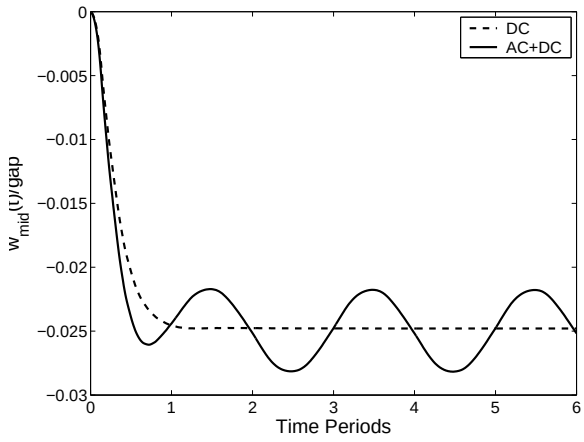

Figure 3.10: Damped vibration for AC+DC bias of $0.5+0.05\cos(0.5\Omega_{Nat}t)V$

3.10)

3.6 Conclusions

Damped free and forced vibrations of thin MEMS beams surrounded by a fluid medium caused by applied DC and AC excitation have been studied in this work. The BEM (a special version suitable for thin features) is used to model the exterior electric field as well as the fluid fields assuming Stokes flow. A fully Lagrangian version of the fluid flow equations are employed and integrated with the Lagrangian versions of the electrical and mechanical equations developed in the companion paper [17]. The fluidic domain is coupled with the mechanical domain through continuity of velocity and equilibrium of traction and the entire Lagrangian coupled problem is solved using a Newton scheme with time integration carried out by the Newmark method. The derivatives of the residuals necessary for the Newton method (which now incorporate the fluid variables as well) are carefully obtained by analytic differentiation of the relevant integral

and FEM equations.

An a posteriori check confirms that the typical Reynold's number for the examples given in this chapter is $\mathcal{O}(10^{-3})$. This justifies the Stokes flow model employed here.

The code developed to simulate the coupled electro-mechanical-fluidic problem is carefully verified by comparison with other solutions reported in the literature. Numerical results for the beam vibrations both free (under DC bias) and forced by AC excitation are presented here for selected problems. The approach presented in this chapter can be extended to study vibrations of MEMS with plates or NEMS with nanowires and nanotubes in a straightforward manner.

It is noted that the method developed here can be extended to handle more detailed numerical calculations needed for complex configurations like variable thickness beams and plates with holes etc. as compared to analytical or semi-analytical methods which are usually restricted to problems with simple geometry (A static deformation analysis of plates without a surrounding fluid has been presented in [39]).

A genuine numerical difficulty is encountered (requiring very small time steps and tighter tolerances for the Newton iteration) when the surrounding fluid is incompressible Stokes and the initial gap between the two beams is very small. A similar observation has also been made in [23]. Unfortunately, the common fluids such as air and water are very nearly incompressible with $\nu^f \approx 0.5$. It has been also found that the most important residual gradients needed for successful Newton's iteration are the ones with respect to their own domain variables, i.e. R_{EE}, R_{MM} and R_{FF}.

Acknowledgments

This research has been supported by National Science Foundation Grant $\#CMS - 0508466$ to Cornell University.

BIBLIOGRAPHY

[1] Roman M. and Aubry N. Design and fabrication of electrostatically actuated synthetic microjets. *ASME Paper No. IMECE2003-41579, New York, American Society of Mechanical Engineers*, 259:517–524, 2003.

[2] Ko S. C., Kim Y. C., Lee S. S., Choi S. S., and Kim S. R. Micromachined piezoelectric membrane acoustic device. *Sensors and Actuators A*, 103:130–134, 2003.

[3] Mukherjee S. *Boundary Element Methods in Creep and Fracture*. Applied Science Publishers, London, 1982.

[4] Banerjee P. K. *Boundary Element Methods in Engineering*. McGraw Hill, Europe, 1994.

[5] Chandra A. and Mukherjee S. *Boundary Element Methods in Manufacturing*. Oxford University Press, New York, 1997.

[6] Bonnet A. *Boundary Element Equation Methods for Solids and Fluids*. Wiley, Chichester, UK, 1999.

[7] Mukherjee S. and Mukherjee Y. X. *Boundary Methods: Elements, Contours and Nodes*. Taylor and Francis, CRC Press, Boca Raton, FL, 2005.

[8] Yang T. Y. *Finite Element Structural Analysis*. Prentice-Hall, Englewood Cliffs, New York, 1986.

[9] Zienkiewicz O. C. and Taylor R. L. *The Finite Element Method*, volume 1,2, 4th Ed. McGraw Hill, Berkshire, UK, 2005.

[10] Hughes T. J. R. *The Finite Element Method: Linear Static and Dynamic Finite Element Analysis*. Dover, Mineola, NY., 2000.

[11] Senturia S. D., Harris R. M., Johnson B. P., Kim S., Nabors K., Shulman M. A., and White J. K. A computer aided design system for microelectromechanical systems(memcad). *IEEE J. Microelectromech. Syst.*, 1:3–13, 1992.

[12] Nabors K. and White J. Fastcap: a multi-pole accelarated 3-d capcacitance extraction program. *IEEE Transcations in Computer Aided Design*, 10:1447–1459, 1991.

[13] Gilbert J. R., Legtenberg R., and Senturia S. D. 3d coupled electromechanics for mems: applications of cosolve-em. In *Proceedings, IEEE MEMS*, 1995.

[14] Shi F., Ramesh P., and Mukherjee S. Simulation methods for micro-electromechanical structures (mems) with applications to microtweezer. *Comp. Struct.*, 56:769–783, 1995.

[15] Aluru N. R. and White J. An efficient numerical technique for electromechanical simulation of complicated microelectromechancial structures. *Sens. Actuators A*, 58:1–11, 1997.

[16] Shi F., Ramesh P., and Mukherjee S. Dynamic analysis of micro-electromechanical systems. *Int. J. Num. Meth. Engng.*, 39:4119–4139, 1996.

[17] Ghosh R. and Mukherjee S. Fully lagrangian modeling of dynamics of mems with thin beams – Part I: Undamped vibrations. *ASME J. Appl. Mech., submitted*, 2008.

[18] Ye W., Wang X., Hemmert W., Freeman D., and White J. Air damping forces in laterally oscillatory microresonators:a numerical and experimental study. *IEEE J. Microelectromech. Syst.*, 12:557–566, 2003.

[19] Mukherjee S., Telukunta S., and Mukherjee Y. X. Bem modeling of damping forces on mems with thin plates. *Eng. Anal. Bound. Elem.*, 29:1000–1007, 2005.

[20] Li G. and Aluru N. R. Efficient mixed-domain analysis of electrostatic mems. *IEEE Trans. Comput.-Aided Design*, 22:1228–1242, 2003.

[21] De S. K. and Aluru N. R. Full-lagrangian schemes for dynamic analysis of electrostatic mems. *IEEE J. Microelectromech. Syst.*, 13, 2004.

[22] Pan F., Kubby J., Peeters E., Tran A. T., and Mukherjee S. Squeeze film damping effect on the dynamic response of a mems torsion mirror. *J. Micromech. Microeng.*, 8:200–208, 1998.

[23] Frangi A. and di Gioa A. Multipole bem for evaluating damping forces on mems. *Comput. Mech.*, 37(1):24–31, December 2005.

[24] Ding J. and Ye W. A fast integral approach for drag force calculation due to oscillatory slip stokes flows. *Int. J. Num. Meth. Engng.*, 60:1535–1567, 2004.

[25] Hutcherson S. and Ye W. On the squeeze film damping of micro-resonators in the free-molecule regime. *J. Micromech. Microeng.*, 14(1726-1733), 2004.

[26] Bhiladvala R. B. and Wang Z. J. Effect of fluids on the q factor and resonance frequency of oscillating micrometer and nanometer scale beams. *Phys. Rev. E*, 69:036307, 2004.

[27] Bao Z., Mukherjee S., Roman M., and Aubry N. Nonlinear vibrations of beams, strings, plates and membranes without initial tension. *ASME J. App. Mech.*, 71(4):551–559, 2003.

[28] Pozrikidis C. *Boundary Integral and Singularity Methods for Linearized Viscous Flow*. Cambridge University Press, Cambridge, UK, 1992.

[29] Mukherjee S. CPV and HFP integrals and their applications in the boundary element method. *Int. J. Solids. Structures*, 45:6623–6634, 2000.

[30] Mukherjee S. Finite parts of singular and hypersingular integrals with irregular boundary source points. *Eng. Anal. Bound. Elem.*, 24:767–776, 2004.

[31] Bao Z. and Mukherjee S. Electrostatic bem for mems with thin conducting plates and shells. *Eng. Anal. Bound. Elem.*, 28:1427–1435, 2004.

[32] Liao Y. S., Chyuan S. W., and Chen J. T. Efficaciously modeling exterior electrostatic problems with singularity for electron devices. *IEEE Circuits Devices Mag*, pages 25–34, 2004.

[33] Cunha F. C., De Sousa A. J., and Loewenberg M. A mathematical formulation of the boundary integral equations for the compressible stokes flow. *Mat. apl. comput.*, 22(1):53–73, 2003.

[34] Newmark N. M. A method of computation for structural dynamics. *J. Engg. Mech. Div., ASCE*, pages 67–94, 1959.

[35] Belytschko T., Lui W. K., and Moran B. *Nonlinear Finite Element for Continua and Structures*. John Wiley & Sons, Ltd., 2000.

[36] Petersen K. E. Silicon as a mechanical material. In *Proceedings, IEEE*, volume 70, pages 420–455, 1982.

[37] Sharpe W. N. Jr. *Mechanical Properties of MEMS materials in The MEMS handbook*. CRC, Boca Raton, FL, 2001.

[38] Hurty W. C. and Rubinstein M. F. *Dynamics of Structures*. Prentice Hall, Englewood Cliffs, New Jersey, 1964.

[39] Telukunta S. and Mukherjee S. Fully lagrangian modeling of mems with thin plates. *IEEE J. Microelectromech. Syst.*, 15(4):795–810, 2006.

CHAPTER 4

APPLICATION OF SINGULAR ELEMENTS FOR FULLY LAGRANGIAN MODELING OF DYNAMICS OF MEMS WITH THIN BEAMS

The field of micro-electro-mechanical systems (MEMS) is a very broad one that includes fixed or moving microstructures; encompassing micro-electro-mechanical, microfluidic, micro-electro- fluidic-mechanical, micro-opto-electro-mechanical and micro-thermo-mechanical devices and systems. MEMS usually consists of released microstructures that are suspended and anchored, or captured by a hub-cap structure and set into motion by mechanical, electrical, thermal, acoustical or photonic energy source(s).

Typical MEMS structures consist of arrays of thin plates with cross-sections in the order of microns (μm) and lengths in the order of ten to hundreds of microns (See, for example, Fig. 4.1). Sometimes, MEMS structural elements are beams. An example is a small rectangular silicon beam with length in the order of mm and thickness of the order of microns, that deforms when subjected to electric fields. Owing to its small size, significant forces and/or deformations can be obtained with the application of low voltages ($\approx$ 10 volts).

Numerical simulation of electrically actuated MEMS devices have been carried out for nearly two decades using the Boundary Element Method (BEM - see, e.g. [2],[3], [4],[5] and [6]) to model the exterior electric field and the Finite Element Method (FEM - see, e.g. [7], [8] and [9]) to model deformation of the structure. Examples of this research can be found in Refs. [10], [11], [12], [13],[14] and [15]. Li and Aluru [16] first proposed a Lagrangian approach for the electri-

[0]R. Ghosh and S. Mukherjee, Singular boundary element application to MEMS with thin beams, Engineering Analysis with Boundary Elements, Volume 34, May 2010, pp-447-455

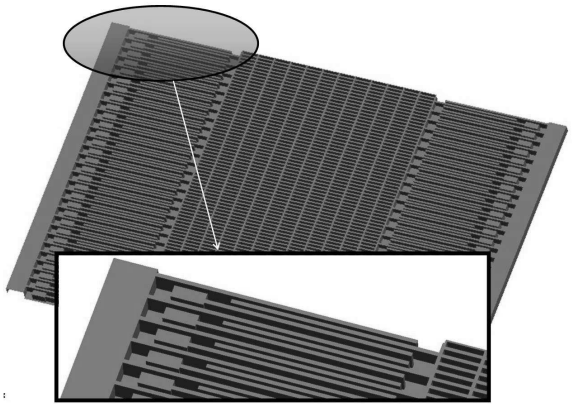

Figure 4.1: Parallel plate resonator: geometry and detail of the parallel plate fingers from [1]

cal analysis as well, thus obviating the need to carry out calculations based on the deformed shapes of a structure. Two- and three-dimensional (2-D and 3-D) quasi-static Lagrangian exterior BEM analysis was addressed in [17] and [18]; while a fully coupled 2-D quasi-static MEMS analysis has been carried out in [16].

Ghosh and Mukherjee ([19], [20]) have recently carried out simulations of fully Lagrangian dynamics for thin clamped-clamped micro-beams. Cantilevered micro-beams, however, cause singularities in the BEM due to the free edge [21]. In order to overcome this singularity, various methods have been proposed [21],[22] and [23]. The superiority of the singular element approach over the adaptive mesh refinement approach in terms of accuracy lies in the fact that the physical nature of the singularity is taken into account in the singularity approach during the solution process. In the area of MEMS, Ong et al. [22] have applied singular elements for the study of quasi-static electromechanics of regular MEMS. In the present work, a singular element formulation is presented for dynamic simulation of thin-MEMS.

This chapter first presents the relevant BIE equations in the electrical domain. Details of the singular element formulation are given next, followed by the FEM equations in the mechanical domain. Next comes a description of Newton's scheme for solving the coupled problem, followed by a discussion of dynamic analysis of MEMS. Numerical results and concluding remarks complete the chapter.

4.1 Electrical Problem in the Exterior Domain

Fig. 4.2 shows (as an example of a MEMS device) a deformable, clamped beam over a fixed ground plane. The undeformed configuration is B with boundary ∂B. The beam deforms when a potential V is applied between the two conductors, and the deformed configuration is called b with boundary ∂b. The charge redistributes on the surface of the deformed beam, thereby changing the electrical force on it and this causes the beam to deform further. The system then undergoes vibrations and the complete analysis of the system is done using the Newton scheme.

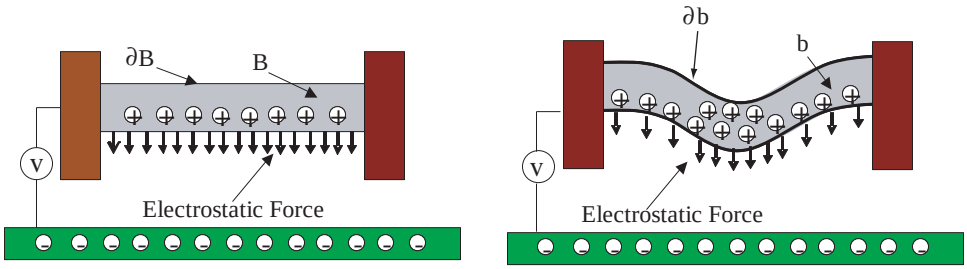

Figure 4.2: Deformable clamped beam over a fixed ground plate

4.1.1 Electric Field BIE in a Simply-Connected Body

The boundary element formulation of the electric problem can be derived from the Laplace equation which governs the potential in the region outside a conductor.

4.1.2 BIEs in Infinite Region Containing Two Thin Conducting Beams

Consider the situation shown in Fig. 4.3. Of interest is the solution of the following Dirichlet problem for Laplaces equation:

$$\nabla^2\phi(\mathbf{x}) = 0, \quad \mathbf{x} \in B, \quad \phi(\mathbf{x}) \text{ prescribed for } \mathbf{x} \in \partial\mathbf{B} \tag{4.1}$$

where B is the region *exterior* to the two beams. The unit normal $\mathbf{n}$ to B is defined to point away from B (i.e., into the beam).

Regular BIE - Source Point Approaching a Beam Surface s_1^+

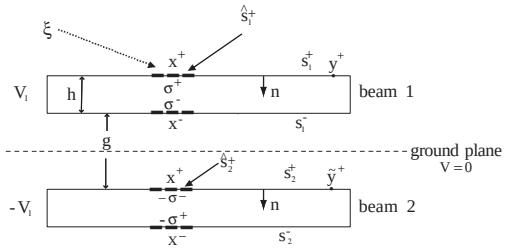

Figure 4.3: Two parallel conducting beams

It has been shown by Bao & Mukherjee [24] that for this case:

$$\phi(\mathbf{x}^+) = -\int_{s_1^+ - \hat{s}_1^+} \frac{\ln r(\mathbf{x}^+, \mathbf{y})\beta(\mathbf{y})}{2\pi\epsilon} ds(\mathbf{y}) - \int_{\hat{s}_1^+} \frac{\ln r(\mathbf{x}^+, \mathbf{y})\beta(\mathbf{y})}{2\pi\epsilon} ds(\mathbf{y}) - \int_{s_2^+} \frac{\ln r(\mathbf{x}^+, \mathbf{y})\beta(\mathbf{y})}{2\pi\epsilon} ds(\mathbf{y}). \quad (4.2)$$

Here $\beta(\mathbf{y}) = \sigma(\mathbf{y}^+) + \sigma(\mathbf{y}^-)$, where σ is now the charge density at a point on the beam surface. The second integral in Eq. (4.2) is logarithmically singular and the rest are regular except when the beam thickness and the gap become very small.

A similar equation can be written for $\mathbf{x}^+ \in s_2^+$. For the case shown in Fig. 4.3, however, that is not necessary since $\beta(\mathbf{y})$ is equal and opposite on the two beams. Therefore, for this case, Eq. (4.2) is sufficient to solve for β on both the beams.

Hypersingular BIE - Source Point Approaching a Beam Surface s_1^+

It is first noted that for $\mathbf{x}^+ \in s_k^+ \cup s_k^-,\ k = 1, 2:$

$$\sigma(\mathbf{x}) = \epsilon \frac{\partial \phi}{\partial n}(\mathbf{x}) = \epsilon \mathbf{n}(\mathbf{x}) \cdot [\nabla_\xi \phi(\xi)]_{\xi = x}. \quad (4.3)$$

Consider the limit $\xi \to \mathbf{x}^+ \in \hat{s}_1^+ \in s_1^+$. It is important to realize that this limit is meaningless for a point $\mathbf{x}$ on the edge of a beam, since the charge density is singular on its edges. One obtains the following HBIE:

$$\sigma(\mathbf{x}^+) = \int_{s_1^+ - \hat{s}_1^+} \frac{\beta(\mathbf{y})\mathbf{r}(\mathbf{x}^+, \mathbf{y}) \cdot \mathbf{n}(\mathbf{x}^+)}{2\pi r^2(\mathbf{x}^+, \mathbf{y})} ds(\mathbf{y}) + \int_{\hat{s}_1^+} \frac{\mathbf{r}(\mathbf{x}^+, \mathbf{y})[\beta(\mathbf{y}) \cdot \mathbf{n}(\mathbf{x}^+) - \beta(\mathbf{x}^+) \cdot \mathbf{n}(\mathbf{y})]}{2\pi r^2(\mathbf{x}^+, \mathbf{y})} ds(\mathbf{y}) + \frac{\beta(\mathbf{x})}{2\pi} \Psi(\hat{s}_1^+, \mathbf{X}^+) + \int_{s_2^+} \frac{\beta(\mathbf{y})\mathbf{r}(\mathbf{x}^+, \mathbf{y}) \cdot \mathbf{n}(\mathbf{x}^+)}{2\pi r^2(\mathbf{x}^+, \mathbf{y})} ds(\mathbf{y}). \quad (4.4)$$

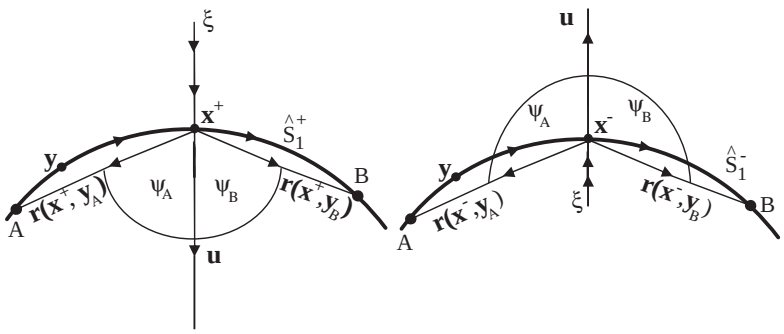

Figure 4.4: Evaluations of angles

In the above, the angle subtended by the line element s_1^+ at the point $\mathbf{x}^+$ (see [25],[24]) and Fig. 4.4 is:

$$\Psi(\hat{s}_1^+, \mathbf{x}^+) = \oint\!\!\!\!\!\!= \int_{\hat{s}_1^+} \frac{\mathbf{r}(\mathbf{x}^+, \mathbf{y}) \cdot \mathbf{n}(\mathbf{y})}{r^2(\mathbf{x}^+, \mathbf{y})} ds(\mathbf{y}) = \psi_A + \psi_B. \tag{4.5}$$

Here, the symbol $\oint\!\!\!\!\!\!=$ denotes the finite part of the integral in the sense of Mukherjee [26]. Also (see Fig. 4.4), a unit vector $\mathbf{u}$, through the point $\mathbf{x}^+$, is chosen such that it intersects $\hat{s}_1^+$. Now, ψ is the angle between the positive $\mathbf{u}$ vector and $\mathbf{r}(\mathbf{x}^+, \mathbf{y})$ with $\mathbf{y} \in \hat{s}_1^+$. This angle can be obtained from the equation,

$$\cos(\psi(\mathbf{y})) = \frac{\mathbf{r}(\mathbf{x}^+, \mathbf{y}) \cdot \mathbf{u}}{r(\mathbf{x}^+, \mathbf{y})} \tag{4.6}$$

From Eq. (4.4) and Eq. (4.6) one gets the following equation,

$$\begin{aligned} \frac{1}{2}[\sigma(\mathbf{x}^+) - \sigma(\mathbf{x}^-)] &= \int_{s_1^+ - \hat{s}_1^+} \frac{\beta(\mathbf{y}) \mathbf{r}(\mathbf{x}^+, \mathbf{y}) \cdot \mathbf{n}(\mathbf{x}^+)}{2\pi r^2(\mathbf{x}^+, \mathbf{y})} ds(\mathbf{y}) \\ &+ \int_{\hat{s}_1^+} \frac{\mathbf{r}(\mathbf{x}^+, \mathbf{y})[\beta(\mathbf{y}) \cdot \mathbf{n}(\mathbf{x}^+) - \beta(\mathbf{x}) \cdot \mathbf{n}(\mathbf{y})]}{2\pi r^2(\mathbf{x}^+, \mathbf{y})} ds(\mathbf{y}) \\ -\frac{\beta(\mathbf{x}^+)}{2\pi}[\pi - \Psi(\hat{s}_1^+, \mathbf{x}^+)] &+ \int_{s_2^+} \frac{\beta(\mathbf{y}) \mathbf{r}(\mathbf{x}^+, \mathbf{y}) \cdot \mathbf{n}(\mathbf{x}^+)}{2\pi r^2(\mathbf{x}^+, \mathbf{y})} ds(\mathbf{y}). \end{aligned} \tag{4.7}$$

Eq. (4.2) gives the sum of the charge densities and the HBIE Eq. (4.7) can be used as a post-processing step to compute the values of individual charge densities on each of the beams.

4.1.3 Electrostatic Boundary Integral Equation in the Lagrangian Framework

Converting Eq. (4.2) and Eq. (4.7) in the Lagrangian framework can be started by using Nanson's law [27]:

$$\mathbf{n}ds = J\mathbf{N} \cdot \mathbf{F}^{-1}dS. \tag{4.8}$$

Here $\mathbf{n}$ and $\mathbf{N}$ are unit normal vectors to ∂b and ∂B, at the generic points $\mathbf{x}$ and $\mathbf{X}$, respectively, $\mathbf{F} = \frac{\partial \mathbf{x}}{\partial \mathbf{X}}$ is the deformation gradient, $J = det(\mathbf{F})$ and dS is an area element on ∂B. Also, $\mathbf{X}$ and $\mathbf{x}$ denote coordinates in the undeformed and deformed configurations, respectively. From Eq. (4.8), it follows that:

$$ds = J|\mathbf{N} \cdot \mathbf{F}^{-1}|dS. \tag{4.9}$$

Next, define Σ, the charge density per unit undeformed surface area. Since $\Sigma dS = \sigma ds$, one has:

$$\Sigma = J\sigma|\mathbf{N} \cdot \mathbf{F}^{-1}|. \tag{4.10}$$

Also define:

$$B = \Sigma^{+} + \Sigma^{-} \tag{4.11}$$

Lagrangian Version of the Regular BIE

Using the relations developed in the previous section, one arrives at the Lagrangian version of the Eq. (4.2),

$$\phi(\mathbf{X}^+) = -\int_{S_1^+ - \hat{S}_1^+} \frac{\ln R(\mathbf{X}^+, \mathbf{Y}) B(\mathbf{Y})}{2\pi\epsilon} dS(\mathbf{Y}) - \int_{\hat{S}_1^+} \frac{\ln R(\mathbf{X}^+, \mathbf{Y}) B(\mathbf{Y})}{2\pi\epsilon} dS(\mathbf{Y}) - \int_{S_2^+} \frac{\ln R(\mathbf{X}^+, \mathbf{Y}) B(\mathbf{Y})}{2\pi\epsilon} dS(\mathbf{Y}) \quad (4.12)$$

where:

$$\begin{aligned} \mathbf{r}(\mathbf{x}(\mathbf{X}), \mathbf{y}(\mathbf{Y})) \equiv \mathbf{R}(\mathbf{X}, \mathbf{Y}) &= \mathbf{y}(\mathbf{Y}) - \mathbf{x}(\mathbf{X}) = \mathbf{Y} + \mathbf{u}(\mathbf{Y}) - \mathbf{X} - \mathbf{u}(\mathbf{X}) \\ &= \mathbf{R_0}(\mathbf{X}, \mathbf{Y}) + \mathbf{u}(\mathbf{Y}) - \mathbf{u}(\mathbf{X}) \end{aligned} \quad (4.13)$$

$$\mathbf{R_0}(\mathbf{X}, \mathbf{Y}) = \mathbf{Y} - \mathbf{X} \quad (4.14)$$

$$r(\mathbf{x}(\mathbf{X}), \mathbf{y}(\mathbf{Y})) \equiv R(\mathbf{X}, \mathbf{Y}) = |\mathbf{R}(\mathbf{X}, \mathbf{Y})| \quad (4.15)$$

with $\mathbf{u}$ denoting the displacement at a point in B.

Also:

$$\mathbf{h}(\mathbf{y}) = -\frac{\sigma^2(\mathbf{y})}{2\epsilon}\mathbf{n} \quad (4.16)$$

$$\int_{\partial B} \mathbf{H} dS = \int_{\partial b} \mathbf{h} ds. \quad (4.17)$$

where $\mathbf{h}$ and $\mathbf{H}$ are the tractions per unit deformed and undeformed surface areas, respectively. Using Eq. (4.8), Eq. (4.9), Eq. (4.16) and Eq. (4.17), one gets:

$$\mathbf{H} = -\frac{J\sigma^2 \mathbf{N}\cdot\mathbf{F^{-1}}}{2\epsilon} = -\frac{\Sigma^2}{2J\epsilon}\frac{\mathbf{N}\cdot\mathbf{F^{-1}}}{|\mathbf{N}\cdot\mathbf{F^{-1}}|} \tag{4.18}$$

Lagrangian Version of the Gradient BIE

The Lagrangian version of the Eq. (4.7) is derived as follows,

$$First\,Term = \int_{S_1^+ - \hat{S}_1^+} \frac{B(\mathbf{Y})\mathbf{R}(\mathbf{X}^+,\mathbf{Y})\cdot\Big(\frac{\mathbf{N}\cdot\mathbf{F^{-1}}}{|\mathbf{N}\cdot\mathbf{F^{-1}}|}\Big)(\mathbf{X}^+)}{2\pi R^2(\mathbf{X}^+,\mathbf{Y})} dS(\mathbf{Y}) \tag{4.19}$$

$$\begin{aligned} Second\,Term = \int_{\hat{S}_1^+} \frac{\mathbf{R}(\mathbf{X}^+,\mathbf{Y})B(\mathbf{Y})}{2\pi R^2(\mathbf{X}^+,\mathbf{Y})}\cdot\Big(\frac{\mathbf{N}\cdot\mathbf{F^{-1}}}{|\mathbf{N}\cdot\mathbf{F^{-1}}|}\Big)(\mathbf{X}^+)dS(\mathbf{Y}) \\ -\int_{\hat{S}_1^+} \frac{\mathbf{R}(\mathbf{X}^+,\mathbf{Y})}{2\pi R^2(\mathbf{X}^+,\mathbf{Y})}\cdot\frac{B(\mathbf{X})}{J(\mathbf{X}^+)|\mathbf{N}\cdot\mathbf{F^{-1}}(\mathbf{X}^+)|}\cdot J(\mathbf{Y})(\mathbf{N}\cdot\mathbf{F^{-1}})(\mathbf{Y})dS(\mathbf{Y}) \end{aligned} \tag{4.20}$$

$$Third\,Term = -\frac{B(\mathbf{X})}{2\pi J|\mathbf{N}\cdot\mathbf{F^{-1}}|(\mathbf{X}^+)}[\pi - \Psi(\hat{S}_1^+,\mathbf{X}^+)] \tag{4.21}$$

The fourth term can be treated in the same way as the first. Now, multiply the entire equation by $J(\mathbf{X}^+)|\mathbf{N}\cdot\mathbf{F^{-1}}|(\mathbf{X}^+)$, use the mid-plane values[1] for $\mathbf{F}(\mathbf{X}^+) = \mathbf{F}(\mathbf{X}^-)$ and use the fact that $\mathbf{N}(\mathbf{X}^+) = -\mathbf{N}(\mathbf{X}^-)$ to simplify the equation further. The resulting equation has the form:

[1] Also called the membrane assumption.

$$\frac{1}{2}[\Sigma(\mathbf{X}^+) - \Sigma(\mathbf{X}^-)] = \int_{S_1^+ - \hat{S}_1^+} \frac{B(\mathbf{Y})\mathbf{R}(\mathbf{X}^+, \mathbf{Y}) \cdot J(\mathbf{X}^+)\mathbf{N} \cdot \mathbf{F^{-1}}(\mathbf{X}^+)}{2\pi R^2(\mathbf{X}^+, \mathbf{Y})} dS(\mathbf{Y})$$
$$+ \int_{\hat{S}_1^+} \frac{B(\mathbf{Y})\mathbf{R}(\mathbf{X}^+, \mathbf{Y}) \cdot J(\mathbf{X}^+)\mathbf{N} \cdot \mathbf{F^{-1}}(\mathbf{X}^+)}{2\pi R^2(\mathbf{X}^+, \mathbf{Y})} dS(\mathbf{Y})$$
$$- \int_{\hat{S}_1^+} \frac{B(\mathbf{X}^+)\mathbf{R}(\mathbf{X}^+, \mathbf{Y}) \cdot J(\mathbf{Y})\mathbf{N} \cdot \mathbf{F^{-1}}(\mathbf{Y})}{2\pi R^2(\mathbf{X}^+, \mathbf{Y})} dS(\mathbf{Y})$$
$$- \frac{B(\mathbf{X}^+)}{2\pi}[\pi - \Psi(\hat{S}_1^+, \mathbf{X}^+)]$$
$$+ \int_{S_2^+} \frac{B(\mathbf{Y})\mathbf{R}(\mathbf{X}^+, \mathbf{Y}) \cdot J(\mathbf{X}^+)\mathbf{N} \cdot \mathbf{F^{-1}}(\mathbf{X}^+)}{2\pi R^2(\mathbf{X}^+, \mathbf{Y})} dS(\mathbf{Y}) \quad (4.22)$$

It must be noted that the second and third terms must be evaluated together for numerical purposes. The angle can be easily computed by taking dot products of the position vectors of the required points on the surface of the body.

4.2 Singular Element Formulation for Regular BIE

The development of a singular element in the current problem is analogous to [21], [22] and [28]. The singularity in the surface charge density entails modification of shape functions for the BEM analysis. The singular element must approximate the singularity closely. The order of singularity must be included in the analysis.

4.2.1 Nature of the Singular Solution

The asymptotic solution of the Laplace equation near a singular point (corner) on the boundary of a body can be expressed in terms of a general (complex)

analytic function $\psi(\mathbf{z})$. Since $Re(\psi(\mathbf{z})) = \phi(x, y)$ is harmonic,

$$\phi = Re(\psi(\mathbf{z})) \quad = \quad \frac{1}{2}(\psi + \overline{\psi}) \tag{4.23}$$

where $\overline{\psi}$ is the complex conjugate of ψ. In polar coordinates, the Cartesian components of the normal to the boundary can be expressed as (See Fig. 4.5),

$$n_x \quad = \quad -\sin\theta \tag{4.24}$$

$$n_y \quad = \quad \cos\theta. \tag{4.25}$$

In polar coordinates one has the relationship:

$$\frac{\partial\phi}{\partial n} = \frac{1}{r}\frac{\partial\phi}{\partial\theta} \tag{4.26}$$

Expressing $\mathbf{z}$ in polar coordinates as $\mathbf{z} = re^{i\theta}$ where $i^2 = -1$, one gets from Eq (4.23):

$$\frac{1}{r}\frac{\partial\phi}{\partial\theta} \quad = \quad \frac{1}{2r}(\psi' ire^{i\theta} - ir\overline{\psi}' e^{-i\theta}) \tag{4.27}$$

Substituting into Eq. (4.26), one gets:

$$\frac{\partial\phi}{\partial n} = \frac{i}{2}(\psi' e^{i\theta} - \overline{\psi}' e^{-i\theta}) \tag{4.28}$$

Assume $\psi(\mathbf{z}) = A\mathbf{z}^\lambda$ where A is complex and λ is real. λ is also called the *order of singularity* determined purely by the geometry of the boundary. Hence:

$$\psi(\mathbf{z}) \quad = \quad Ar^\lambda e^{i\lambda\theta} \tag{4.29}$$

$$\overline{\psi}(\mathbf{z}) \quad = \quad \overline{A} r^\lambda e^{-i\lambda\theta} \tag{4.30}$$

Using Eq. (4.29) and (4.30) in (4.23) one gets:

$$\phi \quad = \quad r^\lambda \left[\begin{array}{c} U \end{array}\right] \left[\begin{array}{c} \Gamma \end{array}\right] \tag{4.31}$$

with,

$$\left[\begin{array}{c} U \end{array}\right] \quad = \quad \frac{1}{2}[e^{i\lambda\theta} \qquad e^{i\lambda\theta}] \tag{4.32}$$

$$\left[\begin{array}{c} \Gamma \end{array}\right] \quad = \quad [A \qquad \overline{A}]^T \tag{4.33}$$

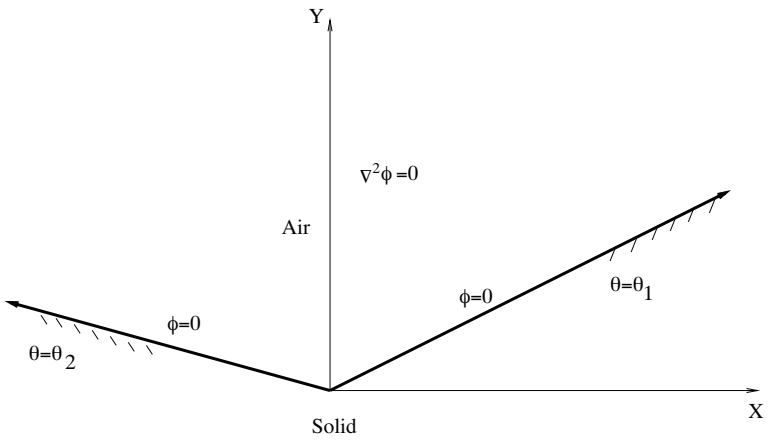

Figure 4.5: Laplace equation solution in polar coordinates

Using the above matrix relationships, one can re-write Eq. 4.28 as:

$$\frac{\partial \phi}{\partial n} = r^{\lambda-1} \left[\; T \; \right] \left[\; \Gamma \; \right] \tag{4.34}$$

where :

$$\left[\; T \; \right] = \frac{d}{d\theta} \left[\; U \; \right] = \frac{i\lambda}{2} [e^{i\lambda\theta} \qquad e^{-i\lambda\theta}] \tag{4.35}$$

4.2.2 Order of Singularity

From Fig. (4.5), one can recast Eq. (4.31) into

$$\phi(\theta_1) = Ar^{\lambda} e^{i\theta_1\lambda} + \overline{A} r^{\lambda} e^{-i\theta_1\lambda} = 0 \tag{4.36}$$

$$\phi(\theta_2) = Ar^{\lambda} e^{i\theta_2\lambda} + \overline{A} r^{\lambda} e^{-i\theta_2\lambda} = 0 \tag{4.37}$$

For Eq. (4.36) and (4.37) in order to have unique solutions, one has the following eigenvalue problem:

$$det \begin{bmatrix} e^{i\theta_1\lambda} & e^{-i\theta_1\lambda} \\ e^{i\theta_2\lambda} & e^{-i\theta_2\lambda} \end{bmatrix} = 0 \tag{4.38}$$

Simplifying Eq. (4.38), one gets

$$\sin[\lambda(\theta_2 - \theta_1)] = 0 \tag{4.39}$$

or

$$\sin[\lambda\Theta] = 0, \qquad \text{where } \Theta = \theta_2 - \theta_1 \tag{4.40}$$

$$\Rightarrow \lambda = \frac{\pi}{\Theta} \tag{4.41}$$

It must be noted that for $\Theta > \pi$, $\frac{\partial\phi}{\partial n}$ is singular (re-entrant corner). For the current problem, $\theta_1 = 0$ and $\theta_2 = 3\pi/2$ implying $\Theta = 3\pi/2$. Hence, from Eq. (4.41), $\lambda = 2/3$.

4.2.3 Construction of a Singular Element for the BIE

A singular element substitutes a normal element at the free end of the cantilever. The shape function for the charge density distribution inside the singular element differs from the remaining elements through the use of asymptotic solutions discussed in the previous section. Eq. (4.33) can be recast as:

$$\left[\ \Gamma\ \right] = C \left[\ \gamma\ \right], \qquad \text{where } \left[\ \gamma\ \right] = \begin{bmatrix} -i \\ \\ i \end{bmatrix} \tag{4.42}$$

Using Eq. (4.42) in Eq. (4.31) and Eq. (4.34) one has:

$$\phi = Cr^{\lambda} \left[\ U\ \right] \left[\ \gamma\ \right] \tag{4.43}$$

$$\frac{\partial\phi}{\partial n} = Cr^{\lambda-1} \left[\ T\ \right] \left[\ \gamma\ \right] \tag{4.44}$$

One needs to compute the following intermediate quantities at the cantilever tip $(\theta = 0)$ in order to obtain the asymptotic expressions for the potential and its

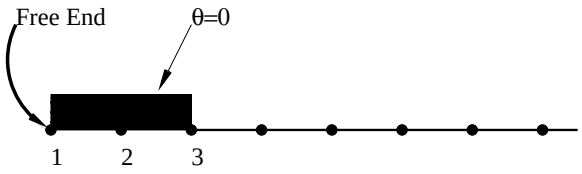

Figure 4.6: Singular element with singularity at the left end

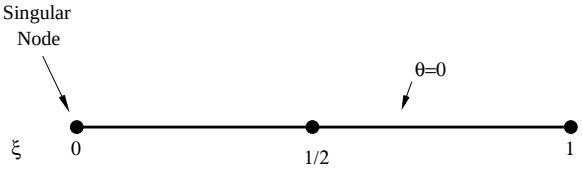

Figure 4.7: Individual singular element

normal derivative (proportional to the charge density) at the singularity,

$$\left[\begin{array}{c} T \end{array}\right]\left[\begin{array}{c} \gamma \end{array}\right] = \frac{i\lambda}{2}\left[\begin{array}{cc} e^{i\lambda\theta} & e^{-i\lambda\theta} \end{array}\right]\left[\begin{array}{c} 1 \\ -1 \end{array}\right](-i)\Big|_{\theta=0} = \lambda \tag{4.45}$$

$$\left[\begin{array}{c} U \end{array}\right]\left[\begin{array}{c} \gamma \end{array}\right] = \frac{1}{2}\left[\begin{array}{cc} e^{i\lambda\theta} & e^{-i\lambda\theta} \end{array}\right]\left[\begin{array}{c} 1 \\ -1 \end{array}\right](-i)\Big|_{\theta=0} = 0 \tag{4.46}$$

Denote the electric potential on the thin conductor as ϕ, and use Gauss's law:

$$\sigma = \epsilon\frac{\partial\phi}{\partial n} \tag{4.47}$$

where ϵ is the permittivity of the medium. Together with Eqs. (4.44) and (4.45) one gets the following asymptotic expression for the singularity dominated zone:

$$\sigma = \epsilon C\lambda r^{\lambda-1} = \overline{C}\lambda r^{\lambda-1} \qquad \text{where } \overline{C} = \epsilon C \tag{4.48}$$

The shape functions in the singular element must contain non-singular components since the element spans space substantially larger than the singularity dominated node [28]. Hence, the normal quadratic shape functions for charge density are modified with singular terms of the same order as in Eq. (4.48).

Assuming the singularity to lie on the left end of a singular element (see Figs. 4.6 and 4.7), one can write the global electric potential and global charge density function inside the singular element in local coordinates as:

$$\sigma = a\xi^{\lambda-1} + b + c\xi \tag{4.49}$$

$$\phi = d\xi^{\lambda} + e + f\xi \tag{4.50}$$

where a, b, c, d, e, and f are constants to be determined. It is clear that at $\xi = 0$, the charge density becomes singular. The asymptotic solution from Eq. (4.48) can be written in local coordinates as

$$\sigma(\xi) = \overline{C}s(\xi), \qquad \text{where } s(\xi) = \lambda\xi^{\lambda-1} \tag{4.51}$$

In the current work, the micro-beam is assumed to be conducting and hence the global potential is constant due the equipotential property of a conductor. From Lim et al.[28], the global charge density function can be expressed in terms of nodal charge density of non-singular nodes $(\sigma^{(2)}, \sigma^{(3)})$ and the constant $\overline{C}$ as:

$$\sigma(\xi) = (2-2\xi)\sigma^{(2)} + (2\xi-1)\sigma^{(3)} + \overline{C}s(\xi) - (2-2\xi)\overline{C}s(1/2) - (2\xi-1)\overline{C}s(1) \tag{4.52}$$

The above expression can be simplified by defining the *charge intensity factor* $M = \lambda\overline{C}$ to:

$$\sigma(\xi) = (2-2\xi)\sigma^{(2)} + (2\xi-1)\sigma^{(3)} + M\xi^{\lambda-1} - (2-2\xi)M\cdot(1/2)^{\lambda-1} - (2\xi-1)M \tag{4.53}$$

The above equation can also be written as,

$$\sigma(\xi) = \begin{bmatrix} L_1 & L_2 & L_3 \end{bmatrix} \begin{bmatrix} \sigma^{(2)} \\ \sigma^{(3)} \\ M \end{bmatrix} \tag{4.54}$$

$$L_1 = 2 - 2\xi \tag{4.55}$$

$$L_2 = 2\xi - 1 \tag{4.56}$$

$$L_3 = \xi^{\lambda-1} - (2-2\xi)\cdot(1/2)^{\lambda-1} - (2\xi-1) \tag{4.57}$$

where $[L_1\ L_2\ L_3]$ denote the shape functions for the singular element. If the singularity lies on the right end of the element, one can replace ξ in the above equation by $1-\xi$ to obtain appropriate global and asymptotic expressions for the charge density.

4.2.4 Work Equivalent Charge Distribution

Solution of the complete electromechanical problem entails computation of traction due to charge density using Eq. (4.18) and use of the hyper-singular auxiliary equation given by Eq. (4.22). Both these equations require one to use the charge density at the singular node. The formulation presented above yields the charge intensity factor at the singularity node and not the actual charge which is infinite. Ong et al. [29] had used this concept to compute equivalent nodal forces analogous to a work equivalent force distribution. In the current chapter, equivalent nodal charges are used which yield both equivalent nodal forces for the traction equation and equivalent charge density for the hyper-singular auxiliary equation. To compute the equivalent nodal charge density, one equates the total charge computed on an element using the asymptotic expression with an assumed quadratic charge density distribution:

$$\sigma^{(i)} = \int_0^1 \sigma_{asym}(\xi) N_i(\xi) J(\xi) d\xi = \int_0^1 M \xi^{\lambda-1} N_i(\xi) J(\xi) d\xi \tag{4.58}$$

where $i = 1, 2, 3$ denotes the nodal points in the singular element, N_i are parabolic shape functions [19] and $J(\xi)$ is the Jacobian at a point in the element. Since the centerline charge density $\beta(\mathbf{x}) = \sigma(\mathbf{x}^+) + \sigma(\mathbf{x}^-)$, it has the same properties as charge density and follows exactly the same treatment.

4.2.5 BIE Regularization at the Singular Element

It must be noted that the BIE appearing in Eq. (4.2) involves logarithmically singular kernels. When the source point lies in the singular element and the field point does not lie in it, the treatment of the integral remains unchanged. However, when the field point lies in the singular element, due to the singular nature of the shape functions, additional singularities must be regularized. To regularize the case when the field point lies in the singular element and source point in a regular element, one can define

$$\mathbf{r}^* = \mathbf{y}^* - \mathbf{x}^+ \qquad \text{where } \mathbf{y}^* \text{ is the position of the singular node} \tag{4.59}$$

Using the above substitution and denoting the singular element as $\hat{s}_1^*$ one can rewrite Eq. (4.2) as:

$$\begin{aligned}\phi(\mathbf{x}^+) = &-\int_{s_1^+ - \hat{s}_1^+ - \hat{s}_1^*} \frac{\ln r(\mathbf{x}^+, \mathbf{y})\beta(\mathbf{y})}{2\pi\epsilon} ds(\mathbf{y}) - \int_{\hat{s}_1^+} \frac{\ln r(\mathbf{x}^+, \mathbf{y})\beta(\mathbf{y})}{2\pi\epsilon} ds(\mathbf{y}) \\ &- \int_{\hat{s}_1^*} \frac{\ln(r(\mathbf{x}^+, \mathbf{y}) - \ln r^*)\beta(\mathbf{y})}{2\pi\epsilon} ds(\mathbf{y}) + \int_{\hat{s}_1^*} \frac{\ln r^*\beta(\mathbf{y})}{2\pi\epsilon} ds(\mathbf{y}) \\ &- \int_{s_2^+} \frac{\ln r(\mathbf{x}^+, \mathbf{y})\beta(\mathbf{y})}{2\pi\epsilon} ds(\mathbf{y})\end{aligned} \tag{4.60}$$

Another kind of singularity may arise when the field point and source point both lie in the singular element. In the current work the geometry of the singular element is assumed to be straight. This assumption is justified since the singular element appears at the end of the beam and for a sufficiently dense mesh, may be assumed to be straight. Assuming a straight geometry, the singular shape function is of the order $\lambda - 1 = -1/3$, the Jacobian is constant and the function $(\ln \xi)/\xi^{1/3}$ is integrable.

4.2.6 HBIE Regularization at the Singular Element

The only source of singularity in the HBIE equation (4.4) is the charge density at the cantilever tip. Hence, if the work equivalent charge density from Eq. (4.58) is used in the Lagrangian version of HBIE equation (4.22), no further regularization of the equation is needed.

4.3 Mechanical Problem for the Elastic Beam

Nonlinear deformation of a beam with no initial axial force is discussed in this section. The beam is linearly elastic, has immovable ends and is of uniform cross section. The cross section is symmetric such that there is no twisting of the beam under applied bending moments. Also, $u(x)$ is the axial deformation and $w(x)$ the transverse displacement of the mid-line of the beam.

4.3.1 The Model

The kinematic equations can be derived starting from the nonlinear strain-displacement equation [30]leading to the following kinematic equations:

$$\epsilon_{xx} = u_{,x} + 1/2 \cdot (w_{,x})^2 \tag{4.61}$$

$$\kappa_x = -w_{,xx}. \tag{4.62}$$

Here, ϵ_{xx} is the midline axial strain and κ_x is the curvature. Also $_{,x}$ denotes the derivative with respect to the axial coordinate x. The strain energy $\mathcal{E}^{(s)}$ and the

kinetic energy $\mathcal{E}^{(k)}$ of an uniform beam of length L are,

$$\mathcal{E}^{(s)} = \frac{EA}{2}\int_0^L [(u_{,x})^2 + u_{,x}(w_{,x})^2 + (1/4)(w_{,x})^4]dx + \frac{EI}{2}\int_0^L (w_{,xx})^2 dx \tag{4.63}$$

$$\mathcal{E}^{(k)} = \frac{\rho A}{2}\int_0^L [(\dot{u})^2 + (\dot{w})^2]dx. \tag{4.64}$$

Here, E, ρ, L, A, I are the Youngs modulus, density (mass per unit volume), length, area of cross section, and area moment of inertia of the cross section of the beam, respectively, and a superposed dot denotes differentiation with respect to time t. Similarly the work expression can be written as,

$$\mathcal{W} = \int_0^L (H_x du + H_y dw + M dw_{,x})dx. \tag{4.65}$$

Here H_x, H_y and M are the axial force, transverse force and bending moment, respectively.

4.3.2 Finite Element Model for Beams with Immovable Ends

The procedure followed here, for FEM discretization of vibrating beams, is similar to standard methods (see, e.g., Zienkiewicz and Taylor [8]). However, in this particular problem the standard beam element needs a slight modification. This modification is necessitated because the usual linear interpolation for the axial deformation results in discontinuities during residual computation in the Newton's scheme. Hence, a quadratic interpolation is taken for the axial deformation. A standard Hermitian interpolation is used for bending. Hence,

the beam element used in this present problem has a total of seven degrees of freedom; three axial at three axial nodes and two transverse and two rotational degrees of freedom at the end nodes. These degrees of freedom can be written as:

$$\begin{aligned} \mathbf{u} &= [u_1\ u_2\ u_3] \\ \mathbf{w} &= [w_1\ w_2] \\ \theta &= [\theta_1\ \theta_2] = [w_{,x1}\ w_{,x2}] \end{aligned} \tag{4.66}$$

Now, the values of the primary deformations $\mathbf{u},\ \mathbf{w}$ inside the elements can be interpolated from the above nodal values using:

$$\begin{bmatrix} u(x,t) \\ w(x,t) \end{bmatrix} = \begin{bmatrix} N^{(I)}(x) & 0 \\ 0 & N^{(0)}(x) \end{bmatrix} \cdot \begin{bmatrix} q^{(I)}(t) \\ q^{(O)}(t) \end{bmatrix} \tag{4.67}$$

wherein

$$[N^{(I)}(x)] = [N_1\ N_2\ N_3], \qquad [N^{(O)}] = [P_1\ P_2\ P_3\ P_4] \tag{4.68}$$

$$[q^{(I)}(t)] = [u_1\ u_2\ u_3]^T, \qquad [q^{(O)}(t)] = [w_1\ \theta_1\ w_2\ \theta_2] \tag{4.69}$$

Here N_k and P_k are third order Lagrange and cubic (Hermite polynomials) interpolation functions, respectively and $q^{(I)}$ and $q^{(O)}$ contain the appropriate nodal degrees-of-freedom. Now, define:

$$D = w_{,x}, \quad [G] = [N^{(O)}_{,x}], \quad [B^{(I)}] = [N^{(I)}_{,x}] \quad [B^{(O)}] = -[N^{(O)}_{,xx}]. \tag{4.70}$$

Substitution of the interpolations from Eq. (4.67) into the work energy expressions from Eq. (4.63), Eq. (4.64) and Eq. (4.65) and use of Hamilton's principle leads to the following element level equations [31]:

$$\begin{bmatrix} M^{(I)} & 0 \\ 0 & M^{(0)} \end{bmatrix} \cdot \begin{bmatrix} \ddot{q}^{(I)}(t) \\ \ddot{q}^{(O)}(t) \end{bmatrix} + \begin{bmatrix} K^{(I)} & 0 \\ 0 & K^{(0)} \end{bmatrix} \cdot \begin{bmatrix} q^{(I)}(t) \\ q^{(O)}(t) \end{bmatrix} + \begin{bmatrix} 0 & K^{IO} \\ 2K^{(IO)T} & K^{(NI)} \end{bmatrix} \cdot \begin{bmatrix} q^{(I)}(t) \\ q^{(O)}(t) \end{bmatrix} = \begin{bmatrix} P^{(I)}(t) \\ P^{(O)}(t) \end{bmatrix}. \tag{4.71}$$

In the above:

$$[M^{(I)}] = \frac{\rho A}{2} \int_0^L [N^{(I)}]^T [N^{(I)}] dx$$
$$[M^{(I)}] = \frac{\rho A}{2} \int_0^L [N^{(O)}]^T [N^{(O)}] dx \tag{4.72}$$
$$[K^{(I)}] = EA \int_0^L [B^{(I)}]^T [B^{(I)}] dx$$
$$[K^{(O)}] = EI \int_0^L [B^{(O)}]^T [B^{(O)}] dx \tag{4.73}$$

$$[K^{(IO)}] = \frac{EA}{2} \int_0^L [B^{(I)}]^T [DG] dx$$
$$[K^{(NI)}] = \frac{EA}{2} \int_0^L [DG]^T [DG] dx \tag{4.74}$$

$$[P] = \int_0^L \begin{pmatrix} N^{(I)} & 0 \\ 0 & N^{(O)} \end{pmatrix}^T \begin{pmatrix} \overline{H}_x \\ \overline{H}_y \\ \overline{M} \end{pmatrix} dx \tag{4.75}$$

where L is the length of the finite element and $[\overline{H}]$ is the resultant traction on the mid-line of the beam. If one denotes $\xi = (I/A)^{1/2}$ as the radius of gyration of the beam cross-section, one can observe a few interesting points about the relations just derived. The in-plane (axial) and out-of-plane (bending) matrices

$[K^{(I)}]$and $[K^{(O)}]$ are $\propto$ to A and $A\xi^2$, respectively, the matrix $[K^{(IO)}] \propto A\delta$ where δ is the beam deflection represents coupling between the axial and bending displacements, and the matrix $[K^{(NI)}] \propto \delta^2 A$ arises purely from the nonlinear axial strains. It is well known that for the linear theory $K^{(O)} \ll K^{(I)}$ as $\xi \to 0$. It is very interesting, however, to note that if δ/ξ remains $\mathcal{O}(1)$ (moderately large deformation), the bending matrix $K^{(O)}$, which arises from the linear theory, and the matrix $K^{(NI)}$ from the nonlinear theory, remain of the same order as $\xi \to 0$ [31].

4.4 Newton's Scheme for Solving the Coupled Problem

Newton's method is an iterative root-finding algorithm that uses the first few terms of the Taylor series of a function $f : \mathtt{R} \to \mathtt{R}$ in the vicinity of a suspected root. The algorithm can be written for a one dimensional case as,

$$x_{n+1} = x_n - \frac{f(x_n)}{f'(x_n)}, \qquad n \geq 0.$$

For the multivariate case, $\boldsymbol{f} : \mathtt{R}^p \to \mathtt{R}^p$,

$$\boldsymbol{x} \in \mathtt{R}^p : \boldsymbol{f}(\boldsymbol{x}) = \boldsymbol{0} \in \mathtt{R}^p$$

$$\boldsymbol{x}_{n+1} = \boldsymbol{x}_n - \boldsymbol{J}\boldsymbol{f}(\boldsymbol{x}_n)^{-1}\boldsymbol{f}(\boldsymbol{x}_n), \qquad n \geq 0 \tag{4.76}$$

where $\boldsymbol{J}\boldsymbol{f}(\boldsymbol{x})$ denotes the Jacobian of the function $\boldsymbol{f}(\boldsymbol{x})$. It is straightforward to re-cast Eq. (4.76) in the context of the current problem by replacing the vector function $\boldsymbol{f}(\boldsymbol{x})$ by the relevant vector function for the present problem.

Newton's scheme is used to solve the entire system of equations of the coupled electro-mechanical problem together. The relevant vector functions used

in the present case are called residuals. Eq. (4.12) gives the electrical residual and Eq. (4.71) gives the mechanical residual. In addition, the auxiliary Eq. (4.22) is used in conjunction with Eq. (4.18) as an inter-domain coupling equation. It must be noted that the primary variables (B and $\mathbf{U} = [\mathbf{u}\ \mathbf{w}\ \theta]$) are, respectively the electrical and mechanical variables. The details of the calculations of the residuals and their gradients are available in [19].

4.5 Dynamic Analysis of MEMS

The computational procedures for dynamic analysis of MEMS are considered next. The governing equation for the dynamic response of MEMS is,

$$\mathbf{M}\ddot{\mathbf{U}}(t) + \mathbf{K}\mathbf{U}(t) = \mathbf{F}(\mathbf{U}(t), \Sigma(t)). \tag{4.77}$$

Here, $\mathbf{U}(t)$ is the displacement vector, $\Sigma(t)$ is the charge density and dots indicate time derivatives. $\mathbf{M}$ and $\mathbf{K}$ are the consistent mass matrix and stiffness matrix, respectively. $\mathbf{F}(\mathbf{U}(t), \Sigma(t))$ represents the electrostatic force which depends on the charge distribution $\Sigma(t)$. Eq. (4.77) can be solved using several direct integration methods when the forces are linear in displacement [7]. However, many of these methods are not directly applicable to MEMS. Two methods applicable to MEMS analysis are the Central Difference Method and the Newmark Method. Eq. (4.77) is solved for $\mathbf{U}(t)$ with the initial conditions,

$$\begin{aligned} \mathbf{U}(0) &= \mathbf{0} \\ \dot{\mathbf{U}}(0) &= \mathbf{0} \end{aligned} \tag{4.78}$$

Now one can define $\dot{\mathbf{U}} = \mathbf{v}$, $\ddot{\mathbf{U}} = \mathbf{a}$ and discretize the time period $[0 \quad T]$ into $[t_1, t_2, \ldots, t_n, t_{n+1}, \ldots, t_N]$ with $t_1 = 0,\ t_N = T$. Consider a typical time interval $[t_n \qquad t_{n+1}]$. Assuming that the solution is known at time t_n, i.e. $[\mathbf{U_n}, \mathbf{v_n}, \mathbf{a_n}]$ are known, the unknown quantities at t_{n+1} are $[\mathbf{U_{n+1}}, \mathbf{v_{n+1}}, \mathbf{a_{n+1}}]$. In the present work, the Newmark method has been employed to update the variables.

4.5.1 The Newmark Method

The Newmark method [32] is a widely used time integration scheme for dynamic analysis in finite element modeling. There are various ways of implementing the Newmark scheme.The version which is used in the present work is called the $a-$form [9]. Define *predictors*,

$$\begin{aligned} \tilde{\mathbf{U}}_{\mathbf{n+1}} &= \mathbf{U_n} + \Delta t \mathbf{v_n} + \frac{\Delta t^2}{2}(1-2\beta)\mathbf{a_n} \\ \tilde{\mathbf{v}}_{\mathbf{n+1}} &= \mathbf{v_n} + (1-\gamma)\Delta t \mathbf{a_n}. \end{aligned} \tag{4.79}$$

The next step is to use the *predictors* to obtain the actual quantities,

$$\begin{aligned} \mathbf{U_{n+1}} &= \tilde{\mathbf{U}}_{\mathbf{n+1}} + \beta \Delta t^2 \mathbf{a_n} \\ \mathbf{v_{n+1}} &= \tilde{\mathbf{v}}_{\mathbf{n+1}} + \gamma \Delta t \mathbf{a_{n+1}}. \end{aligned} \tag{4.80}$$

Here β and γ are algorithmic parameters that are fine tuned for integration accuracy and numerical stability. For a discussion on the effect of these parameters on the performance on the algorithm, see [9].

To start the process, $\mathbf{a_0}$ can be calculated from

$$\mathbf{M a_0} = -\mathbf{K U}(0) + \mathbf{F}(\mathbf{U}(0), \Sigma(0)). \tag{4.81}$$

To march forward in time for acceleration, one needs to solve the time discrete version of the dynamic Eq. (4.77),

$$\mathbf{M}\mathbf{a}_{n+1} + \mathbf{K}\mathbf{U}_{n+1} = \mathbf{F}(\mathbf{U}_{n+1}, \Sigma_{n+1}). \tag{4.82}$$

This equation set is nonlinear and would be solved using the Newton scheme.

4.5.2 Implicit Time Integration

Finally, time integration for the problem is implemented using the Newmark scheme utilizing Newton's scheme. The method follows closely from Belytschko et al. [33]. Using the version of BEM derived in the current work, one can recast Eq. (4.77) as:

$$\mathbf{M}\ddot{\mathbf{U}}(t) + \mathbf{K}\mathbf{U}(t) = \mathbf{f}^{elec}(\mathbf{U}(t), B(t)). \tag{4.83}$$

Here $\mathbf{f}^{elec}(\mathbf{U}(t), B(t))$ denotes the entire force loading term obtained through BEM analysis of the electrostatic problem.

Now define,

$$\mathbf{R}(\mathbf{U}, B) = \begin{pmatrix} R_E \\ \\ R_M \end{pmatrix} \tag{4.84}$$

Here, $\mathbf{R}$ is the grand residual for the problem. The Newton iterative scheme is essentially:

$$\begin{pmatrix} \frac{\partial R_E}{\partial B} & \frac{\partial R_E}{\partial \mathbf{U}} \\ \\ \frac{\partial R_M}{\partial B} & \frac{\partial R_M}{\partial \mathbf{U}} \end{pmatrix}^{(k)} \cdot \begin{pmatrix} \Delta B \\ \\ \Delta \mathbf{U} \end{pmatrix}^{(k)} = - \begin{pmatrix} R_E \\ \\ R_M \end{pmatrix}^{(k)} \tag{4.85}$$

$$\mathbf{U}^{(k+1)} = \mathbf{U}^{(k)} + \Delta\mathbf{U}^{(k)} \quad B^{(k+1)} = B^{(k)} + \Delta B^{(k)}. \tag{4.86}$$

Superscripts are used to denote the iteration step and subscripts for the Newmark integrator. Starting with $k = 0$, Eq. (4.85) is iterated until convergence. At convergence, $\mathbf{R}^{(k)} \equiv R(\mathbf{U^{(k)}}, B^{(k)}) \rightarrow \mathbf{0}$. This iteration helps one find the value of $\mathbf{a_n}$ needed at each step of time integration through an update of $\mathbf{U_n^{(k)}}$. The algorithm for the coupled scheme is available in [19] .

4.6 Numerical Results

The material used for the current analysis is assumed to be Silicon with the following material properties:

$$E = 169GPa, \qquad \nu = 0.22, \qquad \rho = 2231Kg/m^3, \qquad \epsilon = 8.85 \times 10^{-12}F/m. \tag{4.87}$$

Here, E, ν and ρ refer to the Young's modulus, Poisson's ratio and density of Silicon respectively whereas ϵ is the permittivity of free space. It is assumed that the anisotropy is negligible and the beam is made up of poly-silicon for this system. Dynamics of a MEMS beam (the silicon is doped so that it is a conductor), is simulated using the BEM-FEM coupled approach described earlier in the chapter. Each beam is in clamped-free configuration and two beams are used in order to have a zero voltage ground plane (plane of symmetry) midway between them (See Fig. 4.3). The MEMS beam is $1000\mu m$ long, $40\mu m$ wide and $0.5\mu m$ in height. The initial gap (gap_0) is $5\mu m$. The normalized transverse tip deflection is denoted by w_{tip}/gap_0.

Fig. 4.8 shows comparison of normalized tip deflection as a function of voltage

(for a quasi-static version with DC bias) between the singular element formulation and the old nonsingular approach [19]. In both cases, the beam suffers instability when the gap reduces by approximately 57% of the initial value. This result agrees very well with results obtained using reduced order modeling [34]. The difference in pullin voltages between the current singular element approach and [19] is found to be about 5%.

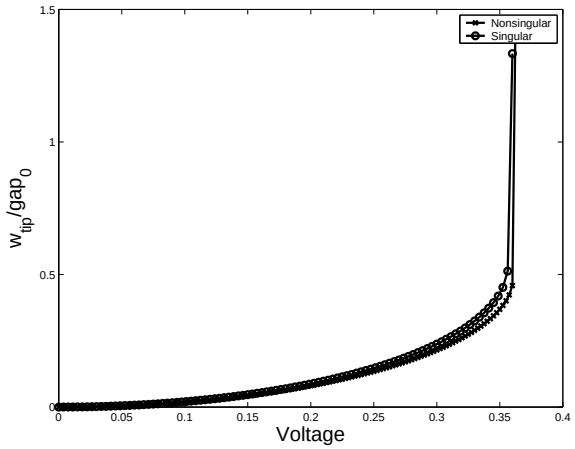

Figure 4.8: Quasi-static pullin comparison

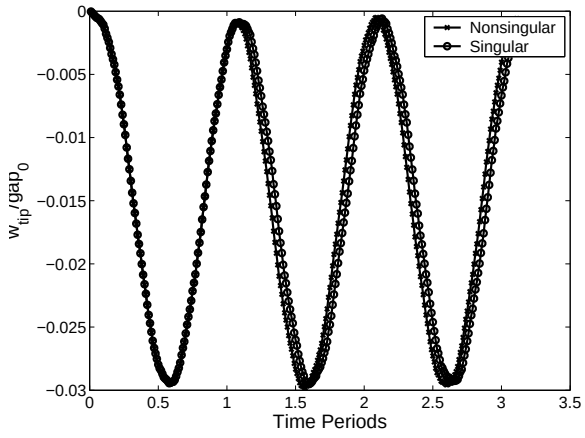

Figure 4.9: DC bias vibration response comparison, V=$0.1V$

A comparison of dynamic behavior of the beam under DC bias at approximately

10% of the pullin voltage can be seen in Fig. 4.9. The time period in the plot refers to $T_p = 2\pi/\Omega_{Nat}$ where $\Omega_{Nat} = (1.875)^2(EI/\rho AL^4)^{1/2}$ from the classical linear beam theory [35]. For the current beam geometry, $T_p \approx 1.443ms$. The frequency of vibration agrees within 1% with this theoretical value for a relatively low excitation voltage which limits the nonlinear effect. The frequency of vibration differs by about 1% between the two methods (current and old [19]).

4.7 Conclusions

The main goal of this work is to understand the effect of the singularity at the corner of the edge of a cantilevered MEMS beam that is subjected to electrical excitations. For this purpose, a singular boundary element is carefully formulated. This formulation for an external Laplace equation is analogous to similar work in [21],[22] and [23]. It should be noted that quasi-static deformation problems are addressed in earlier work while electromechanically coupled as well as dynamic problems are addressed in the present chapter. As can be seen from Figs. 4.8 and 4.9, the new singular element has relatively minimal impact on the numerical results presented here. One should realize however that the singular element presented here is a more faithful mathematical model compared to nonsingular one presented in [19]. It is conceivable that the approximate element presented in [19] is more prone to generating errors for more complicated problems. Also, the element presented here is easy to implement. Therefore, its use is recommended for the future work on this subject.

Acknowledgments

This research has been supported by National Science Foundation Grant $\#CMS - 0508466$ to Cornell University.

BIBLIOGRAPHY

[1] Frangi A. and di Gioa A. Multipole bem for evaluating damping forces on mems. *Comput. Mech.*, 37(1):24–31, December 2005.

[2] Mukherjee S. *Boundary Element Methods in Creep and Fracture*. Applied Science Publishers, London, 1982.

[3] Banerjee P. K. *Boundary Element Methods in Engineering*. McGraw Hill, Europe, 1994.

[4] Chandra A. and Mukherjee S. *Boundary Element Methods in Manufacturing*. Oxford University Press, New York, 1997.

[5] Bonnet A. *Boundary Element Equation Methods for Solids and Fluids*. Wiley, Chichester, UK, 1999.

[6] Mukherjee S. and Mukherjee Y. X. *Boundary Methods: Elements, Contours and Nodes*. Taylor and Francis, CRC Press, Boca Raton, FL, 2005.

[7] Yang T. Y. *Finite Element Structural Analysis*. Prentice-Hall, Englewood Cliffs, New York, 1986.

[8] Zienkiewicz O. C. and Taylor R. L. *The Finite Element Method*, volume 1,2, 4th Ed. McGraw Hill, Berkshire, UK, 2005.

[9] Hughes T. J. R. *The Finite Element Method: Linear Static and Dynamic Finite Element Analysis*. Dover, Mineola, NY., 2000.

[10] Senturia S. D., Harris R. M., Johnson B. P., Kim S., Nabors K., Shulman M. A., and White J. K. A computer aided design system for microelectromechanical systems(memcad). *IEEE J. Microelectromech. Syst.*, 1:3–13, 1992.

[11] Nabors K. and White J. Fastcap: a multi-pole accelarated 3-d capcacitance extraction program. *IEEE Transcations in Computer Aided Design*, 10:1447–1459, 1991.

[12] Gilbert J. R., Legtenberg R., and Senturia S. D. 3d coupled electromechanics for mems: applications of cosolve-em. In *Proceedings, IEEE MEMS*, 1995.

[13] Shi F., Ramesh P., and Mukherjee S. Simulation methods for micro-electro-mechanical structures (mems) with applications to microtweezer. *Comp. Struct.*, 56:769–783, 1995.

[14] Aluru N. R. and White J. An efficient numerical technique for electromechanical simulation of complicated microelectromechancial structures. *Sens. Actuators A*, 58:1–11, 1997.

[15] Shi F., Ramesh P., and Mukherjee S. Dynamic analysis of micro-electro-mechanical systems. *Int. J. Num. Meth. Engng.*, 39:4119–4139, 1996.

[16] Li G. and Aluru N. R. Efficient mixed-domain analysis of electrostatic mems. *IEEE Trans. Comput.-Aided Design*, 22:1228–1242, 2003.

[17] Li G. and Aluru N. R. A lagrangian approach for electrostatic analysis of deformable conductors. *J. Microelectromech. Syst.*, 11:245–254, 2002.

[18] Shrivastava V., Aluru N. R., and Mukherjee S. Numerical analysis of 3d electrostatics of deformable conductors using a lagrangian approach. *Eng. Anal. Bound. Elem.*, 28:583–591, 2004.

[19] Ghosh R. and Mukherjee S. Fully lagrangian modeling of dynamics of mems with thin beams – Part I : Undamped vibrations. *ASME J. Appl. Mech., submitted*, 2008.

[20] Ghosh R. and Mukherjee S. Fully lagrangian modeling of dynamics of mems with thin beams – Part II : Damped vibrations. *ASME J. Appl. Mech., submitted*, 2008.

[21] Ong E.T. and Lim K. M. Three-dimensional singular boundary elements for corner and edge singularities in potential problems. *Eng. Anal. Bound. Elem.*, 29(2):175–189, February 2005.

[22] Ong E.T., Hong L. K., and Lim K. M. An accurate singular boundary element for two-dimensional problems in potential theory with corner singularities. *Int. J. Num. Meth. Engng.*, 6(4):251–260, 2005.

[23] Mukhopadhyay S. and Majumdar N. A study of three-dimensional edge and corner problems using the nebem solver. *Eng. Anal. Bound. Elem.*, 33(2):105–119, February 2009.

[24] Bao Z. and Mukherjee S. Electrostatic bem for mems with thin beams. *Comm. Numer. Meth. Engng.*, 21:297–312, 2005.

[25] Bao Z. and Mukherjee S. Electrostatic bem for mems with thin conducting plates and shells. *Eng. Anal. Bound. Elem.*, 28:1427–1435, 2004.

[26] Mukherjee S. Finite parts of singular and hypersingular integrals with irregular boundary source points. *Eng. Anal. Bound. Elem.*, 24:767–776, 2004.

[27] Nanson E. J. Note on hydrodynamics. *The Messenger of Mathematics*, 7:182–183, 1877-1888.

[28] K. M. Lim, K. H. Lee, A. A. O. Tay, and W. Zhou. A new variable-order singular boundary element for calculating stress intensity factors in three-dimensional elasticity problems. *Int. J. Num. Meth. Engng.*, 55(3):293–316, 2002.

[29] E. T. Ong, K. M. Lim, and H. P. Lee. Techniques in electrostatics analysis of mems and their applications. *MEMS/NEMS Handbook Techniques and Applications*, pages 235–291, 2006.

[30] Reddy J. N. *Introduction to Nonlinear Finite Element Analysis*. Oxford University Press, USA, 2004.

[31] Bao Z., Mukherjee S., Roman M., and Aubry N. Nonlinear vibrations of beams, strings, plates and membranes without initial tension. *ASME J. App. Mech.*, 71(4):551–559, 2003.

[32] Newmark N. M. A method of computation for structural dynamics. *J. Engg. Mech. Div., ASCE*, pages 67–94, 1959.

[33] Belytschko T., Lui W. K., and Moran B. *Nonlinear Finite Element for Continua and Structures*. John Wiley & Sons, Ltd., Chichester, West Sussex, England, 2000.

[34] Younis M. I., Abdel-Rahman E. M., and Nayfeh A. H. A reduced-order model for electrically actuated microbeam-based mems. *IEEE J. Microelectromech. Syst.*, 12(5):672–680, 2003.

[35] Hurty W. C. and Rubinstein M. F. *Dynamics of Structures*. Prentice Hall, Englewood Cliffs, New Jersey, 1964.

CHAPTER 5

CONCLUSIONS AND FUTURE RESEARCH

This dissertation comprises the following. A fully Lagrangian coupled electromechanical dynamics of MEMS with damping effects from a surrounding fluid has been carried out to understand the effects of geometrical parameters like thickness and gap between the ground and the electrostatically actuated conductor, excitation frequency, and damping force from the fluidic property. The dimensional ratio between thickness and length were generally of the order of $1000:1$ with length of the order of a few mm. The electrostatic problem is modeled as an exterior Laplace problem assuming that the doped semiconductor used to manufacture these devices can be assumed conducting. The method of choice for the exterior problem is the boundary element method (BEM) to exploit its well known efficacy for external problems. The structural solid mechanics of the beam is modeled using the finite element method (FEM). The surrounding fluid has been assumed to be Stokes and is also modeled using BEM. The justification for using Stokes has been explained in the work. The full set of governing equations for electric-mechanical and fluidic problem has been solved using a fully Lagrangian framework first proposed by De and Aluru [1] and has been extended to very thin beams with Stokes damping in this work. This approach is equivalent to the usual BEM based on the un-deformed configuration. Through this formulation, re-meshing of deformed structure and recalculation of interpolation functions are unnecessary since the Boundary Integral Equations (BIE) of the system are presented in the referential coordinates. This approach accelerates the speed of convergence due the use of gradient based Newton's method and obviates the need for re-meshing making it more accurate. This approach is extended to the damping problem to compute the effect

of damping force on the structure.

The major analytical challenge in this method remains the extremely careful computation of the residuals needed for the work. It has been observed that the effect of diagonal blocks of the residual gradients (derivatives of domain specific residuals with respect to domain variables themselves, i.e. $\partial R_E/\partial B, \partial R_M/\partial U, \partial R_F/\partial H^f$) have a much greater effect on the convergence properties of the Newton algorithm. Notwithstanding the acceleration wrought by the use of a gradient based Newton algorithm, the numerical efficiency is also affected by the fact that some of the residual gradients themselves have BIE and FEM type constitution requiring more involved computation. In addition, the solution accuracy for the coupled problem is often dependent on many competing accuracies operating within the code. For instance, the tolerance of the Newton loop is not wholly independent from the magnitude of time steps taken. Such competing accuracies can become acute for high frequency excitations for the damped problem. In the absence of well known theoretical limits on these tolerances, some amount of numerical experimentation needs to be done. It is strongly recommended to use advanced data structures and possibly parallel computing for the three dimensional coupled electro-mechanical-fluidic problem. Such faster computing greatly aids the numerical experiments needed to *fine tune* some of the code parameters.

5.1 Extension to Silicon Nano Wires

The analysis presented above can be extended to simulate the coupled electromechanics of Silicon nano wires (SNWs). Typical nanowires exhibit aspect

ratios (length-to-width ratio) of 1000 or more. As such they are often referred to as one-dimensional (1-D) materials. Nanowires have many interesting properties that are not seen in bulk or 3-D materials. This is because electrons in nanowires are quantum confined laterally and thus occupy energy levels that are different from the traditional continuum of energy levels or bands found in bulk materials. Peculiar features of this quantum confinement exhibited by certain nanowires manifest themselves in discrete values of the electrical conductance. Such discrete values arise from a quantum mechanical restraint on the number of electrons that can travel through the wire at the nanometer scale. These discrete values are often referred to as the quantum of conductance. The conductivity of a nanowire is much less than that of the corresponding bulk material due to low mean free path of electrons. Hence, it is often appropriate to treat them as semiconducting in a semi-classical sense [2]. This makes their electrical behavior more complex than the MEMS problem described in the thesis because of distributed charges inside the medium. Hence, in addition to the external Laplace equation, a Poisson equation must also be satisfied in the interior. The semi-classical electrostatic problem of a thin semiconducting nanowire has been solved using a coupled FEM/BEM method by Chen et.al. in [3]. The length scales involved in the silicon nanowires causes the classical assumptions used in this thesis to break down. Significant quantum effects for the electrostatic problem can be seen especially in the case of SNWs with very thin diameter. In addition, SNWs have been reported to behave linear elastically until fracture with a very large fracture strain up to 12% [4]. Hence, once the semi-classical electrostatic model is coupled with the mechanics, the coupled electromechanics of the wire can be simulated as part of an integrated NEMS system employing a computational framework very similar to the one described in the current

thesis.

5.2 Fast Multipole Method

For micro systems involving a huge array of MEMS structure like synthetic microjets, energy harvesters, MEMS based displays and comb drives the analysis presented in the dissertation though analytical correct needs to be modified for computational requirements. Although BEM converts the problem posed in a domain to another defined on the boundary of the domain, thus reducing the dimensionality of the problem by one, its net effect on computational efficiency may not be always positive [5]. Suppose that one introduces N unknowns to discretize a boundary integral equation. The conventional BEM will produce an $N \times N$ full matrix, whose construction will undoubtedly require operations of complexity proportional to N^2. Such an approach, unfortunately, is considered expensive in large problems since other major numerical tools such as finite difference (FDM) or finite element methods (FEM) do the equivalent jobs with $O(N)$ operations thanks to their banded coefficient matrices. One may argue that the Ns for BEM and domain methods are different by an order of magnitude. Even with this difference, one sees that BEM is really inferior to domain methods, at least in 3D problems. Indeed, suppose that one solves a boundary value problem for a cube using $O(n)$ nodes on an edge. In that case the computational complexity of BEM is $O(n^4)$ since $N = O(n^2)$, while those for FDM or FEM is $O(n^3)$ since $N = O(n^3)$. This is the reason why BEM has been considered a loser in large problems. However, recent developments of the fast BEM have revealed that the discretized equation for BIEM may possibly be solved with $O(N) = O(n^2)$ operations, at least in integral equations for Laplaces equation,

with the help of the Fast Multipole Method(FMM) (see [6] and [7]). Although the constant multiplying N in the operation count is quite large, FMM accelerated BEM usually becomes faster than the conventional BEM when N is larger than a few hundreds to thousands. This method thus can be used for solving very large scale practical coupled BEM-FEM problem described before. In BEM, one converts an initial-boundary value problem into an equivalent boundary integral equation, and solves this equation to obtain the solution of the original problem:

$$f(x) = \int_S K(x,y)\phi(y)dy, \qquad x \in S \tag{5.1}$$

where f is a given function defined on a set S, K is a given kernel function defined on $S \times S$, and ϕ is an unknown function on S. This kernel $K(x,y)$ is expanded into the following form:

$$K(x,y) = \sum_n k_n^{(1)}(\mathbf{x}-\mathbf{y}_0)k_n^{(2)}(\mathbf{y}-\mathbf{y}_0) \tag{5.2}$$

where $\mathbf{y}_0$ is a certain point. The functions $k_n^{(1)}$ are usually singular at the origin and $k_n^{(2)}$ are usually entire functions. It can be shown that the functions $k_n^{(2)}$ satisfy:

$$k_n^{(2)}(\mathbf{y}-\mathbf{y}_1) = \sum_m k_m^{(2)}(\mathbf{y}-\mathbf{y}_0)c_{n,m}^R(y_1,y_0) \tag{5.3}$$

where y_1 is a point and $c_{n,m}^R(y_1,y_0)$ are numbers. Now, for a set $S_0 \in S$ and a point $x \notin S_0$, one can use Eq. (5.2) to obtain:

$$\int_{S_0} K(x,y)\phi(y)dy = \sum_n k_n^{(1)}(\mathbf{x}-\mathbf{y}_0)M_n(y_0) \tag{5.4}$$

where $M_n(y_0)$ stands for the multipole moment centered at y_0 defined by:

$$M_n(y_0) = \int_{S_0} k_n^{(2)}(\mathbf{y}-\mathbf{y}_0)\phi(y)dy \tag{5.5}$$

From Eq. (5.3 and Eq. (5.5), one can write the $M2M$ formula:

$$M_n(y_1) = \sum_m M_m(y_0)c_{n,m}^R(y_1,y_0) \tag{5.6}$$

By affecting different kinds of expansion of the Eq. (5.2) one can obtain different kinds of formulae called $L2M$ and $L2L$ (see Nishimura [5] for details). The implementation is carried out by utilizing a tree like hierarchical structure (Fig. 5.1) to reduce computational complexities [7]. It can be shown that the total complexity of the process can be brought down from $O(N^2)$ to about $O(N)$ by the implementation [5]. For applications in the context of the thesis, FMM can be used to accelerate the electrostatic and fluidic problems. FMM has been used to accelerate the Stokes flow and electrostatic Laplace problem in the past (see this book by Liu [8]) and efforts are still on to couple all of them for a dynamic simulation.

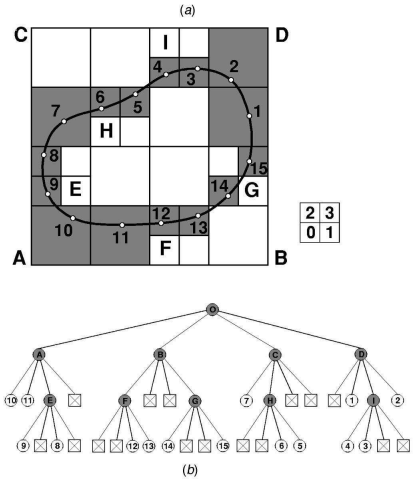

Figure 5.1: A hierarchical structure for utilization in FMM [5]

5.3 Uncertainty Quantification

Low cost and mass manufacturing of MEMS can introduce uncertainties in physical and electrical properties through residual stresses, irregular surface to-

pography and chemical contamination. Such uncertainties can introduce errors in the models developed. Hence, stochastic variation of the relevant parameters are introduced for design simulation. Recently, several approaches have been proposed for reliability-based design optimization of MEMS devices under uncertainties. Allen et al. [9] employed the first-order reliability method for optimizing the tuning accuracy of an electrostatically actuated variable capacitor under reliability constraints. Han and Kwak [10] presented the use of robust optimization during the design of a microgyroscope using MC simulations to compare predicted yields. Liu et al. [11] presented a robust design method to minimize the sensitivity of a laterally vibrating resonator against width variations due to fabrication errors. A genetic algorithm based on MC simulations has been used in [12] for optimizing the filter performance of a MEMS resonator in terms of the shape of the frequency-response curve. Wittwer et al. [13] applied a robust optimization framework based on Taylor series expansion to design a fully compliant bistable micromechanism under various uncertainties. Most of these optimization frameworks are based on MC simulations, which presents a natural but expensive approach for including uncertainties. Specially, when these uncertainties are considered using high-fidelity computational models for the complex multiphysics MEMS problems, it often becomes impractical due to prohibitive computational cost. Agarwal and Aluru in [14]and [15],presented a stochastic Lagrangian framework for MEMS based on a spectral discretization technique - generalized polynomial chaos (GPC) followed by Galerkin projections, which provides high accuracy and fast convergence. uncertainties. Agarwal and Aluru [16] have recently extended their method to using the stochastic collocation approach. The basic formulation of such problem in a strictly formal terms can be explained as follows.

One can write the whole set of electromechanical-fluidic equations described in the dissertation formally as:

$$\mathcal{L}(\mathbf{U}, \beta, H_f; \mathbf{X}, t) = 0 \qquad (\mathbf{X}, t) \in \Omega \times T \tag{5.7}$$

where $\mathbf{U}, \beta, H_f$ are the unknown variables representing displacement, charge density and fluidic traction respectively;Ω represents the physical domain and $t \in [0, T]$ represents the time interval. Eq. (5.7) is clearly deterministic and one needs to specify the input uncertainty. The variation in the input data is assumed to be represented by mutually independent random variables $\xi = \{\xi_i\}_{i=1}^n$ with probability density functions (pdf) $\rho_i : \Gamma_i \longrightarrow \mathbf{R}^+$, for $i = 1, \ldots, n$. The joint pdf is given by:

$$\rho(\xi) = \prod_{i=1}^{n} \rho_i(\xi_i) \qquad \forall \xi \in \Gamma \tag{5.8}$$

where $\Gamma = \prod_{i=1}^{n} \Gamma_i$ represents the support of the set of random variables. Once the formulation of the stochastics have been done, one needs to propagate the uncertainty. Hence one seeks the stochastic displacement $\mathbf{U}(\mathbf{X}, t, \xi)$, surface charge density $\beta(\mathbf{X}, t, \xi)$ and the fluidic pressure $H_f(\mathbf{X}, t, \xi)$ such that:

$$\mathcal{L}(\mathbf{U}, \beta, H_f; \mathbf{X}, t) = 0 \qquad (\mathbf{X}, t, \xi) \in \Omega \times T \times \Gamma \tag{5.9}$$

The computational methods available for uncertainty propagation can be broadly classified into two major categories - methods based on a statistical approach and methods based on a nonstatistical approach. The statistical approach includes methods such as Monte Carlo(MC) simulations and various sampling schemes such as stratified sampling, Latin hypercube sampling (LHS), etc. These statistical methods are straightforward to implement, but can be computationally expensive, as their accuracy depends on the sample size. The most popular of the nonstatistical methods are based on techniques which seek to

directly discretize the unknown stochastic solution like generalized polynomial chaos (GPC) or stochastic collocation (SC) methods.

BIBLIOGRAPHY

[1] De S. K. and Aluru N. R. Full-lagrangian schemes for dynamic analysis of electrostatic mems. *IEEE J. Microelectromech. Syst.*, 13, 2004.

[2] Y. Cui and M. Leiber. Functional nanoscale electronic devices assembled using silicon nanowire building blocks. *Science*, 291(5505):851–853, February 2001.

[3] Chen H., Mukherjee S., and Aluru N. Charge distribution on thin semiconducting silicon nanowire. *Comput. Methods Appl. Mech. Engrg., In Press*, 197:3366–3377, 2008.

[4] Q. Qin W.Y. Fung Y. Zhu, F. Xu and W. Lu. Mechanical properties of vapor-liquid-solid synthesized silicon nanowires. *Nano Lett.*, 9(11):3934–3939, Aug. 2009.

[5] N. Nishimura. Fast multipole accelerated boundary integral equation methods. *Appl. Mech. Rev.*, 55(4):299–325, 2002.

[6] V. Rokhlin. Rapid solution of integral equations of classical potential theory. *J. Comput. Phys.*, 60:187–207, 1985.

[7] L. Greengard. *The Rapid Evaluation of Potential Fields in Particle Systems*. MIT Press, Cambridge, MA., 1988.

[8] Y. Liu. *Fast Multipole Boundary Element Method :Theory and Applications in Engineering*. Cambridge University Press, Cambridge, U.K., illustrated edition, 2009.

[9] K. Maute M. Allen, M. Rauli and D. Frangopol. Reliability-based analysis and design optimization of electrostatically actuated mems. *Comput. Struct.*,, 82(13/14):1007–1020, May 2004.

[10] J. S. Han and B. M. Kwak. Robust optimal design of a vibratory microgyroscope considering fabrication errors. *J. Micromech. Microeng.*,, 11(6):662–671, Oct. 2001.

[11] B. Paden R. Liu and K. Turner. mems resonators that are robust to process-induced feature width variations. *J. Microelectromech. Syst.*, 11(5):505551, Oct. 2002.

[12] K. Maute M. Liu and D. M. Frangopol. Multi-objective design optimization of electrostatically actuated microbeam resonators with and without parameter uncertainty. *Reliab. Eng. Syst. Saf.*, 92(10):1333–1343, Oct. 2007.

[13] Robust design and model validation of nonlinear compliant micromechanisms. *J. Microelectromech. Syst.*, 15(1):3341, Feb. 2006.

[14] N. Agarwal and N. R. Aluru. a stochastic lagrangian approach for geometrical uncertainties in electrostatics. *J. Comput. Phys.*, 226(1):156179, Sep. 2007.

[15] N. Agarwal and N. R. Aluru. Stochastic modeling of coupled electromechanical interaction for uncertainty quantification in electrostatically actuated mems. *Comput. Methods Appl. Mech. Eng.*, 197(43/44):34563471, Aug. 2008.

[16] N. Agarwal and N. R. Aluru. Stochastic analysis of electrostatic mems subjected to parameter variations. *J. Microelectromech. Syst.*, 18(6):1454–1468, Dec. 2009.